SURFACE REACTION MECHANISMS IN PLASMA ETCHING PROCESSES

BY

DA ZHANG

B.S., Zhejiang University, 1993
M.S., Zhejiang University, 1996

THESIS

Submitted in partial fulfillment of the requirements
for the degree of Doctor of Philosophy in Materials Science and Engineering
in the Graduate College of the
University of Illinois at Urbana-Champaign, 2000

Urbana, Illinois

SURFACE REACTION MECHANISMS IN PLASMA ETCHING PROCESSES

Da Zhang, Ph.D.
Department of Materials Science and Engineering
University of Illinois at Urbana-Champaign, 2000
M. J. Kushner, Advisor

Plasma etching is an essential process in the fabrication of submicron features in the semiconductor industry. Plasma-surface interactions in plasma etching processes are capable of influencing bulk plasma properties as well as determining etch rates and feature profiles. To address the coupling of plasma and surface processes, the Surface Kinetics Model (SKM) was developed and was linked to the Hybrid Plasma Equipment Model (HPEM), a two-dimensional, modularized simulation tool addressing low temperature plasma processing. The SKM accepts reactive fluxes to the surface from the HPEM and generates the surface species coverages and returning fluxes to the plasma by implementing a modified site-balance algorithm. The integration of the SKM and the HPEM provides a self-consistent simulation of plasma chemistry and surface chemistry.

The integrated plasma-surface model was used to investigate surface reaction mechanisms in fluorocarbon plasma etching. Fluorocarbon plasmas are widely used for silicon and silicon dioxide etching in microelectronics fabrication due to their high etch rates and good selectivity. One characteristic of fluorocarbon plasma processing is that a polymeric passivation layer is deposited on surfaces during etching. Since the passivation layer limits species diffusion and energy transfer from the plasma to the wafer, the etch rate and selectivity are sensitive to the steady state thickness of the passivation. This polymerization process was investigated. The polymer layer grows by C_xF_y radical deposition and is consumed by ion sputtering and F atom etching. During SiO_2 etching, oxygen atoms in the substrate also etch the polymer. The steady

state thickness of the polymer is achieved as a result of a balance between its growth and consumption. The polymerization kinetics relies on the plasma properties, such as ion bombarding energy and the ion-to-neutral flux ratio, which are determined by process conditions. Relationships between process parameters, plasma properties, polymer thickness, and etching kinetics were investigated in both silicon and silicon dioxide etching. It was demonstrated that processes with thinner passivation provide higher etch rates. The SiO_2 etching process was also investigated with a feature scale model, the Monte Carlo Feature Profile Model (MCFPM). Tapered profiles were obtained with strong sidewall passivation.

Surface reactions occurring in fluorocarbon plasmas also influence plasma properties by consuming or generating plasma fluxes. Of particular interest is the effect that surfaces have on CF_2 densities, as CF_2 is a precursor for polymer formation. These processes were investigated with the integrated plasma-surface model. Simulations demonstrated that CF_2 self-sticking is a loss at the surface, while ion sputtering and large ion dissociation can generate CF_2 at surfaces. The net effect of the surface depends on the relative magnitudes of the loss and generation reactions.

ACKNOWLEDGMENTS

I would like to acknowledge the support of the Semiconductor Research Corporation (SRC), National Science Foundation (NSF), University of Wisconsin Engineering Research Center (ERC) for Plasma Aided Manufacturing, Air Force Office of Scientific Research (AFOSR)/Defense Advanced Research Projects Administration (DARPA) Mutidisciplinary University Research Initiative, Lam Research Corporation, and Applied Materials.

I would like to express my most sincere gratitude to my advisor, Professor Mark J. Kushner, for his guidance. He showed me the direction when I encountered confusion and gave me support when I faced difficulties. His constant help and inspiration made this work possible.

Thanks must also go to my fellow ODP group mates, past and present: Dr. Shahid Rauf, Dr. Eric Keiter, Dr. Fred Huang, Dr. Robert Hoekstra, Dr. Mike Grapperhaus, Dr. Xudong Xu, Kelly Voyles, Ron Kinder, June Lu, Dr. Trudy van der Straaten, Dan Cronin, Rajesh Dorai, Brian Lay, Pramod Subramonium, Arvind Sankaran, Kapil Rajaraman, and Dyutiman Das.

Finally, I would like to thank members of my family for their endless love for me. My beloved wife, Hailan, brings me the most precious things in the world: sincerity, charity, and beauty. My parents, Peifeng and Xiuchun Zhang, always see values in me and give me confidence. My sisters Qing and Yan, and my brother Lan, care about every bit of my happiness and sadness. It would be impossible for me to accomplish anything without their affection and support.

TABLE OF CONTENTS

Page

1. INTRODUCTION 1

1.1. Plasma Etching and Plasma Sources 1
1.2. Plasma Modeling and Simulation 4
1.3. Surface Reactions in Plasma Etching 6
1.4. References 15

2. HYBRID PLASMA EQUIPMENT MODEL 20

2.1. Introduction 20
2.2. Description of the Main Modules of the HPEM 21
2.2.1. The Electromagnetic Module 21
2.2.2. The Electron Energy Transport Module 23
2.2.2.1. The Electron Energy Equation Method 24
2.2.2.2. The Electron Monte Carlo Simulation 25
2.2.3. The Fluid-chemical Kinetics Simulation 26
2.3. Description of the MCFPM and PCMCS Models 29
2.4. Typical Results from the HPEM 30
2.5. References 36

3. SURFACE KINETICS MODEL 37

3.1. Introduction 37
3.2. Description of the Integrated Model 38
3.3. Cl_2/Ar Plasma Etching of Polycrystalline Silicon 46
3.4. References 60

4. MECHANISMS FOR CF_2 RADICAL GENERATION AND LOSS ON SURFACES IN FLUOROCARBON PLASMAS 61

4.1. Introduction 61
4.2. CF_4 Plasma and Surface Reaction Mechanisms for CF_2 Production 62
4.3. CF_2 Production and Loss in an rf CF_4 Discharge 65
4.4. Concluding Remarks 70
4.5. References 81

5. INVESTIGATIONS OF SURFACE REACTIONS IN SILICON ETCHING BY FLUOROCARBON PLASMAS 83

5.1. Introduction 83
5.2. Description of the Reaction Mechanism 84
5.3. C_2F_6 Plasma Etching of Si 87
5.4. Concluding Remarks 95

5.5. References 107

6. INVESTIGATIONS OF THE SURFACE REACTIONS IN C_2F_6 PLASMA ETCHING OF SiO_2 WITH EQUIPMENT AND FEATURE SCALE MODELS 109

6.1. Introduction 109
6.2. Surface Reaction Mechanisms in C_2F_6 Plasma Etching of SiO_2 110
6.3. Etching of SiO_2 in a C_2F_6 Plasma 115
6.4. Profile Simulations of SiO_2 Etching by C_2F_6 Plasma 123
6.5. Concluding Remarks 126
6.6. References 146

7. CONCLUDING REMARKS 148

APPENDIX A. $Ar/CF_4/C_2F_6$ REACTION MECHANISM 151
A.1. References 154

VITA 155

1. INTRODUCTION

1.1. Plasma Etching and Plasma Sources

Plasma etching, an efficient and economical processing technique for obtaining anisotropic micro-sized features in chip manufacturing, has been developing rapidly with the advance of the microelectronic industry [1-7]. Modern microelectronics processes strive to increase the number and density of circuit components on an IC chip by shrinking the minimum feature sizes with each new generation of IC products. Throughout the last four decades this development obeyed Moore's Law described by Intel cofounder Gordon Moore [8], which predicts the yearly doubling of the transistor density, or the annual shrinking of the minimum feature size. The benefits of this trend include the constant improvement in processor speeds to ~700 MHz at 0.18-μm feature size in 2000, and the steady decline in the price for a unit memory cell. The strict design rules necessary in modern processes have led to the replacement of wet chemical etching with dry plasma etching, and to the improvement of the plasma etching.

For wet etching (or chemical etching), a wafer with patterned photoresist (PR) is immersed in a reactive wet solution [9]. The PR, which is etching-resistant, protects the covered area and the exposed wafer area is etched, thereby transferring the pattern from the PR to the wafer. Because wet etchant reacts in all directions of contact, wet processes produce isotropic profiles (undercutting) as shown in Fig. 1.1(b). When overetching happens, the minimum feature obtainable is limited further.

Plasma etching (or dry etching) has the advantage of obtaining anisotropic etching as illustrated in Fig. 1.1(c). As a result, the minimum controllable sizes are much smaller than what wet etching can achieve. Primarily for this reason, plasma etching has dominated the

commercial market and has become an important topic of research. Anisotropic etching by a plasma is attributed to its abundance of energetic etch reactants (radicals and ions) and to the vertically oriented ion bombardment of the wafer surface.

A plasma is a partially ionized gas in an electrically quasi-neutral state. When an electrical field is applied to a gas, free electrons are accelerated by the field. Because the mass of an electron is much smaller than that of a neutral species, electrons lose almost no energy during electron-neutral momentum transfer collisions. As a result the free electrons are accelerated to very high energies, typically several electron volts. When electron energies exceed the threshold energies of inelastic collisions (ionization or excitation), electron impacts of neutral species produce electron-ion pairs and neutral radicals. With proper selection of the source gas, the generated ions and radicals can be utilized as reactants for wafer etching.

In the bulk plasma, charge neutrality is obeyed. Since both electrons and ions are lost to the wall due to diffusion, in a small region near the surface (namely the sheath region), both electron and ion densities are lower than those in the bulk plasma region. Because the electron temperature is much higher than the ion temperature, and because the electron mass is much smaller than ion masses, according to the Einstein's equation for diffusivity, the diffusion coefficient of electrons is much larger than that of ions. The diffusion loss rate for electrons is therefore much larger than that for ions, leading to a net positive charge in the sheath region. According to the Poisson's equation, in order to maintain quasi-neutrality, a sheath potential drop is formed that compensates for the difference in the diffusion loss rates of electrons and ions. The whole process is depicted in Fig. 1.2. In an etching tool, the sheath potential drop above the wafer can be controlled by a bias voltage to be tens or hundreds of volts. The large sheath voltage drop supplies ions with large bombarding energies. And more importantly, once

the sheath electric field is oriented normal to the surface, the motions of ions also become perpendicular to the surface. So the ion bombardment of the surface is anisotropic as well as energetic, and this gives plasma etching the great merit of being an anisotropic process.

Conventional plasma etching tools use parallel plates with capacitive coupling to deposit energy into the plasma [10-11]. Such a system can only generate low-density plasma (10^9 - 10^{10} cm^{-3}). To increase plasma density, the bias voltage needs to be increased. However, because of possible wafer damage from ions with too high an energy, there is an upper limit for the bias voltage. Current high-density plasma reactors decouple the plasma power and ion energy sources. While a substrate bias is commonly used for controlling the ion energies, several methods can be used for generating high-density plasmas (10^{11} - 10^{12} cm^{-3}) for semiconductor processing. The most frequently used methods include electron cyclotron resonance (ECR), helicon waves, and inductively coupling. An ECR reactor uses a microwave source having a frequency equal to the electron cyclotron frequency [12-13]. A resonance effect produces high-energy electrons and a high plasma density at low pressure [14-16]. Helicon plasma sources apply steady-state magnetic fields to induce helicon waves along magnetic field lines for power deposition [17-19]. Inductively coupled plasma (ICP) sources are widely used in the semiconductor industry [20-26]. Power is deposited by inductive coils in an ICP discharge. Fig. 1.3 illustrates a common ICP etching reactor. A spiral coil sits on top of a quartz window, and the rf current passing through the coil produces oscillating magnetic fields that penetrate into the reactor. The magnetic fields then produce oscillating electric fields in the reactor. These fields are the power source for plasma formation. A separate rf bias is connected to the substrate of the wafer. Compared with that from the top coil, the power deposition into electrons from the substrate bias is very low, and it hardly influences the plasma density. The substrate bias,

however, determines the sheath voltage drop at the wafer, allowing the ion energies to be controlled independently.

1.2. Plasma Modeling and Simulation

Due to the high cost of equipment design and experiments for plasma processes in the semiconductor industry, plasma modeling and simulation are desirable to assist in predicting trends. Another benefit of modeling is that by making comparisons between experiments and simulations the understanding of plasma processes can be improved. Throughout the last decade, numerical investigations of plasma systems have developed very quickly due to increasing support from the semiconductor industry and with improvements in computational power.

A plasma can be represented by a continuum model (or fluid model), in which moments of Boltzmann's equation describe charged and neutral species generation and transport. The fields for charged particle acceleration are obtained by solving Poisson's equation and/or Maxwell's equations, depending on the reactor. Tsai and Wu reported the first two-dimensional (2-D) continuum model for rf discharges [27]. Boeuf published a 1-D fluid model for rf capacitively coupled plasmas and then extended it to 2-D [28-29]. The drawback of these early fluid models is that they assumed a fixed electron temperature (T_e) or an electron temperature with a given distribution. To more precisely treat the electron temperature, which strongly influences electron impact properties, electron-energy transport equations (EETE) were included in the plasma model. In 1993 Wu et al. added EETEs to their original fluid model [30-32]. Dalvie et al. published a 2-D model using this methodology in 1993 [33]. To fully capture the plasma kinetics, Boltzman's equation needs to be solved. It is particularly important to use

kinetics models for low-pressure conditions, as the mean free path reaches the dimensional limit of fluid models. A typical method for doing this is the particle-in-cell Monte Carlo collision (PIC-MCC) technique [34-37]. For this method a large number of pseudoparticles are released in the system, with each pseudoparticle representing 10^6 - 10^9 basic particles (electrons or ions). Monte Carlo collisions are then tracked to determine the plasma chemistry and the plasma physics. Vahedi et al. simulated an Ar rf discharge with the PIC-MCC method [38]. They derived bi-Maxewllian electron distribution functions as observed in some experiments [39]. The main drawback of a Monte Carlo kinetics model is its very high computational cost compared with a fluid model. To combine the advantages of fluid models and Monte Carlo kinetics models, some hybrid fluid-kinetics models were developed [40-42], most notably the Hybrid Plasma Equipment Model (HPEM) [40, 42-50].

The first 2-D HPEM model was published by Ventzek et al. in 1993 [42]. In this model electron energy distribution functions (EEDFs) are obtained from a Monte Carlo simulation, and the EEDF results are then used to determine the electron impact reaction rates in the fluid module. Species densities and electric fields are solved from fluid equations. The model was further developed to include an off-line ion and neutral Monte Carlo simulation for heavy particles [43]. The advantage of this hybrid method is that the EEDF is more accurately obtained for the fluid model without adding too much computational cost. Many in-line and off-line modules have been developed for the HPEM after its initial publication. In 1996 ion drag effect was included in the HPEM by Collison and Kushner [44]. Grapperhaus and Kushner developed a sheath module for the HPEM in 1997 [45]. Two off-line models of the HPEM, the Plasma Chemistry Monte Carlo Simulation (PCMCS) and the Monte Carlo Feature Profile Model (MCFPM), were developed by Hoekstra and Kushner for obtaining energy and angular

distributions and feature profile simulation [46-47]. Rauf and Kushner added the noncollisional heating effect of electrons to the HPEM in 1997 [48], and in 1998 they developed an integrated circuit model capable of simulating multifrequency input power [49]. In Chapter 2, a more detailed description of the HPEM will be given.

In plasma process modeling, plasma-surface interactions are important in that, in addition to determining the rate and quality of the process, they can also influence the properties of the bulk plasma by consuming and generating plasma species. To address this coupling of bulk and surface processes, the Surface Kinetics Model (SKM) was developed as a module in the HPEM with the goal of combining plasma chemistry and surface chemistry in a self-consistent fashion [50]. The SKM accepts gaseous reactant fluxes from the HPEM and generates surface species coverages, process rates, and returning fluxes to the plasma by implementing a user-defined reaction mechanism. The integrated HPEM and SKM model is the main simulation platform for this work. The details of the SKM model will be discussed in Chapter 3.

1.3. Surface Reactions in Plasma Etching

A plasma is a combination of neutrals and charged species. Anisotropic ion bombardment is important for wafer etching, but surface interactions for plasma etching are much more complicated than just ion sputtering. The research work by Coburn and Winters marked a milestone for understanding the mechanisms in plasma etching [51]. They found that when using an Ar^+ ion beam only for silicon etching, hardly any etching occured. They also noticed that when using only XeF_2 gas, the etch rate was very slow. When the Ar^+ ion beam and XeF_2 gas were used together, they obtained very high silicon etch rates. Similar work on a Cl_2/Si system also showed that the simultaneous presence of ions and neutrals is essential for efficient

etching. These experiments demonstrated that plasma etching is not simply a physical ion sputtering process, and neither is it a spontaneous neutral etching. It must involve both chemical adsorption of neutrals to the surface and energetic ion bombardment.

Langmuir-type surface reaction models have been successfully used to describe some etching systems. These models consider a surface site as fractional occupations of several surface species. Surface processes involve interactions of incident plasma fluxes with the surface species. Dane and Mentai developed a reaction model for Cl_2 plasma etching of polycrystalline silicon (p-Si), which included Cl atom chemisorption to Si surface sites to form $SiCl_x$ surface species, and ion bombardment of $SiCl_x$ surface sites to form a volatile gas [52]. This model predicted that the Si etch rate was a function of both neutral and ion fluxes, and there were neutral and ion fluxes starved regions for the etch rate. The modeling results for etch rate versus ion power flux agreed very well with their experimental results, as shown in Fig. 1.4. Ono et al. also worked on the Cl_2/p-Si etching system [53-54]. In their model more surface species were included, and redepositions of etch products were taken into consideration. The concept of surface coverage was confirmed by experimental works by Donnelly et al. [55-56]. In their investigations of p-Si etching by a Cl_2/HBr mixture plasma, Donnelly et al. studied the Si surfaces with x-ray photoelectron spectroscopy (XPS) and laser desorption laser-induced fluorescence (LD-LIF). They found that the relative surface coverages of different species are related to the gas ratio of the source and that the etch rate increases with increasing neutral coverages [55].

Fluorocarbon plasmas (C_mF_n) are widely used for silicon and silicon dioxide etching [57-62]. One important feature of C_mF_n plasma etching is the coincidence of polymer deposition on surfaces and wafer etching [63-67]. The polymer layer, which is formed by C_xF_y radical

deposition, regulates wafer etching by preventing direct contact between the plasma and the wafer, and so the thickness of the polymer layer influences both the etch rate and etch selectivity. The polymer thickness can be experimentally determined by *in situ* ellipsometry and XPS measurements [66-67]. In an investigation of Si etching by an inductively coupled C_2F_6 discharge, Oehlein et al. measured the polymer thickness to be on the order of nanometers [66]. They also observed that with decreasing passivation thickness resulting from increasing self-bias voltage on the substrate, the etch rate increases, as shown in Fig. 1.5 [66]. One major effect of the passivation layer is its limit on the radical diffusion fluxes through it. Increasing thickness, in principle, leads to decreasing diffusion fluxes. Oehlein et al. described a qualitative model for fluorocarbon plasma etching of Si [66]. In this model they assumed that a steady state thickness of the polymer layer was reached at the balance of polymer growth (C_xF_y deposition) and polymer consumption (ion sputtering and F atom etching). Si etch precursors (F atoms) need to diffuse through this polymer layer and then reach the Si surface to react. Zhang and Kushner quantitatively developed a model for the fluorocarbon plasma etching of silicon which contains polymer formation, diffusion fluxes through the polymer, and Langmuir-type wafer surface reactions [50]. The work will be discussed in detail in Chapter 5.

The passivation thickness on different materials varies, and this provides etch selectivity. In silicon dioxide etching by fluorocarbon plasmas, due to polymer consumption by the oxygen in the SiO_2, the polymer passivation on the wafer is much thinner than its counterpart in Si etching [68], which leads to faster species diffusion through the polymer. In addition, energetic ions can penetrate through the thin passivation to interact with the SiO_2 wafer surface. Consequently, the SiO_2 etch rate is much higher than the Si etch rate [69-70]. The

polymerization kinetics and the passivation-dependent surface reactions in SiO_2 etching will be addressed in Chapter 6.

Active surface reactions occurring in fluorocarbon plasmas can also influence plasma properties by consuming or generating plasma fluxes. Modern processes require precise control of plasma species densities, and this increases the importance of studying the coupling of surface reactions and plasma properties. For example, in an inductively coupled plasma sustained in a C_2F_6 gas, Oehlein et al. observed the influence of the reactor wall temperature on radical densities (e.g., CF_2, F), because some radical sticking coefficients on the wall change with temperature [70]. As a consequence of the varying radical densities, wafer etch rates changed with wall temperature. Chinzei et al. [71] and Hayashi et al. [72] made similar reports verifying the dependencies between reactor wall temperature, radical densities, and etch kinetics.

The CF_2 radical is one of the major precursors of polymer formation on the surface, so the effect of surfaces on CF_2 density has been investigated by many groups [73-76]. Booth et al. used laser-induced fluorescence (LIF) to measure spatial radical distributions [73-74]. Surface effects on radicals (source or sink) were determined by the spatial gradient or slope of the density to the surface: increasing radical density to the surface implies that the surface acts as a source, and a decreasing slope denotes the surface as a sink [73-74]. They focused on CF and CF_2 radicals in an rf CF_4 discharge and found that the influence of the surface changes with process parameters like power supply and gas pressure [73]. Other groups also observed different surface source or sink effects on CF_2 [75-76]. In a helicon wave reactor with C_4F_8 gas, Suzuki et al. obtained increasing CF_2 density to the surface, or a surface source effect for CF_2 [75]. In a capacitively coupled plasma, Sugai et al. found that the CF_2 density decreased from the bulk plasma to the surface, implying a surface sink effect [76]. These seemingly inconsistent

observations imply that surface effects are determined by many reactions occurring simultaneously on the surface, with some reactions contributing to radical generation and others to radical consumption. The relative rates of radical generation and consumption determine the net effect of a surface. So systematic investigation of these primary plasma-surface interactions is the key for understanding surface effects and optimizing processes. The mechanism of surface reactions for CF_2 production in fluorocarbon plasmas will be discussed in detail in Chapter 4.

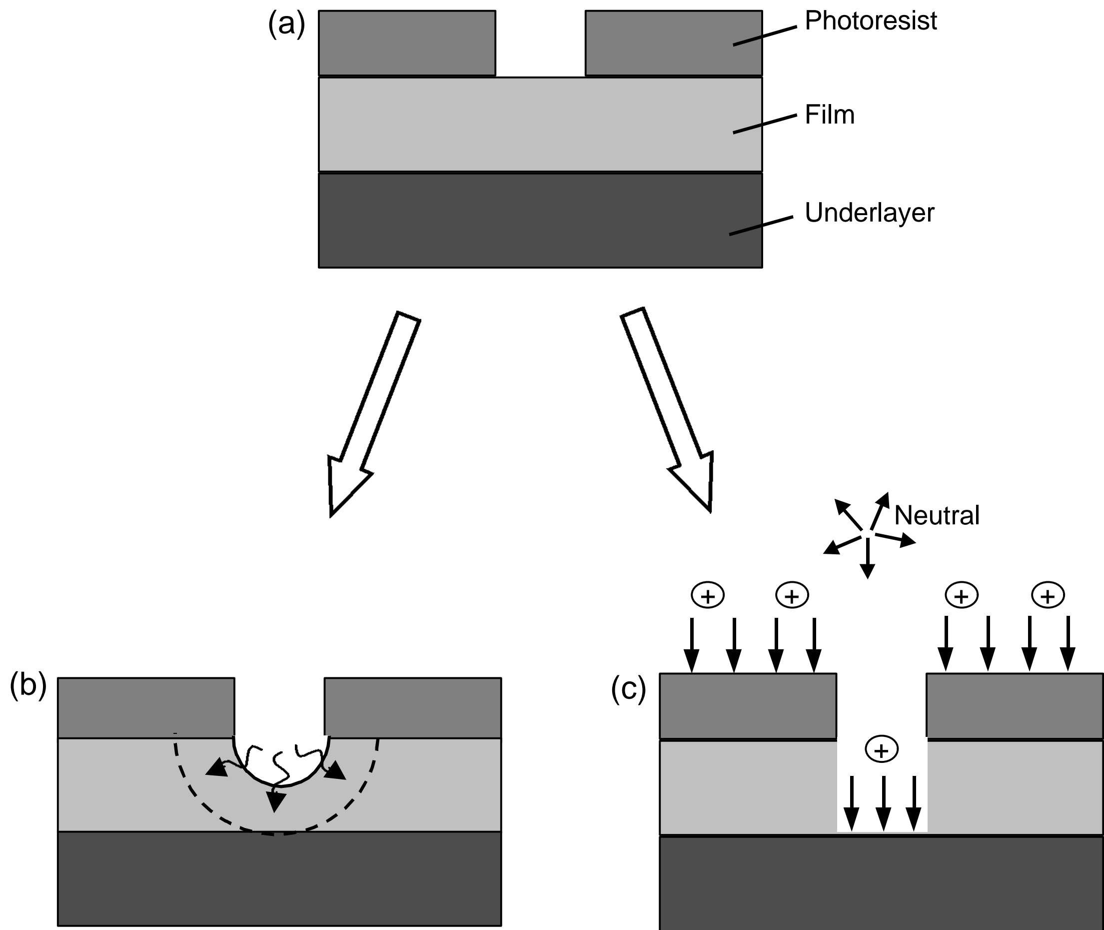

Fig. 1.1. Schematic of etch effects. (a) Before etch. (b) Wet etching. The arrows denote isotropic chemical etching, and the dashed line shows the profile of undercutting. (c) Plasma etching. The divergent arrows represent isotropic motions of neutrals, and the vertical arrows represent anisotropic bombardment of positive ions.

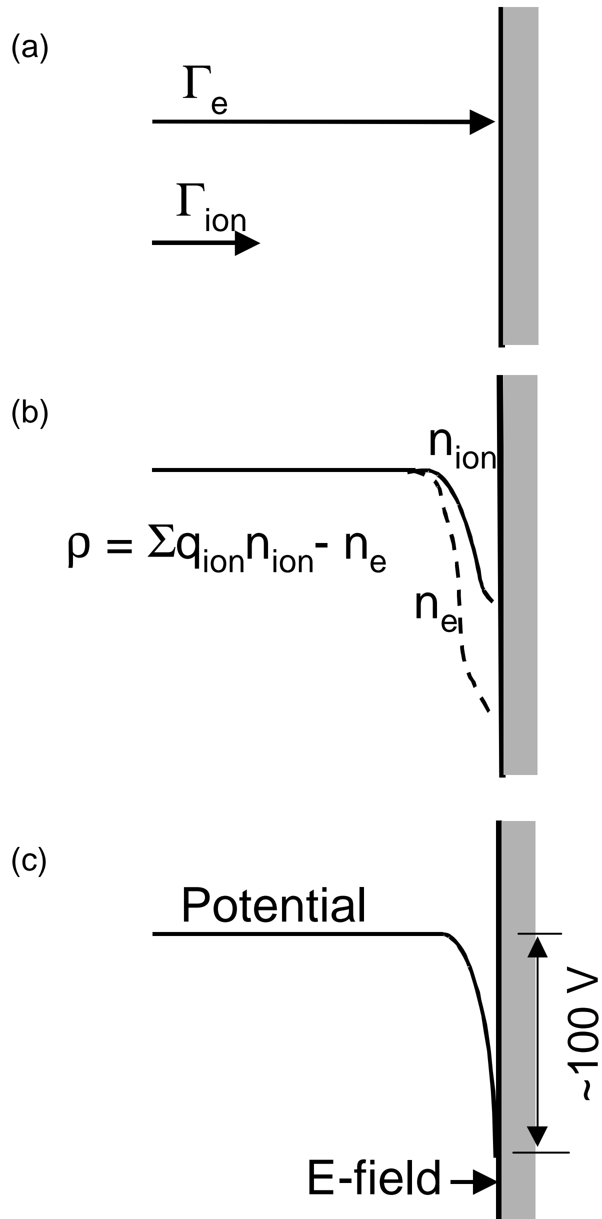

Fig. 1.2. The formation of the sheath potential drop near a surface. (a) The electron diffusion flux is much larger than the ion diffusion flux to the surface due to different diffusivities. (b) A net positively charged region is formed near the surface. (c) The net charge produces a plasma potential drop and a sheath field.

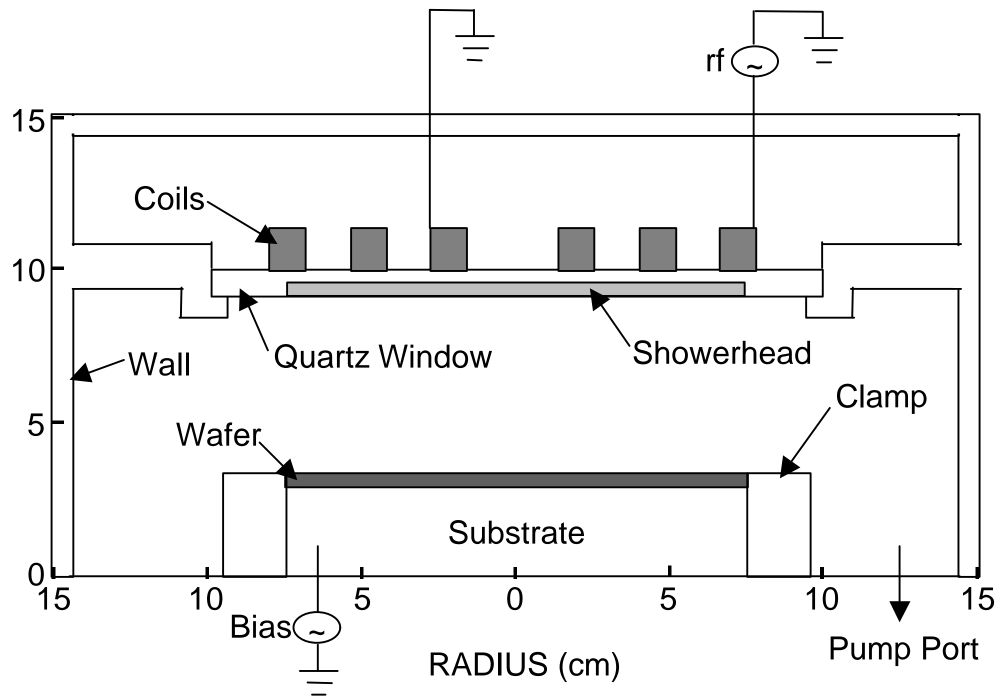

Fig. 1.3. Schematic of an ICP reactor.

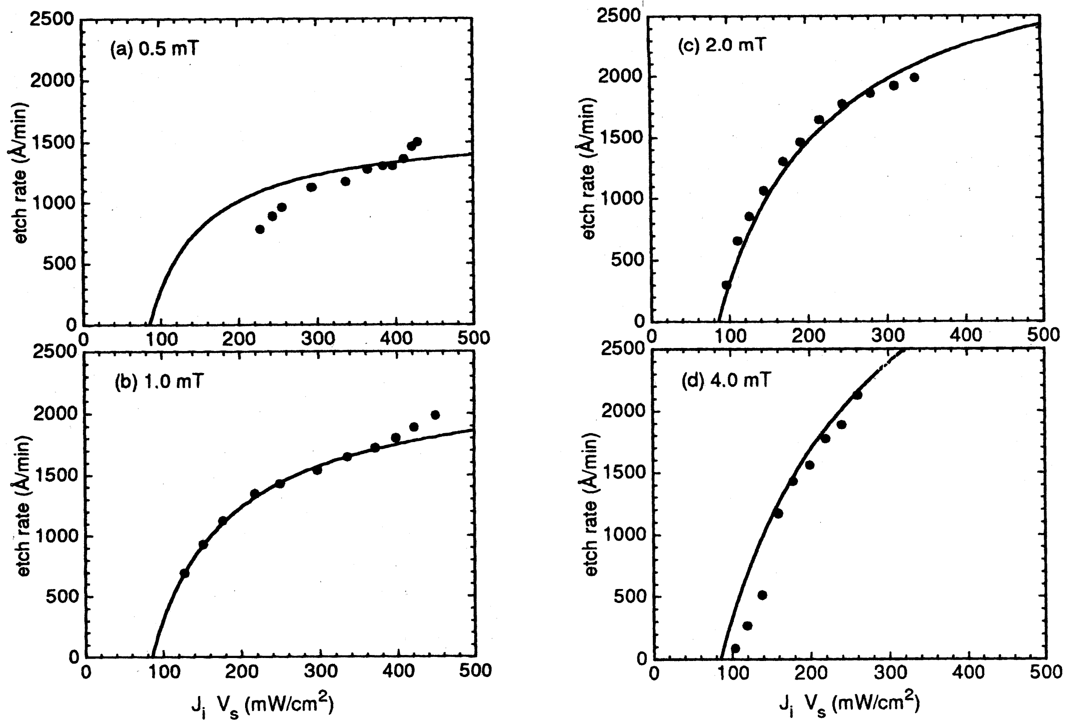

Fig. 1.4. Silicon etch rates (solid points) as functions of ion power fluxes J_iV_s for four Cl_2 pressures (0.5 to 4.0 mtorr), where J_i is the ion current flux and V_s is the sheath voltage drop. The solid lines were derived from a Langmuir-type surface reaction model [52].

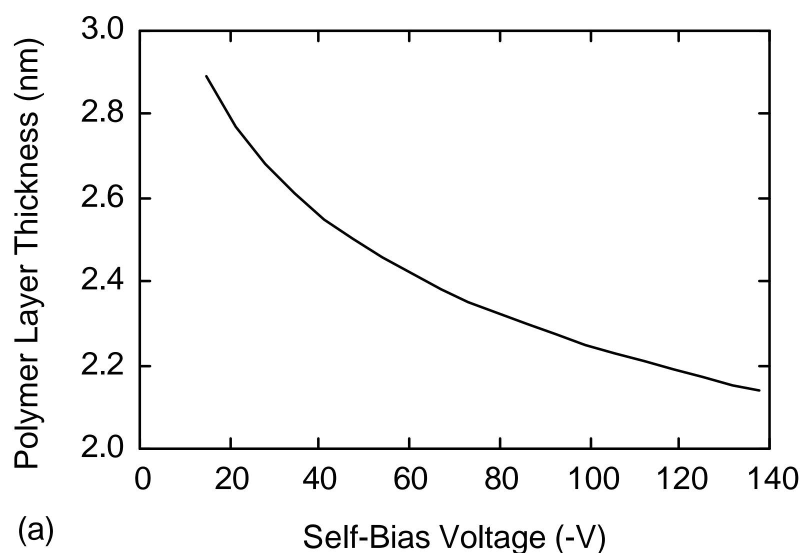

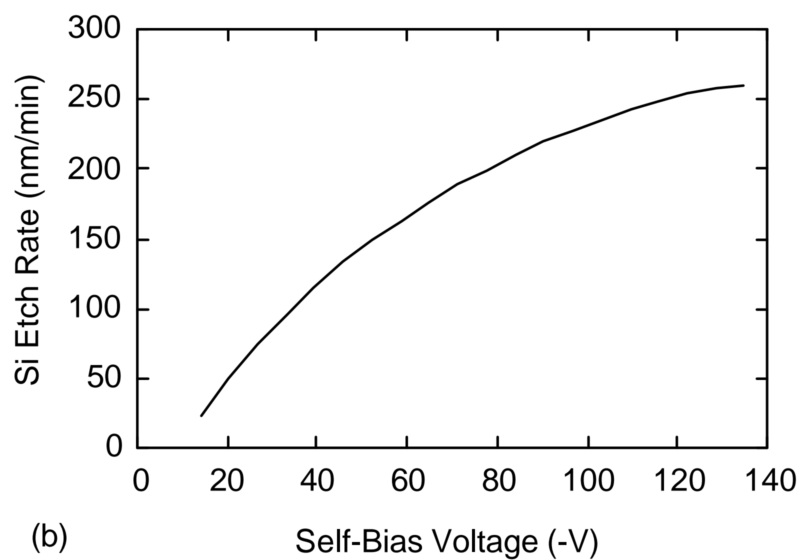

Fig. 1.5. Process properties as a function of the self-bias voltage on the substrate. (a) Polymer layer thickness. (b) Si etch rate. Process conditions: C_2F_6, 100 mTorr, 40 sccm, 1400 W ICP power [66].

1.4. References

[1] G. S. Oehrlein and J. F. Rembetski, IBM J. Res. Develop. **36**, 140 (1992).

[2] Plasma Etching: An Introduciton. Edited by D. M. Manos and D. L. Flamm, Academic Press, 1989.

[3] M. Inayoshi, M. Ito, M. Hori, and T. Goto, J. Vac. Sci. Technol. A **16**, 233 (1998).

[4] M. Armacost, P. D. Hoh, R. Wise, W. Yan, J. J. Brown, J. H. Keller, G. A. Kaplita, S. D. Halle, K. P. Muller, M. D. Naeem, S. Srinivasan, H. Y. Ng, M. Gutsche, A. Gutann, and B. Spuler, IBM J. Res. Develop. **43**, 39 (1999).

[5] J. P. Chang, A. P. Mahorowala, and H. H. Sawin, J. Vac. Sci. Technol. A **16**, 217 (1997).

[6] G. Y. Yeom and M. J. Kushner, Appl. Phys. Lett. **56**, 857 (1990).

[7] C. Lee, M. A. Lieberman, and D. B. Graves, Plasma Chemistry and Plasma Processing **16**, 99 (1996).

[8] G. E. Moore, Proc. Caltech. Conf. on Very Large Scale Integration, California Institute of Technology, Pasadena, California (1979).

[9] J. Hopwood, Plasma Sources Sci. Technol. **1**, 109 (1992).

[10] B. N. Chapman, Glow Discharge Processes, John Wiley & Sons Inc., New York, 1980.

[11] S. J. Choi, P. L. G. Ventzek, R. J. Hoekstra, and M. J. Kushner, Plasma Sources Sci. Technol. **3**, 418 (1994).

[12] J. Asmussen, Jr., T. A. Grotjohn, P. Mak, and M. A.Perrin, IEEE Trans. Plasma Sci. **25**, 1196 (1997).

[13] O. Popov, in Physics of Films, Edited by M. H. Francombe and J. L. Vossen, New York: Academic, 1994.

[14] M. Aoyagi, M. Maezawa, H. Nakagawa, and I. Kurosawa, IEEE Trans. Appl. Superconductivity **7**, 2644 (1997).

[15] N. Fujiwara, S. Ogino, T. Maruyama, and M. Yoneda, Plasma Sources Sci. Technol. **5**, 126 (1996).

[16] H. H. Doh, J. H. Kim, S. H. Lee, and K. W. Whang, J. Vac. Sci. Technol. A **14**, 2827 (1996).

[17] K. P. Shamrai, V. F. Virko, H. O. Blom, V. P. Pavlenko, V. B. Taranov, L. B. Jonsson, C. Hedlund, and S. Berg, J. Vac. Sci. Technol. A **15**, 2864 (1997).

[18] G. D. Conway, A. J. Perry, and R. W. Boswell, Plasma Sources Sci. Technol. **7**, 337 (1998).

[19] T. P. Schneider, W. W. Dostalik, A. D. Springfield, and R. Kraft, Plasma Sources Sci. Technol. **8**, 397 (1999).

[20] J. B. Carter, J. P. Holland, E. Peltzer, B. Richardson, E. Bogle, H. T. Nguyen, Y. Melaku, D. Gates, and M. Ben-Dor, J. Vac. Sci. Technol. B **11**, 1301 (1993).

[21] M. S. Barnes, J. C. Foster and J. H. Keller, Appl. Phys. Lett. **62**, 2622 (1993).

[22] J. R. Woodworth, M. E. Riley, P. A. Riley, and G. A. Hebner, J. Appl. Phys. **81**, 5950 (1997).

[23] M. Puttock, Surface and Coatings Technol. **97**, 10 (1997).

[24] K. B. Jung, E. S. Lambers, J. R. Childress, S. J. Pearton, M. Jenson, and A. T. Hurst Jr., J. Electrochemical Society **145**, 4025 (1998).

[25] P. Colpo, R. Ernst, and F. Rossi, J. Appl. Phys. **85**, 1366 (1999).

[26] M. V. Malyshev, V. M. Donnelly, and S. Samukawa, J. Appl. Phys., **84**, 1222 (1998).

[27] J. H. Tsai and C. Wu, Phys. Rev. A **41**, 5626 (1990).

[28] J. P. Boeuf, Phys. Rev. A **36**, 2782 (1987).

[29] J. P. Boeuf, L. C. Pitchford, A. Fiala, and P. Belenguer, Surf. And Coat. Technol. **59**, 32 (1993).

[30] F. F. Young and C. Wu, Appl. Phys. Lett. **62**, 473 (1993).

[31] F. F. Young and C. Wu, J. Appl. Phys. **74**, 839 (1993).

[32] F. F. Young and C. Wu, IEEE Trans. Plasma Sci. **21**, 312 (1993).

[33] M. Dalvie, M. Surendra, and G. S. Selwyn, Appl. Phys. Lett. **62**, 3027 (1993).

[34] C. K. Birdsall, IEEE Trans. Plasma Sci. **19**, 65 (1990).

[35] M. Surendra and D. B. Graves, IEEE Trans. Plasma Sci. **19**, 144 (1991).

[36] M. V. Alves, M. A. Lieberman, V. Vahedi, and C. K. Birdsall, J. Appl. Phys. 69,3823 (1991).

[37] M. M. Turner and H. B. Hopkins, Phys. Rev. Lett. **69**, 3511 (1992).

[38] V. Vahedi, C. K. Birdsall, M. A. Lieberman, G. DiPeso, and T. D. Rognlien, Plasma Sources Sci. Technol. **2**, 273 (1993).

[39] V. A. Godyak and R. B. Piejak, Phys. Rev. Lett. **65**, 996 (1990).

[40] T. J. Sommerer and M. J. Kushner, J. Appl. Phys. **71**, 1654 (1992).

[41] R. A. Stewart, P. Vitello, and D. B. Graves, J. Vac. Sci. Technol. B **12**, 478 (1994).

[42] P. L. G. Ventzek, T. J. Sommerer, R. J. Hoekstra, and M. J. Kushner, Appl. Phys. Lett. **63**, 605 (1993).

[43] P. L. G. Ventzek, R. J. Hoekstra, and M. J. Kushner, J. Vac. Sci. Technol. B **12**, 461 (1993).

[44] W. Z. Collison and M. J. Kushner, Appl. Phys. Lett. **68**, 903 (1996).

[45] M. J. Grapperhaus and M. J. Kushner, J. Appl. Phys. **81**, 569 (1997).

[46] R. J. Hoekstra, and M. J. Kushner, J. Appl. Phys. **79**, 2275 (1995).

[47] R. J. Hoekstra, and M. J. Kushner, , J. Vac. Sci. Technol. A **15**, 1913 (1997).

[48] S. Rauf and M. J. Kushner, J. Appl. Phys. **81**, 5966 (1997).

[49] S. Rauf and M. J. Kushner, J. Appl. Phys. **83**, 5087 (1998).

[50] D. Zhang and M. J. Kushner, J. Appl. Phys. **87**, 1060 (2000).

[51] J. W. Coburn and H. F. Winters, J. Vac. Sci. Technol. **16**, 391 (1979).

[52] D. Dane and T. D. Mantei, Appl. Phys. Lett. **65**, 478 (1994).

[53] M. Tuda, K. Ono, and K. Nishikawa, J. Vac. Sci. Technol. B **14**, 3291 (1996).

[54] K. Nishikawa, T. Oomori, and K. Ono, J. Vac. Sci. Technol. B **17**, 127 (1999).

[55] C. C. Cheng, K. V. Guinn, I. P. Herman, and V. M. Donnelly, J. Vac. Sci. Technol. A **13**, 1970 (1995).

[56] K. V. Guinn, C. C. Cheng, and V. M. Donnelly, J. Vac. Sci. Technol. B **13**, 214 (1995).

[57] J. W. Butterbaugh, D. C. Gray, and H. H. Sawin, J. Vac. Sci. Technol. B **9**, 1461 (1991).

[58] T. L. Cheeks and A. L. Ruoff, J. Vac. Sci. Technol. A **5**, 1917 (1987).

[59] Y. Chinzei, Y. Feurprier, M. Ozawa, T. Kikuchi, K. Horioka, T. Ichiki, and Y. Horiike, J. Vac. Sci. Technol. A **18**, 158 (2000).

[60] J. P. Booth, Plasma Sources Sci. Technol. **8**, 249 (1999).

[61] G. S. Oehrlein, Y. Zhang, D. Vender, and O. Joubert, J. Vac. Sci. Technol. A **12**, 333 (1994).

[62] N. E. Capps, N. M. Mackie, and E. R. Fisher, J. Appl. Phys. **84**, 4736 (1998).

[63] A. J. Bariya, C. W. Frank, and J. P. McVittie, J. Electrochem. Soc. **137**, 2575 (1990).

[64] B. E. E. Kastenmeiter, P. J. Matsuo, G. S. Oehrlein, and J. G. Langan, J. Vac. Sci. Technol. A **16**, 2047 (1998).

[65] S. Samukawa and S. Furuoya, Jpn. J. Appl. Phys., Part 2 **32**, L1289 (1993).

[66] T. E. F. M. Standaert, M. Schaepkens, N. R. Rueger, P. G. M. Sebel, G. S. Oehrlein, and J. M. Cook, J. Vac. Sci. Technol. A **16**, 239 (1998).

[67] M. Schaepkens, G.S. Oehrlein, C. Hedlund, L.B. Jonsson, H.-O. Blom, J. Vac. Sci. Technol. A **16**, 3281 (1998).

[68] N. R. Rueger, J. J. Beulens, M. Schaepkens, M. F. Doemling, J. M. Mirza, T. E. F. M. Standaert, and G. S. Oehrlein, J. Vac. Sci. Technol. A **15**, 1881 (1997).

[69] F. H. Bell, O. Joubert, G. S. Oehrlein, Y. Zhang, and D. Vender, J. Vac. Sci. Technol. A **12**, 3095 (1994).

[70] M. Schaepkens, R. C. M. Bosch, T. E. F. M. Standaert, and G. S. Oehrlein, J. Vac. Sci. Technol. A **16**, 2099 (1998).

[71] Y. Chinzei, T. Ichiki, R. Kurosaki, J. Kikuchi, N. Iegami, T. Fukazawa, H. Shindo, and Y. Horiike, Jpn. J. Appl. Phys., Part 1 **35**, 2472 (1996).

[72] S. Hayashi, M. Yamanaka, H. Nakagawa, M. Kubota, and M. Ogura, Electronics and Communications in Japan, Part II **81**, 21 (1998).

[73] J. P. Booth, G. Cunge, P. Chabert, and N. Sadeghi, J. Appl. Phys. **85**, 3097 (1999).

[74] G. Cunge and J. P. Booth, J. Appl. Phys. **85**, 3952 (1999).

[75] C. Suzuki, K. Sasaki, and K. Kadota, J. Vac. Sci. Technol. A **16**, 2222 (1998).

[76] Y. Hikosaka, H. Toyota, and H. Sugai, Jpn. J. Appl. Phys. **32**, L353 (1993).

2. HYBRID PLASMA EQUIPMENT MODEL

2.1. Introduction

The Hybrid Plasma Equipment Model (HPEM) has been developed at the University of Illinois for simulating low-temperature, low-pressure plasma processes such as plasma etching and plasma-assisted deposition [1-18]. Two important parameters for plasma processes include the power source and the gas source. The power source, typically capacitively or inductively coupled, generates within the process tool electromagnetic fields that accelerate electrons and drive electron impact processes to produce a plasma. The partially ionized plasma, as a conduction body, is capable of affecting the electric fields inside the process chamber once it is generated. The HPEM handles plasma physics and plasma chemistry in a modular fashion. There is a series of modules that are related to three main blocks: The Electromagnetic Module (EMM), the Electron Energy Transport Module (EETM), and the Fluid-chemical Kinetic Simulation (FKS). Starting with an initial guess of plasma properties, the EMM computes the inductively coupled electric fields determined by the inductive coils, and the magnetostatic fields induced by permanent magnets or dc current loops. These fields are passed to the EETM. Together with a database describing electron collision cross sections, the EETM calculates electron kinetics properties like the electron energy distribution function, electron temperature, and electron impact rate coefficients. Results of the EETM are transferred to the FKS module to determine plasma source and sink terms. The FKS solves the fluid continuity equations for species densities and plasma conductivity. Electrostatic fields are also derived in the FKS by either solving Poisson's equation or assuming quasi-neutrality. The outputs of the FKS are then fed back to the EMM and EETM modules for updated computations. The whole process iterates

until results reach a preset convergence criterion, or until a preset number of total iterations are finished. For simulating an ICP system, all three modules should be used. For an rf capacitively coupled plasma (CCP), only the EETM and FKS modules are used since there is no inductively coupled power source.

Several off-line modules of the HPEM have been developed for other specific purposes. The Plasma Chemistry Monte Carlo Simulation (PCMCS) computes energy and angular dependencies of fluxes at specified surface locations by using outputs from the HPEM [6]. The Monte Carlo Feature Profile Model (MCFPM) uses the results of the PCMCS to simulate micro-scale feature profile evolution [15]. The physics of the three main modules contained in the HPEM will be described in Section 2.2, followed by an introduction to the PCMCS and the MCFPM models in Section 2.3. In Section 2.4, typical results from the HPEM will be presented.

2.2. Description of the Main Modules of the HPEM

2.2.1. The Electromagnetic Module

The electromagnetic module (EMM) computes time varying electric and magnetic fields for the HPEM. For an inductively coupled plasma, rf currents passing through the inductive coils generate azimuthal electric fields that are governed by Maxwell's equations. A reactor may also contain permanent magnets, or dc current loops, to produce magnetic fields that trap electrons and increase power deposition. These electric and magnetic fields determine the motions and collisions of charged particles involved in the production of a high-density plasma.

The EMM module calculates the spatially dependent azimuthal electric fields by solving Maxwell's equation under time harmonic conditions. Assuming azimuthal symmetry, Maxwell's equation for electric fields is reduced to

$$-\nabla \cdot \frac{1}{\boldsymbol{m}} \nabla E_{f} = \boldsymbol{w}^{2} \boldsymbol{e} E_{f} - i \boldsymbol{w} J_{f}\,, \tag{2.1}$$

where $\boldsymbol{m}$ is the permeability, E_{f} is the azimuthal electric field, $\boldsymbol{w}$ is the frequency of the source current, $\boldsymbol{e}$ is the permittivity, and J_{f} is the total current consisting of driving and conduction currents. The conduction current J_c is calculated from $J_c = \boldsymbol{s}E_{f}$, where $\boldsymbol{s}$ is the conductivity. For collisional plasmas, the plasma conductivity is approximated as

$$\boldsymbol{s} = \frac{q_e^2 n_e}{m_e} \frac{1}{\boldsymbol{n}_{me} + i\boldsymbol{w}}\,, \tag{2.2}$$

where q_e is the unit electron charge, n_e represents electron density, m_e denotes electron mass, $\boldsymbol{n}_{me}$ is the momentum transfer collision frequency of electrons, and $\boldsymbol{w}$ is the driving frequency. The first iteration of HPEM takes an initial guess of $\boldsymbol{s}$, and all the subsequent values are obtained from the FKS module. Only electron conduction current is considered here, because ion currents are much smaller due to the low ion mobilities. Maxwell's equations are solved using the successive overrelaxation (SOR) technique. The weighting coefficient and the convergence criterion for the SOR are adjustable simulation parameters.

For an azimuthally symmetric reactor with magnets present, the EMM also solves for the magnetostatic fields in the radial and axial direction. Only dc current loops are used for this calculation. For example, for a mesh that contains a permanent magnet, the code replaces the corresponding grid points with small current loops. Due to the azimuthal symmetry, the magnetic field can be computed through a vector **A,** which satisfies

$$\nabla \times \mathbf{A} = \mathbf{B}; \qquad \nabla \times \frac{1}{\boldsymbol{m}} \nabla \times \mathbf{A} = \mathbf{j}, \tag{2.3}$$

where $\boldsymbol{m}$ is the permeability, and $\mathbf{j}$ is the current density of the source current loops.

2.2.2. The Electron Energy Transport Module

Once electric fields are formed in the reactor chamber, free electrons are accelerated to high energies, on the order of several electron volts. These electrons then inelastically collide with neutrals, leading to neutral dissociation, excitation, and ionization. The electron impact reaction rates strongly depend on the electron temperature T_e, which is related to the electron energy distribution function (EEDF) as

$$T_e = \frac{3}{2} \int f(\boldsymbol{e}) \cdot \boldsymbol{e} \cdot d\boldsymbol{e} \,, \tag{2.4}$$

where $\boldsymbol{e}$ represents electron energy and $f(\boldsymbol{e})$ is the electron energy distribution function. Inelastic collions influence the EEDF by extracting energy from electrons, resulting in a reduction of the high-energy tail of the EEDF. So for a collisional plasma, the EEDF does not behave as a Maxwellian distribution. The Electron Energy Transport Module (EETM) was designed to simulate this effect, more realistically capturing the plasma kinetics and chemistry. There are two ways for the EETM to calculate the electron energy distribution function. The first option, namely the Electron Energy Equation Method (EEEM), solves the zero-dimensional Boltzmann equation to obtain electron transport properties as a function of average electron energy based on

realistic EEDFs. These values are then coupled with the electron energy equation to derive spatial distributions of the electron energy. The second approach of the EETM is to use an electron Monte Carlo simulation (EMCS). The EEDF is then obtained from the collected statistics.

2.2.2.1. The Electron Energy Equation Method

For a plasma with weak interparticle collisions, the Boltzmann equation describes its kinetics. The Boltzmann equation is expressed as

$$\frac{\partial f_e}{\partial t} + \mathbf{v} \cdot \nabla_{\mathbf{r}} f_e - \frac{e(\mathbf{E} + \mathbf{v} \times \mathbf{B})}{m_e} \cdot \nabla_{\mathbf{v}} f_e = \left(\frac{\boldsymbol{d}f_e}{\boldsymbol{d}t} \right)_{collision} , \tag{2.5}$$

where $f_e = f_e(t, \boldsymbol{r}, \boldsymbol{v})$ is the electron distribution function, $\nabla_{\mathbf{r}}$ is the spatial gradient, $\nabla_{\mathbf{v}}$ is the velocity gradient, m_e is the electron mass, and $\left(\frac{\boldsymbol{d}f_e}{\boldsymbol{d}t} \right)_{collision}$ represents the effect of collisions. The Electron Energy Equation Method (EEEM) solves the zero-dimensional Boltzmann equation for a range of E/N (electric field divided by total gas density). The electron temperature and all of its dependent quantities, like electron mobility and electron impact rate coefficients, are derived from the EEDF.

Results of the zero-dimensional Boltzmann equation are then used to provide transport coefficients as a function of average electron energy to solve the electron energy equation:

$$\nabla \boldsymbol{k} \nabla T_e + \nabla \cdot (\Gamma_e T_e) = P_{heating} - P_{loss} , \tag{2.6}$$

where $\boldsymbol{k}$ is the thermal conductivity, T_e is the electron temperature, Γ_e is the electron flux, $P_{heating}$ is the electron heating due to deposition, and P_{loss} is the power loss due to inelastic collisions. $P_{heating}$ is computed from the time averaged value of $\mathbf{j} \cdot \mathbf{E}$, where $\mathbf{j}$ is the electron current obtained from the FKS module, and E is the electric field due to both inductively and capacitively coupled effects.

2.2.2.2. The Electron Monte Carlo Simulation

The electron Monte Carlo simulation (EMCS) tracks the trajectories of electron pseudoparticles in the electromagnetic fields obtained from the EMM module and the electrostatic fields obtained from the FKS. Statistics on electron energy distributions are gathered by tracking the particle motions and collisions. The electrons are initially given a Maxwellian distribution and are spatially distributed according to the electron density distribution calculated by the FKS module. Electrons are accelerated by the electromagnetic and electrostatic fields in a manner governed by the Lorentz equation:

$$\frac{d\mathbf{v}}{dt} = \frac{q_e}{m_e}(\mathbf{E} + \mathbf{v} \times \mathbf{B}) , \tag{2.7}$$

where $\mathbf{v}$ is the velocity ($d\mathbf{r}/dt = \mathbf{v}$ where $\mathbf{r}$ is the location). Collisions can also alter electron energy and location. Energy-dependent collision cross sections and energy losses due to collisions are supplied to the EMCS. Similar to the EEEM method, the EMCS generates spatially dependent electron temperature, collision frequencies, and electron impact rate coefficients.

2.2.3. The Fluid-chemical Kinetics Simulation

In the fluid-chemical kinetics simulation (FKS), fluid equations, together with chemical reactions, are solved to obtain plasma species densities and fluxes. The FKS also computes electrostatic fields by either solving Poisson's equation or using an ambipolar field approximation.

The continuity equation that describes the density evolution rate for any species is

$$\frac{\partial N_i}{\partial t} = -\nabla \cdot \Gamma_i + S_i , \tag{2.8}$$

where N_i is the density, Γ_i denotes the flux, and S_i represents the source term determined by plasma chemical reactions. Rate coefficients for electron impact reactions are obtained from the EETM, and heavy particle reaction coefficients are supplied to the code. These values are used to calculate the source terms. For both electrons and heavy particles, the fluxes can be calculated from the drift-diffusion equation:

$$\Gamma_{\mathrm{k}} = \boldsymbol{m}_{\mathrm{k}} q_k N_k \mathbf{E} - \mathrm{D}_{\mathrm{k}} \nabla N_k , \tag{2.9}$$

where $\boldsymbol{m}$ is the mobility, q is the charge, N is the density, and D is the diffusion coefficient. The transport properties of electrons are obtained from the EETM results. For ions and neutrals, the transport properties are either taken from a database or calculated from Lenard-Jones parameters.

Ion and neutral fluxes can also be solved from the momentum equation:

$$\frac{\partial \Gamma_i}{\partial t} = -\frac{1}{m_i}\nabla(N_i kT_i) - \nabla\cdot(N_i \mathbf{v}_i \mathbf{v}_i) + \frac{q_i}{m_i}N_i(\mathbf{E} + \mathbf{v_i}\times\mathbf{B}) - \nabla\cdot\bar{\boldsymbol{t}} - \sum_j \frac{m_j}{m_i + m_j}N_i N_j(\mathbf{v}_i - \mathbf{v}_j)\nu_{ij} \ , \tag{2.10}$$

where Γ_i, m_i, k, N_i, T_i, and $\mathbf{v}_i$ denotes the flux, mass, Boltzmann constant, density, temperature, and velocity, respectively, of the species i; m_j and N_j are the mass and density, respectively, of the species j; ν_{ij} is the collision frequency between species i and j. Here $\boldsymbol{t}$ is the viscosity tensor for neutral species, and it is only used in the neutral momentum equation.

There are two kinds of flux boundary conditions used in the FKS. The first is the gas inlet and outlet. The FKS uses fixed feedstock gas flux at the inlet, and fixed total gas flux at the outlet. The second kind of boundary condition is the plasma-reactor interface. For an incident flux Φ_{im} of speies i on surface material m, three classes of parameters are used to specify the surface boundary effect: (1) sticking coefficient of the incident species S_{im}, (2) generated returning species j, and (3) fractional generation coefficient of the returning new species j (f_{ij}). The returning flux of the original species is $(1 - S_{im})\Phi_{im}$, and the returning flux of the generated species j is $f_{ij}\Phi_{im}$. In past works the FKS uses fixed boundary conditions at surfaces. The development of the Surface Kinetics Model (SKM) enables the code to calculate sticking and fractional generation coefficients based on plasma-surface chemistry and physics. The boundary conditions rely on the plasma condition and are updated during the HPEM iteration. Details of the SKM model will be discussed in Chapter 3.

In the FKS, the process of solving the continuity equation is coupled with the derivation of electrostatic fields. These fields determine the drift flux terms used in the continuity equation. There are two alternative ways for the FKS to calculate the electrostatic fields. The first option

is to directly solve Poisson's equation. In this method the time-evolving electrostatic potential ϕ is related to the net charge density as

$$\nabla \cdot \varepsilon \nabla \phi = -\rho \,, \tag{2.11}$$

where ε is the permittivity, ϕ is the electrostatic potential, and ρ is the net charge density. To provide implicities, the charge density at the time when ϕ is required is numerically estimated using a first-order Taylor series expansion:

$$\rho^{t+\Delta t} = \rho^{t} + \Delta t \cdot \left.\frac{\partial \rho}{\partial t}\right|^{t+\Delta t} , \tag{2.12}$$

where $\rho^{t+\Delta t}$ is the charge density at time $t+\Delta t$, and ρ^{t} is the charge density at time t. The evolution rate of the charge density $\partial\rho/\partial t$ is determined by the gradient of the total current density $\mathbf{j}$:

$$\frac{\partial \rho}{\partial t} = -\nabla \cdot \mathbf{j} + S \,, \tag{2.13}$$

where S is the source function of charges. In the plasma region, $\mathbf{j} = \sum_i q_i(-D_i \nabla n_i + q_i \mu_i(-\nabla \phi))$; in materials, $\mathbf{j} = \sigma(-\nabla \phi)$ where σ is the material conductivity.

The second option to compute electrostatic fields in the FKS is to use a quasi-neutrality approximation over the entire plasma region. Under such an assumption, the electron density is equal to the total ion charge density at all locations. At steady state, this requires that

$$-\nabla \cdot \Gamma_e + S_e = \sum_i q_i (-\nabla \cdot \Gamma_i + S_i) \tag{2.14}$$

or

$$\nabla \cdot (\mu_e n_e \nabla \phi + D_e \nabla n_e) + S_e = \sum_i q_i (\nabla \cdot (-\mu_i n_i \nabla \phi + D_i \nabla n_i) + S_i) \tag{2.15}$$

when using drift-diffusion equations for both electrons and ions. In the above equations, S_e and S_i represent electron and ion source functions, respectively, and the right-hand side of the equations sum over all charged species. From Eq. 2.15, the electrostatic potential is determined from species densities and species source functions.

2.3. Description of the MCFPM and PCMCS Models

The MCFPM is an off-line module of the HPEM that resolves time-dependent feature profiles resulting from plasma-surface interactions [15]. Heavy particle transport in the HPEM is derived from a fluid algorithm, and so the angular and energy distributions of heavy particles required by the MCFPM are not directly available from the HPEM. The Plasma Chemistry Monte Carlo Simulation (PCMCS) was developed to make the linkage [6]. By using the plasma source functions and the electrical fields available from the HPEM, the PCMCS calculates the energy distributions (ED) and angular distributions (AD) of heavy particles incident on specified surfaces. The plasma fluxes, EDs, and ADs are then supplied to the MCFPM. The MCFPM uses a rectilinear mesh to represent mask, wafer material, surface layers (such as polymer), and the open area filled with plasma. Each cell in the mesh has a material identity. Pseudoparticles representing incident plasma species are launched into the system, following the EDs and ADs

provided by the PCMCS. The pseudopaticles interact with the surface based on a user-defined reaction mechanism, with the probability of each reaction being realized using Monte Carlo techniques. The consequences of these surface interactions include the change of the identity of the surface species, addition or removal of surface species, and reflection and/or generation of plasma fluxes. The returning plasma species from the surface are tracked as new pseudoparticles. Feature profiles are obtained due to the removal or addition of cells representing solid materials.

2.4. Typical Results from the HPEM

The results of HPEM simulations include 2-D distributions of fields, power deposition, source functions, species densities, species fluxes, etc. HPEM outputs for an example case are discussed in this section for an ICP discharge sustained in Cl_2 gas. The schematic of the cylindrical reactor used in this simulation is shown in Fig. 2.2(a). A spiral coil is placed arround the reactor dome, and a 13.56 MHz rf source current is supplied to generate inductively coupled fields. The wafer, 20 cm in diameter and 14 cm below the top inside wall, sits on an rf-biased substrate. Aluminum focus rings with a dielectric constant of 7.9 are used to confine the wafer. Pure Cl_2 is supplied through the gas nozzle at a flow rate of 80 sccm. The pressure is stabilized at 10 mTorr.

The azimuthal electric field is plotted in Fig. 2.2(a). The field is maximum in the region close to the source ICP coils. In this system the ionization produced by the inductive coils dominates over the ionization induced by the capacitive bias (which is typical for most ICP systems). Consequently, the power deposition and the Cl_2^+ ion source peaks occur in the upper right corner of the reactor, as depicted in Figs. 2.2(b) and 2.3(a). Cl_2^+ ion density distribution strongly depends on the source term for this case, so the density is maximum near the peak

source function region, as shown in Fig. 2.3(b). Then ions diffuse away from the peak region to distribute through the reactor. The fluxes are shown as arrows in Fig 2.3(b).

The electric potential is shown in Fig. 2.4. The plasma possesses a uniform potential in the bulk region due to its high conductivity. The rf bias produces a negative dc component on the substrate because of the large difference in the areas for the biased surface and the grounded surface. This results in the sheath voltage drop peaking above the wafer, contributing to the energetic ion bombardment of the wafer surface.

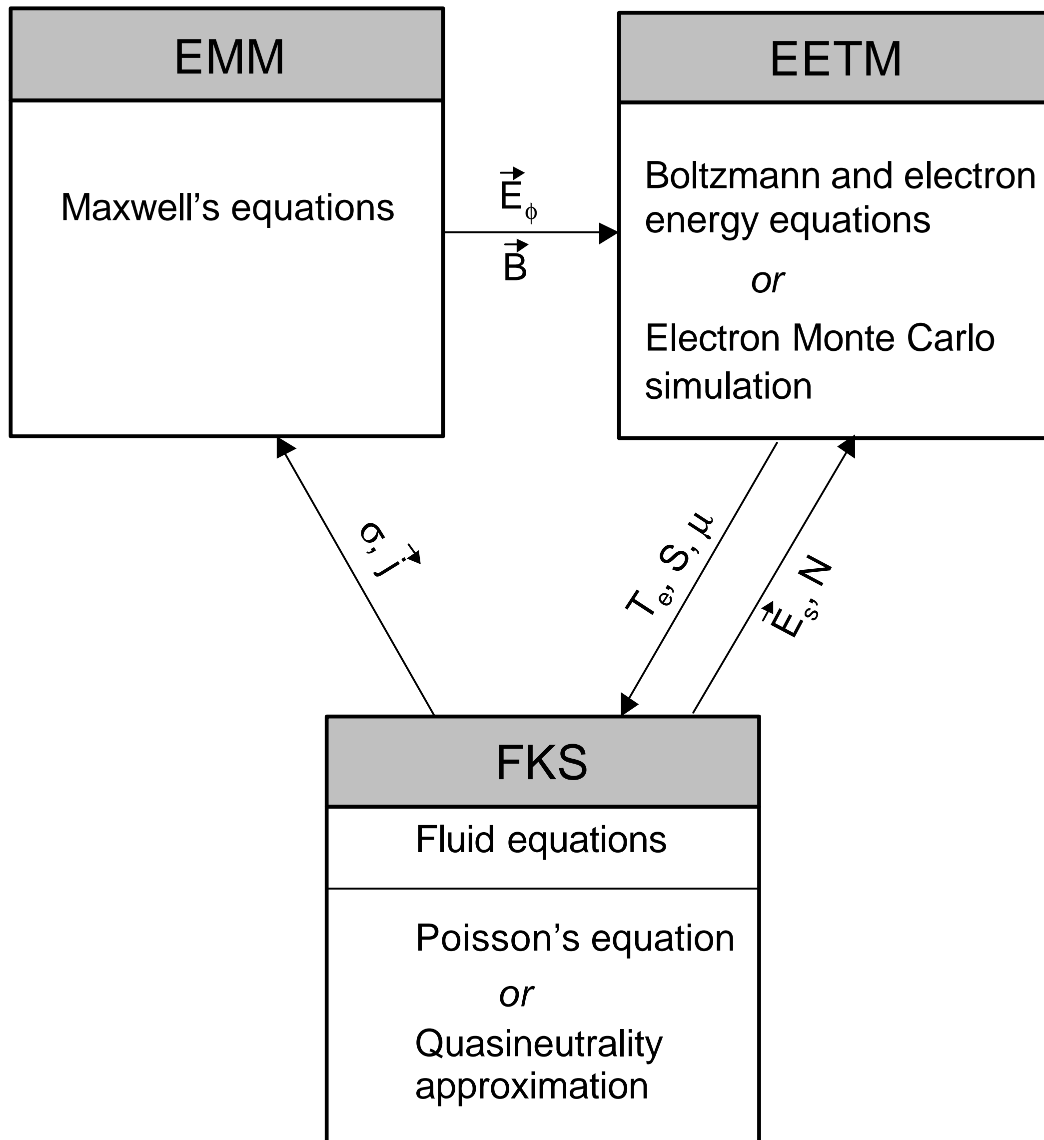

Fig. 2.1. Schematic of the modular HPEM. There are three main modules: the Electromagnetic Module (EMM), the Electron Energy Transport Module (EETM), and the Fluid-chemical Kinetics Simulation (FKS). Data flow among modules and simulations iterate until convergence.

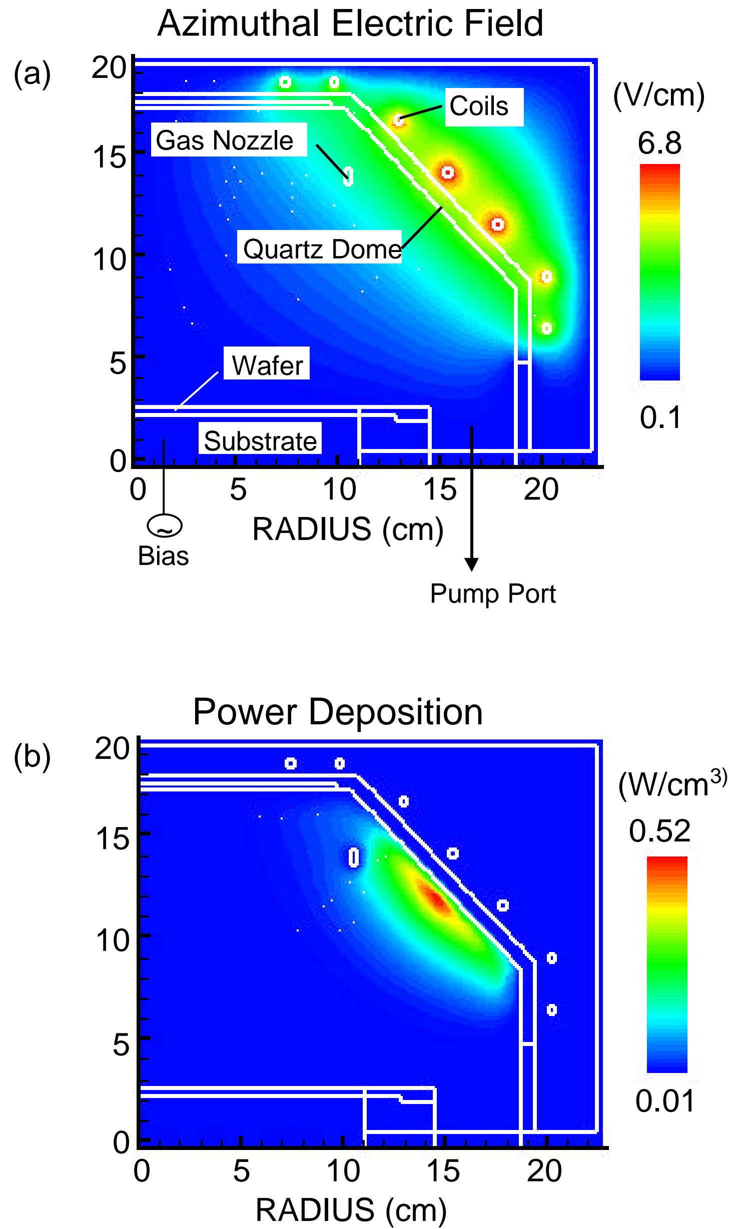

Fig. 2.2. Plasma properties in an ICP reactor. (a) Azimuthal electric field. (b) Total power deposition. Process conditions: Cl_2, 10 mTorr, 80 sccm gas flow rate, 800 W ICP power, 100 V rf substrate bias.

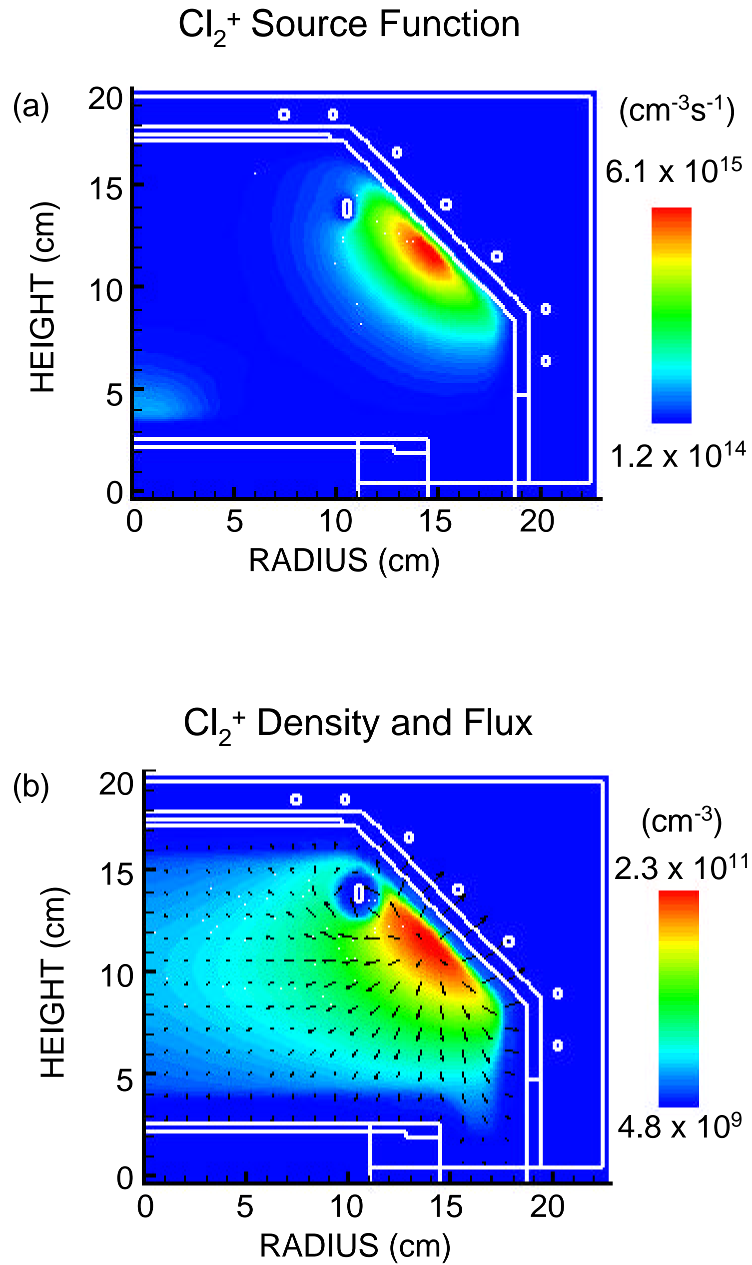

Fig. 2.3. Properties of the ICP plasma described in Fig. 2.2. (a) Cl_2^+ source function. (b) Cl_2^+ density and fluxes. The arrows in (b) denote the relative magnitudes and directions of Cl_2^+ ion fluxes.

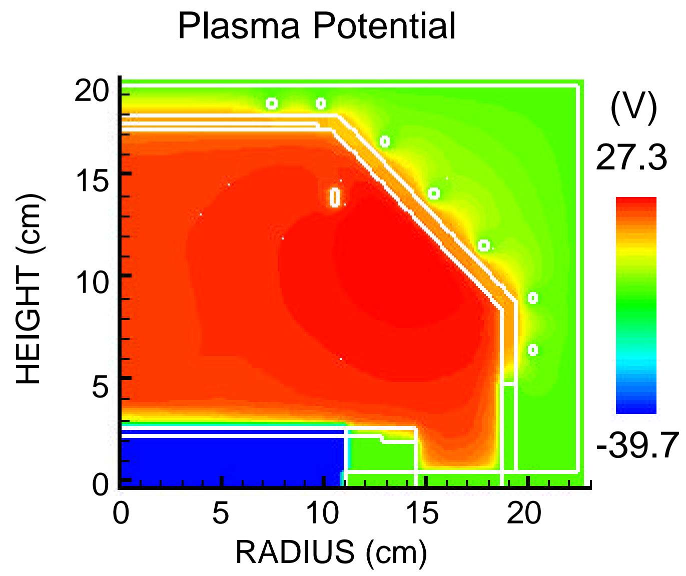

Fig. 2.4. Electric potential of the ICP plasma described in Fig. 2.2.

2.5. References

[1] T. J. Sommerer and M. J. Kushner, J. Appl. Phys. **71**, 1654 (1992).

[2] P. L. G. Ventzek, R. J. Hoekstra, T. J. Sommerer, and M. J. Kushner, Appl. Phys. Lett. **63**, 605 (1993).

[3] P. L. G. Ventzek, R. J. Hoekstra, and M. J. Kushner, J. Vac. Sci. Technol. B **12**, 461 (1994).

[4] P. L. G. Ventzek, M. J. Grapperhaus, and M. J. Kushner, J. Vac. Sci. Technol. B **12**, 3118 (1994).

[5] F. Y. Huang and M. J. Kushner, J. Appl. Phys. **78**, 5909 (1995).

[6] R. J. Hoekstra and M. J. Kushner, J. Appl. Phys. **79**, 2275 (1996).

[7] W. Z. Collison and M. J. Kushner, Appl. Phys. Lett. **68**, 903 (19996).

[8] H. H. Hwang and M. J. Kushner, Appl. Phys. Lett. **68**, 3716 (1996).

[9] M. J. Grapperhaus and M. J. Kushner, J. Appl. Phys. **81**, 5960 (1997).

[10] S. Rauf and M. J. Kushner, J. Appl. Phys. **81**, 5966 (1997).

[11] M. J. Kushner, J. Appl. Phys. **82**, 5312 (1997).

[12] M. J. Grapperhaus, Z. Krivokapic, and M. J. Kushner, J. Appl. Phys. **83**, 35 (1998).

[13] S. Rauf and M. J. Kushner, IEEE Trans. Semiconductor Manufact. **11**, 486 (1998).

[14] S. Rauf and M. J. Kushner, J. Appl. Phys. **83**, 5087 (1998).

[15] R. J. Hoekstra and M. J. Kushner, J. Vac. Sci. Technol. B **16**, 2102 (1998).

[16] S. Rauf and M. J. Kushner, J. Vac. Sci. Technol. A **17**, 704 (1999).

[17] X. Xu, S. Rauf, and M. J. Kushner, J. Vac. Sci. Technol. A **18**, 213 (2000).

[18] D. Zhang and M. J. Kushner, J. Appl. Phys. **87**, 1060 (2000).

3. SURFACE KINETICS MODEL

3.1. Introduction

The trend in plasma processing is towards the use of low-pressure, high-plasma-density etching reactors in which reactive species more frequently interact with the chamber walls and the wafer surface than in their high-pressure counterparts [1]. These trends have renewed concern about the consequences of plasma surface interactions for both the behavior of the bulk plasma and the quality of the etch [2-6]. For example, recent studies were performed by Schaepkens et al. in which the wall temperature of the chamber was varied during Si etching using fluorocarbon gases in an inductively coupled plasma (ICP) reactor [4]. They observed that the density of radicals in the gas phase, the thickness of the polymer layer on the wafer, and the etch rate were all functions of the wall temperature. These effects were attributed to the temperature dependence of the sticking coefficient of fluorocarbon radicals on the walls of the chamber. Plasma equipment, surface chemistry, and molecular dynamics models have been successful in separately addressing bulk plasma and surface processes.[7-11] There have, however, been few efforts to date that have self-consistently combined plasma and surface processes to simulate low-pressure systems where wall processes may dominate.

To investigate surface chemistries and to couple surface reactions with bulk plasma properties, a surface kinetics model (SKM) has been developed for the Hybrid Plasma Equipment Model (HPEM), a bulk plasma simulator previously described in Chapter 2. The linking of the SKM with HPEM has resulted in an integrated plasma and surface simulation. The SKM accepts fluxes of reactants from the HPEM. By implementing a modified surface site balance algorithm at all points along the plasma-surface boundary, the SKM produces surface

coverages, effective reactive sticking coefficients, and the identity of species returning to the plasma. In doing so, different surface reaction mechanisms can be investigated for different types of materials (or locations) in the reactor. Conventional site balance models use gaseous fluxes as available reactants at the surface. However, for fluorocarbon plasma processes, which involve polymeric passivation deposition on surfaces, gaseous fluxes cannot directly reach the wafer to etch. Instead, etch precursors must diffuse through a passivation layer. To address these conditions, the SKM is capable of capturing deposition of passivation layers, passivation thickness dependent etch rates, and transport of reactants through the layer. A comparison of the algorithms of a conventional surface site balance model and the SKM model is shown in Fig. 3.1. The integrated plasma and surface model is described in this chapter.

3.2. Description of the Integrated Model

A detailed discussion of the HPEM has been given in Chapter 2. Before the development of the SKM, the HPEM used a fixed boundary condition at the plasma-solid interface. For each plasma species hitting a surface (e.g., wafer, reactor wall, or quartz window), a reaction probability S_{im} for the ith plasma species and m^{th} surface material was defined. Computationally, all species are "consumed" on all boundaries. Depending on the surface reaction mechanism, species are "reflected" back into the plasma. The reflecting flux of the same species back to the bulk plasma from the mth material is

$$\Phi^{R}{}_{im} = (1 - S_{im}) \cdot \Phi^{I}{}_{im}, \tag{3.1}$$

where $\Phi^{I}{}_{im}$ is the flux of species i to the surface m. We also specified that each incident species

may produce other species on the surface. So for a species i incident onto surface m, the flux of the jth generated species returning to the plasma is

$$\Phi^{R}{}_{ijm} = \Phi^{I}{}_{im} \cdot f_{ijm}, \tag{3.2}$$

where f_{ijm} is the fractional generation rate. For example, consider an argon ion (species 1) striking a wall passivated by a CF_x polymer (material 4), neutralizing to form ground state Ar (species 2) with unity probability and sputtering CF_2 (species 3) with probability of 0.2 $Ar^+ \xrightarrow{\text{wall}} Ar + CF_2$. The coefficients are $S_{14} = 1$, $f_{124} = 1$, $f_{134} = 0.2$. This method is, in principle, exact provided that all of the S_{im} and f_{ijm} coefficients are specified properly. Since the values of S_{im} and f_{ijm} ultimately depend on surface coverages, and on the fluxes and energies of reactants, a surface reaction mechanism is required to specify them, and that is the purpose of the SKM.

The SKM was designed to be a self-consistent module functioning within the HPEM framework. The SKM first identifies specified surface locations on chosen materials, sets the initial surface species coverages, and extracts reactive fluxes to the surface from the HPEM. Based on a specified surface reaction mechanism, differential equations for fractional occupancy of surface sites and thickness of overlaying polymer layers are integrated in time. After reaching the steady state or a specified end time, the resulting coefficients S_{ik} and f_{ijk} are fed back to the HPEM for use as boundary conditions in the manner previously described. These coefficients are held fixed until the next call to the SKM. Etching or deposition rates are obtained based on the surface coverages and reactive fluxes at the end of the call to the SKM. The flow chart of the integrated model is shown in Fig. 3.2.

There are three classes of processes in the surface reaction mechanism used by the SKM. The first class involves reactions of plasma species with surface species or sites. For etch systems without polymer deposition on the wafer, this class of reactions is enough for surface modeling. For etch systems involving polymer formation on surfaces, this class of reactions describes interactions of plasma fluxes and the first exposed layer of the solid boundary. The generic form of these reactions is

$$A_g + B_s \xrightarrow{k_i} C_s + D_g + E_g, \tag{3.3}$$

where the subscript g denotes a gas phase species and the subscript s denotes a surface resident species or a surface site, and k_i is the reaction probability of the ith reaction. The rate of reaction of the ith process of gas species A with surface species B on material m, $R_{im,}$ is

$$R_{im} = k_i \cdot \Phi^I_{Am} \cdot \boldsymbol{\theta}_{Bm}, \tag{3.4}$$

where Φ^I_{Am} is the incident plasma flux of species A on m, $\boldsymbol{\theta}_{Bm}$ is the fractional surface coverage of surface species or site B on m. The evolution rate of the surface coverage of species species B on m contributed by the ith reaction $(\partial \theta_{Bm} / \partial t)_i$ is

$$\left(\frac{\partial \boldsymbol{\theta}_{Bm}}{\partial t} \right)_i = -\frac{1}{T} R_{im}, \tag{3.5}$$

where T is the total surface site density per unit area. In the mechanism some reactions may

generate surface species B, and some other reactions may consume B. So overall, the evolution rate of the surface coverage of species B on surface material m is

$$\frac{\partial \boldsymbol{q}_{Bm}}{\partial t} = \frac{1}{T}\left(\sum_{i=1}^{p} R_{im} - \sum_{j=1}^{q} R_{jm} \right), \tag{3.6}$$

where p is the total number of reactions generating B on m, and q is the total number of reactions consuming B on m. To calculate steady state surface coverages of surface species, the differential equations describing surface coverage evolution rates for all species are integrated over time by using a third order Runge-Kutta technique until they converge or until a specified time has elapsed.

The surface reaction coefficient S_{Am} for incident plasma species A on material m, which is used in the bulk plasma model, is then the sum of the reaction rates of all processes including A as a reactant:

$$S_{Am} = \sum_{j=1}^{s}\sum_{i=1}^{n} \frac{R_{iAjm}}{\Phi_{Am}^{I}} = \sum_{j=1}^{s}\sum_{i=1}^{n} k_i \boldsymbol{q}_{jm} , \tag{3.7}$$

where s is the total number of surface species and n is the number of reactions of A with surface species j. The generation rate for the returning flux of a gaseous reaction product D (Eq. 3.3) from material m is then the sum of the rates of all reactions generating D:

$$\Phi_{Dm}^{R} = \sum_{\ell=1}^{t} \Phi_{\ell Dm}^{R} = \sum_{\ell=1}^{t}\sum_{j=1}^{s}\sum_{i=1}^{n}\sum_{p=1}^{q} k_i \Phi_{\ell m}^{I} \boldsymbol{q}_{mj} \boldsymbol{d}(p-D) , \tag{3.8}$$

where t is the total number of gas phase species and q is the number of products of that reaction. The returning flux coefficient from material m is then

$$f_{ADm} = \sum_{j=1}^{s} \sum_{i=1}^{n} \sum_{p=1}^{q} k_i \theta_{jm} \delta(p - D). \tag{3.9}$$

For an etch system having no simultaneous polymer deposition, the etch rate can be derived from the first class of reactions. Although there is no formation of additional polymer layers, some etch products can still redeposit to the surface, and the effect is the "reverse" of an etch step, or a "negative" rate of etching. For example, in Cl_2 plasma etching of p-Si, etch products ($SiCl_2$, $SiCl_4$) can redeposit onto the wafer surface. After reaching steady state, the SKM sums up the net rates of etching and deposition processes to obtain the total etch rate:

$$ER = M \cdot \left(\sum_{i=1}^{e} R_{im} - \sum_{j=1}^{d} R_{jm} \right), \tag{3.10}$$

where ER denotes etch rate, M is the monolayer thickness of the wafer material, e is the total number of reactions contributing to wafer etching, and d is the total number of reactions for etch product redeposition.

The rate coefficients for surface reactions with ions may be a function of ion energy. The rate of such a reaction is typically characterized by a threshold energy and an exponential [12],

$$p(E) = p_0 \cdot \frac{E^m - E_{th}^m}{E_{ref}^m - E_{th}^m}, \tag{3.11}$$

where *p(E)* is the reaction probability for an ion with energy *E*, E_{th} is the threshold energy of the process, E_{ref} is a reference energy, and p_0 is the reaction probability at the reference energy. Typically, $m = 1/2$ for sputtering or ion activated etching, and that value was used in this work. In this version of the HPEM, we are not explicitly computing the kinetic energy of individual ions. The ion energy used in *p(E)* is an average value obtained in the following manner. The sheath voltage drop V_s at each surface location is estimated by taking the difference between the local plasma and surface potential. The sheath thickness t_s at a given surface location is determined by searching for the nearest location to the surface where quasi-neutrality is achieved. We approximate the quasi-neutral condition as

$$\frac{\left| \sum_i (q_i \cdot n_i) - n_e \right|}{n_e} \le 5\% , \tag{3.12}$$

where n_i is the ion density, q_i is the charge of the ion, and n_e is the electron density. Assuming collisions totally dissipate the initial ion energy, the energy (E_i) of the incident species *i* is estimated by

$$E_i = Min(1, \frac{\lambda_i}{t_s}) \cdot V_s , \tag{3.13}$$

where λ_i is the mean free path of the species.

The second class of reactions in the mechanism is between surface species or surface sites. For example,

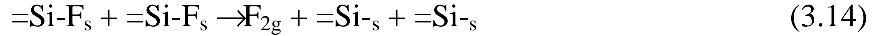

$$=\text{Si-F}_s + =\text{Si-F}_s \rightarrow \text{F}_{2g} + =\text{Si-}_s + =\text{Si-}_s \qquad (3.14)$$

denotes the interconnection of two fluorine passivated silicon surface sites, evolving molecular fluorine and producing two bare Si sites. The rates of reaction for these processes are $k \cdot \theta_F \cdot \theta_F$, where k is the rate coefficient.

The third class of reactions accounts for deposition of multiple layers of passivation and transport of species through those layers. For example, during fluorocarbon etching of Si, CF_x radicals deposit on the wafer surface to form a polymer layer. The thickness of this layer regulates the etch rate [5]. F atoms, the precursor for Si etching, must diffuse through the CF_x passivation layer, and so thicker layers imply lower diffusion rates and lower Si etching rates. Similarly, thicker passivation layers disperse incident ion energy before it can reach to the surface to activate desorption processes.

For processes involving polymer deposition and passivation-dependent etching, the SKM first solves for the steady state thickness of the passivation layer. Generally, neutral sticking and energetic ion sputtering are the main generation and consumption factors for the polymer. Because both are surface processes, under conditions when more than one monolayer of polymer is formed, a regulating force which depends on the polymer thickness is required for the polymer to reach a steady state thickness. For example, in fluorocarbon plasma etching of Si/SiO_2, F atoms can etch the C_xF_y polymer formed on the wafer surface, which is a bulk process.

The time-dependent evolution rate of the passivation is obtained from

$$\frac{dL^t}{dt} = G^t - C^t - R(L^t)\,, \tag{3.15a}$$

where L^t is the passivation thickness at time t, G^t and C^t are thickness-independent passivation generation and consumption rates, respectively, at time t, and $R(L^t)$ is the thickness-dependent passivation regulating force. It is the existence of $R(L^t)$ that allows the polymer to reach a steady state. That is, $dL^{ts}/dt \rightarrow 0$, where t_s is the time for achieving steady state. The steady state thickness of the passivation layer L_s is obtained by integrating the passivation evolution rate until t_s:

$$L_s = L_0 + \int_0^{ts} \frac{dL^t}{dt} dt\,, \tag{3.15b}$$

where L_0 is the initial passivation thickness.

In order for etch precursors to react with the wafer surface covered by the polymer, four steps must take place: (1) Etch precursors adsorb on the top surface of the passivation layer. (2) The absorbed precursors diffuse through the polymer layer to reach the polymer-wafer interface. (3) The etch precursors at the interface react with wafer surface sites to form volatile gases, either spontaneously or by ion bombardment. 4) Volatile products diffuse back through the polymer layer. There are two options for the SKM to account for the influence of the polymer. The first approach is to directly describe these adsorption, diffusion, and reaction steps in the reaction mechanism. Adsorptions of etch precursors are described using the first class of reactions. Assuming Fick's law for diffusion of the etch precursors (EP) through the passivation

layer, the diffusion flux $\boldsymbol{G}_{EP}$ reaching the wafer surface can be approximated as

$$\Gamma_{EP} = D \cdot \frac{EP_t - EP_i}{L}, \qquad (3.16)$$

where D is the diffusion coefficient, EP_t is the density of the etch precursor on the top surface of the passivation layer, EP_i is the density of the etch precursor at the interface between the polymer and wafer, and L is the passivation layer thickness at the surface site. This diffusion flux supplies etch precursors to the polymer-wafer interface. EP_i then reacts with the wafer surface species in the manner described for the second class of reactions. The process of diffusion of volatile etch products back through the polymer is not presently addressed in our model. Once a volatile product is formed, it is directly returned to the plasma region. These algorithms have been used in an investigation of Si etching by a fluorocarbon plasma, which will be discussed in Chapter 5. The second method that the SKM can use for assessing the influence of polymer passivation is to calculate polymer-thickness-dependent reaction rates. This method combines the effects of adsorption, diffusion, and reaction steps into one analytic model describing the influence of the polymer. Details of this approach, and its application to an investigation of C_2F_6 plasma etching of SiO_2, will be given in Chapter 6.

3.3. Cl_2/Ar Plasma Etching of Polycrystalline Silicon

In this section, Cl_2/Ar mixture plasma etching of polycrystalline silicon (p-Si) will be discussed as an example of the operation of and results from the SKM. This etching system does not have polymeric deposition on the wafer, so the surface reactions addressed in this section belong to the first class of reactions described in Section 3.2 (direct contact between plasma

fluxes and surface species). Etching with polymer deposition will be discussed in detail in Chapters 4, 5, and 6.

For the p-Si to be etched away, initial passivation by Cl is required. Cl neutrals can chemisorb onto the wafer to sequentially passivate the Si sites to form $-SiCl_{xs}$ surface species:

$$Cl_g + Si_s \rightarrow SiCl_s, \tag{3.17}$$

$$Cl_g + SiCl_s \rightarrow SiCl_{2s}, \tag{3.18}$$

$$Cl_g + SiCl_{2s} \rightarrow SiCl_{3s}. \tag{3.19}$$

Ion bombardment then serves as an activation energy source to release $-SiCl_{xs}$ species from the surface, exposing new Si_s sites. The incident ions themselves get neutralized. For example,

$$Ar^+_g + SiCl_{2s} \rightarrow SiCl_{2g} + Si_s + Ar_g. \tag{3.20}$$

Some ions also serve as chemical sources for surface etch reactions. For example,

$$Cl^+_g + SiCl_s \rightarrow SiCl_{2s} + Si_s. \tag{3.21}$$

In this reaction, the incident Cl^+ ion becomes a part of the volatile $SiCl_{2g}$ product. Overall, for Cl_2/Ar plasma etching of p-Si, neutral sticking and ion bombarding are two processes required for wafer etching.

For this system, etch products can redeposit to the surface to hinder wafer etching. For example, $SiCl_2$ products can stick back onto the surface:

$$SiCl_{2g} + Si_s \rightarrow Si_2Cl_{2s} . \qquad (3.22)$$

This requires additional ion bombardment to remove a volatile product:

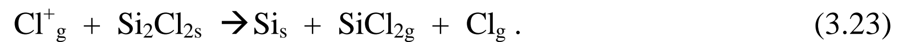

$$Cl^+_g + Si_2Cl_{2s} \rightarrow Si_s + SiCl_{2g} + Cl_g . \qquad (3.23)$$

Wall reactions can influence plasma properties due to the large surface area of the reactor wall. For chlorine plasmas, wall reactions can convert an incident Cl flux into a returning Cl_2 flux:

$$Cl_g + W_s \rightarrow WCl_s , \qquad (3.24)$$

$$Cl_g + WCl_s \rightarrow W_s + Cl_{2g} , \qquad (3.25)$$

where W_s denotes the wall. In addition, ion sputtering of the Cl-passivated wall can release chlorine from the surface.

Based on the above discussion, a reaction mechanism describing plasma-surface interactions has been developed for the SKM and is summarized in Table 3.1. The mechanism

includes reactions for neutral chemisorption, ion sputtering, reactive ion etching, etch product re-deposition, and wall regulation. Plasma reactants and products include Cl_2, Cl, Cl^* ("*" denotes an excited state), Cl^+, Cl_2^+, Ar, Ar^*, Ar^+, $SiCl_2$, and $SiCl_4$. Wafer surface species include Si_s, $SiCl_s$, $SiCl_{2s}$, $SiCl_{3s}$, Si_2Cl_{2s}, Si_2Cl_{3s}, and Si_2Cl_{4s}. Wall surface species include W_s, WCl_s, and $WSiCl_{2s}$.

The reactor geometry for this simulation is shown in Fig. 3.3(a). It is almost the same as that in Fig. 2.2, except that a showhead is used to replace the gas nozzle for gas supply. Process conditions are Ar/Cl_2 = 70/30, 10 mTorr pressure, 80 sccm gas flow rate, and 100 V rf substrate bias. The ICP power applied varies from 300 to 2000 W.

Results at 2000 W ICP power are discussed. The electron temperature and $SiCl_4$ density distributions are shown in Fig 3.3(a) and 3.3(b) respectively. The electron temperature peaks near the source ICP coils because the peak azimuthal field and power deposition occur there. Electron impact source functions and densities of electron-impact-produced species are also maximum near the coils. $SiCl_4$ is maximum near the wafer because it is only produced by surface reactions. The Cl and Cl^+ ion fluxes to the wafer are shown in Fig. 3.4(a). Cl^+ is the dominant ion for this case. The fluxes increase from the wafer center to larger radii as a consequence of the gas phase density distributions. Radial distributions of steady state surface coverages are shown in Fig. 3.4(b). The $SiCl_{xs}$ species show uniform distributions along the wafer because their regulating forces, produced by Cl and Cl^+ fluxes, vary in similar trends. As shown in Fig. 3.5(a), the sheath voltage drop above the wafer is uniform. This implies that the probabilities for reactive ion etching reactions are the same at different wafer locations. Under such conditions (uniform surface coverages and similar reaction probabilities), the distribution of the etch rate follows the pattern of the ion flux, as shown in Fig. 3.5(b).

Simulations were performed at different ICP powers from 300 to 2000 W. The Cl^+ fluxes at the wafer center and edge, as a function of source power, are shown in Fig. 3.6(a). Due to the off-axis peak of the power deposition, fluxes at the wafer edge are larger than those at the wafer

center. For this range of power, the increase in the ion source function with increasing power dominates, so the ion flux increases with power. The relationship between Cl flux and the source power is depicted in Fig. 3.6(b). At first Cl flux increases with increasing power due to increasing source functions. After reaching 800 W, Cl flux saturates. At high powers, Cl_2, the source for Cl generation, is already depleted, and so further increasing the power does not increase the Cl density and flux.

Since neutral chemisorption and ion bombardment are both required for efficient etching, the saturation of the Cl flux at high power limits the etch rate. The etch rate as a function of the ICP power is shown in Fig. 3.7. In the power range where Cl flux only slowly increases (800 - 2000 W), for 800 - 1500 W, the etch rate increases with power due to the contribution of increasing ion fluxes. So here the etch rate is in a "ion-starved" region. After 1500 W, increasing ICP power, although it still increases ion fluxes, can no longer effectively increase the etch rate. That is because now the etch rate is in a "neutral-starved" region, and to further increase the etch rate, additional surface passivation by neutrals is necessary. Since both Cl^+ and Cl fluxes are larger at the wafer edge than those at the wafer center, the etch rates at the wafer edge are larger than those at the wafer center. The relationship between etch rate and neutral and ion fluxes derived from our model agrees very well with what has been obtained semi-empirically by Dane and Mentai [13]. This has been discussed in Section 1.2 and is shown in Fig. 1.4.

Table 3.1. Surface Reaction Mechanism

Gas phase species: Cl_{2g}, Cl_g, Cl^*_g, Cl^+_g, $Cl_2{}^+_g$, Ar_g, Ar^+_g.

Wafer surface species: Si_s, $SiCl_s$, $SiCl_{2s}$, $SiCl_{3s}$, Si_2Cl_{2s}, Si_2Cl_{3s}, Si_2Cl_{4s}.

Wall surface species: W_s, WCl_s, $WSiCl_{2s}$.

Reaction[a, b, c]	Probability	Note
$Cl_g + Si_s \rightarrow SiCl_s$	0.99	
$Cl_g + SiCl_s \rightarrow SiCl_{2s}$	0.2	
$Cl_g + SiCl_{2s} \rightarrow SiCl_{3s}$	0.15	
$Cl_g + SiCl_{3s} \rightarrow Si_s + SiCl_{4g}$	0.001	d
$Cl_g + SiCl_{3s} \rightarrow SiCl_{2s} + Cl_{2g}$	0.08	
$Cl_g + Si_2Cl_{2s} \rightarrow SiCl_s + SiCl_{2g}$	0.008	d
$Cl_g + Si_2Cl_{3s} \rightarrow SiCl_s + SiCl_{2g} + Cl_g$	0.008	d
$Cl_g + Si_2Cl_{4s} \rightarrow SiCl_{2s} + SiCl_{2g} + Cl_g$	0.008	d
$Cl_g + W_s \rightarrow WCl_s$	0.02	
$Cl_g + WCl_s \rightarrow W_s + Cl_{2g}$	0.02	
$Cl^*_g + Si_s \rightarrow SiCl_s$	0.6	
$Cl^*_g + SiCl_s \rightarrow Si_s + SiCl_{2g}$	0.25	d
$Cl^*_g + SiCl_{2s} \rightarrow Si_s + SiCl_{2g} + Cl_g$	0.5	d
$Cl^*_g + SiCl_{3s} \rightarrow Si_s + SiCl_{4g}$	0.5	d
$Cl^*_g + W_s \rightarrow WCl_s$	0.06	
$Cl^*_g + WCl_s \rightarrow W_s + Cl_{2g}$	0.16	
$Cl^*_g + WSiCl_{2s} \rightarrow W_s + SiCl_{2g} + Cl_g$	0.04	
$Cl^+_g + SiCl_s \rightarrow Si_s + SiCl_{2g} + ET$	$p_0 = 0.3$	d, e
$Cl^+_g + SiCl_{2s} \rightarrow Si_s + SiCl_{2g} + Cl_g + ET$	$p_0 = 0.6$	d, e
$Cl^+_g + SiCl_{3s} \rightarrow Si_s + SiCl_{4g} + ET$	$p_0 = 0.6$	d, e
$Cl^+_g + Si_2Cl_{2s} \rightarrow Si_s + SiCl_{2g} + Cl_g$	$p_0 = 0.9$	d, e
$Cl^+_g + Si_2Cl_{3s} \rightarrow SiCl_s + SiCl_{2g} + Cl_g$	$p_0 = 0.99$	d, e
$Cl^+_g + Si_2Cl_{4s} \rightarrow SiCl_{2s} + SiCl_{2g} + Cl_g$	$p_0 = 0.99$	d, e
$Cl^+_g + WCl_s \rightarrow W_s + Cl_{2g}$	$p_0 = 0.8$	

Table 3.1. Continued

Reaction	Probability	Notes
$Cl^+_g + WSiCl_{2s} \rightarrow W_s + SiCl_{2g} + Cl_g$	$p_0 = 0.7$	
$Cl_2{}^+_g + Si_s \rightarrow Si_s + SiCl_{2g} + ET$	$p_0 = 0.002$	d, e
$Cl_2{}^+_g + SiCl_s \rightarrow Si_s + SiCl_{2g} + Cl_g + ET$	$p_0 = 0.25$	d, e
$Cl_2{}^+_g + SiCl_{2s} \rightarrow Si_s + SiCl_{2g} + Cl_{2g} + ET$	$p_0 = 0.6$	d, e
$Cl_2{}^+_g + SiCl_{3s} \rightarrow Si_s + SiCl_{4g} + Cl_g + ET$	$p_0 = 0.6$	d, e
$Cl_2{}^+_g + Si_2Cl_{2s} \rightarrow Si_s + SiCl_{2g} + Cl_{2g}$	$p_0 = 0.9$	d, e
$Cl_2{}^+_g + Si_2Cl_{3s} \rightarrow SiCl_s + SiCl_{2g} + Cl_{2g}$	$p_0 = 0.99$	d, e
$Cl_2{}^+_g + Si_2Cl_{4s} \rightarrow SiCl_{2s} + SiCl_{2g} + Cl_{2g}$	$p_0 = 0.99$	d, e
$Cl_2{}^+_g + WCl_s \rightarrow W_s + Cl_{2g} + Cl_g$	$p_0 = 0.8$	
$Cl_2{}^+_g + WSiCl_{2s} \rightarrow W_s + SiCl_{2g} + Cl_{2g}$	$p_0 = 0.04$	
$Ar^+_g + SiCl_{2s} \rightarrow Si_s + SiCl_{2g} + Ar_g$	$p_0 = 0.4$	d, e
$Ar^+_g + Si_2Cl_{2s} \rightarrow Si_s + SiCl_{2g} + Ar_g$	$p_0 = 0.9$	d, e
$Ar^+_g + Si_2Cl_{3s} \rightarrow SiCl_s + SiCl_{2g} + Ar_g$	$p_0 = 0.99$	d, e
$Ar^+_g + Si_2Cl_{4s} \rightarrow SiCl_{2s} + SiCl_{2g} + Ar_g$	$p_0 = 0.99$	d, e
$Ar^+_g + WCl_s \rightarrow W_s + Cl_g + Ar_g$	$p_0 = 0.4$	
$Ar^+_g + WSiCl_{2s} \rightarrow W_s + SiCl_{2g} + Ar_g$	$p_0 = 0.7$	
$SiCl_{2g} + Si_s \rightarrow Si_2Cl_{2s}$	0.3	f
$SiCl_{2g} + SiCl_s \rightarrow Si_2Cl_{3s}$	0.2	f
$SiCl_{2g} + SiCl_{2s} \rightarrow Si_2Cl_{4s}$	0.1	f
$SiCl_{2g} + W_s \rightarrow WSiCl_{2s}$	0.2	

Notes:

a. Unless otherwise specified, all ions neutralize on all surfaces, returning as their neutral counterparts.
b. The sum of probabilities of gas phase species with surface sites shown here may not sum to unity. The remaining probability is assigned to the incident species reflecting without reaction.
c. All gas phase species have units of flux ($cm^{-2}s^{-1}$). All surface species have units of fractional coverage. Derivatives for surface species are divided by the surface site density T. In this work, $T = 1 \times 10^{15}$ cm^{-2}.
d. Wafer etching step.
e. See Eq. 3.11. $E_r = 50$ eV. $E_{th} = 5$ eV.
f. Etch product redeposition.

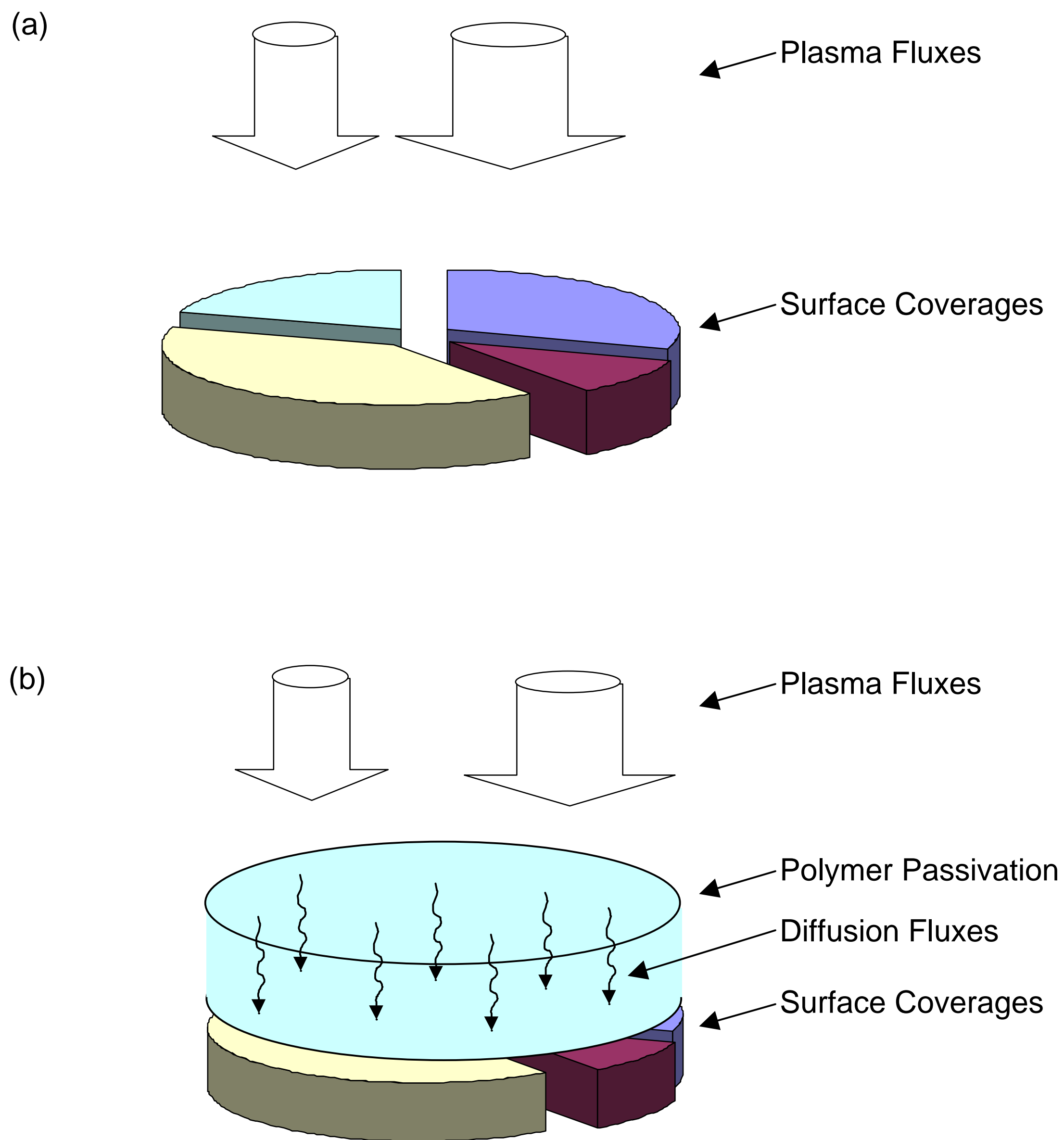

Fig. 3.1. Schematics showing the algorithms for (a) conventional surface site balance model and (b) modified site balance model including polymeric deposition at the surface and diffusion fluxes through the polymer layer.

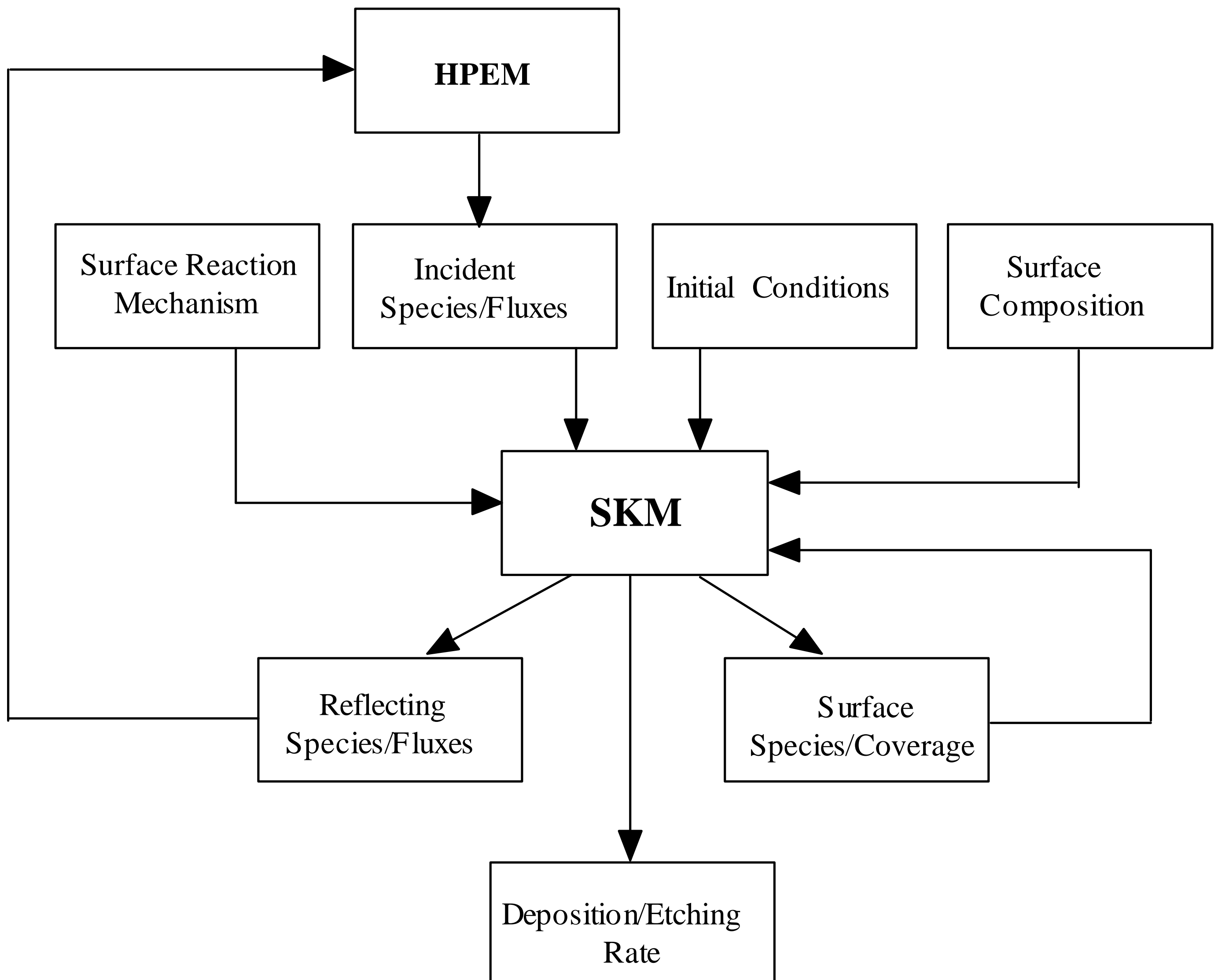

Fig. 3.2. Flow diagram of the integrated plasma-surface model.

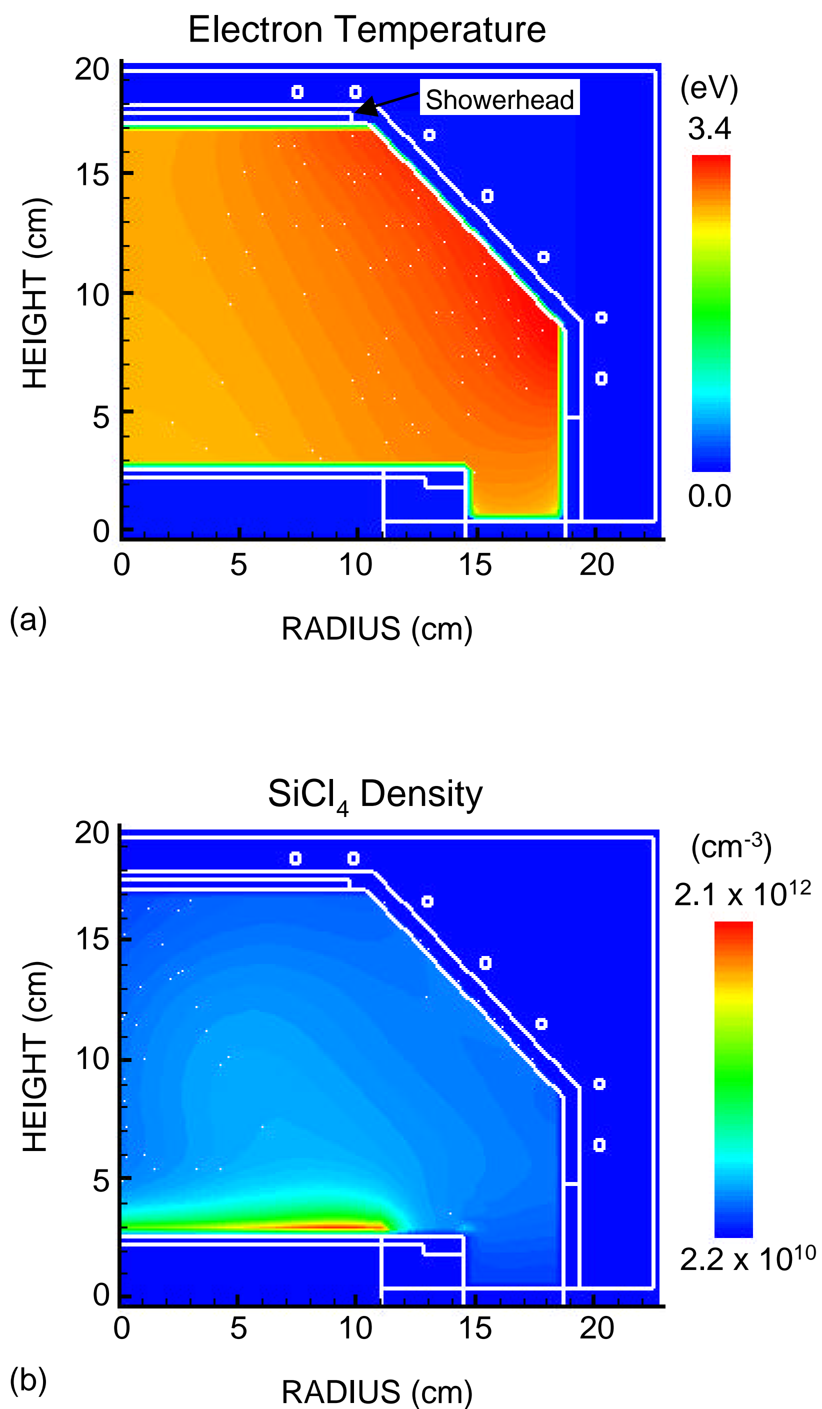

Fig. 3.3. Plasma properties in an Ar/Cl_2 ICP reactor. (a) Electron temperature and (b) $SiCl_4$ densities. Process conditions: Ar/Cl_2 = 70/30, 10 mTorr, 80 sccm.

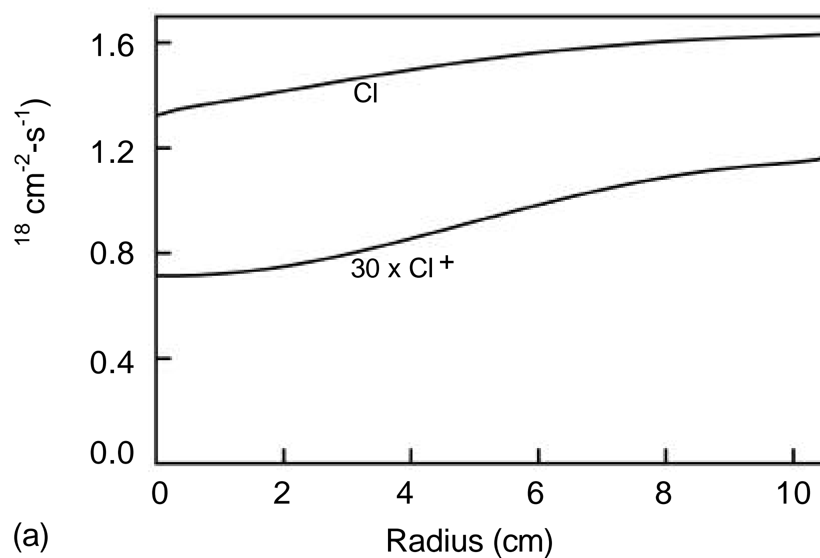

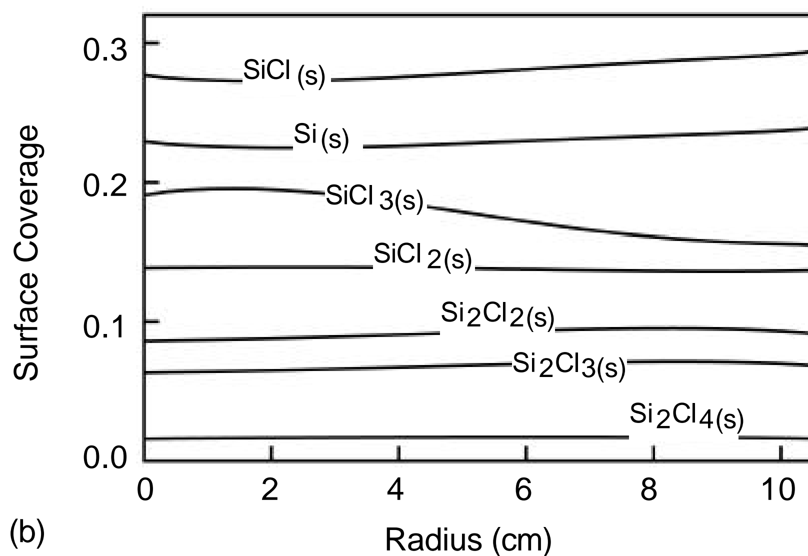

Fig. 3.4. Surface properties in the Ar/Cl_2 reactor. (a) Cl and Cl^+ fluxes to the wafer. The ion flux has been multiplied by a factor of 30. (b) Steady state surface coverages.

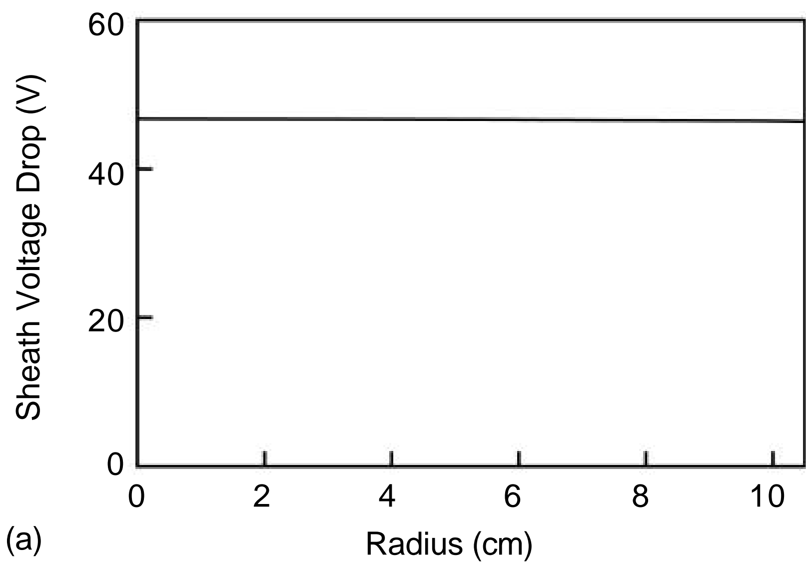

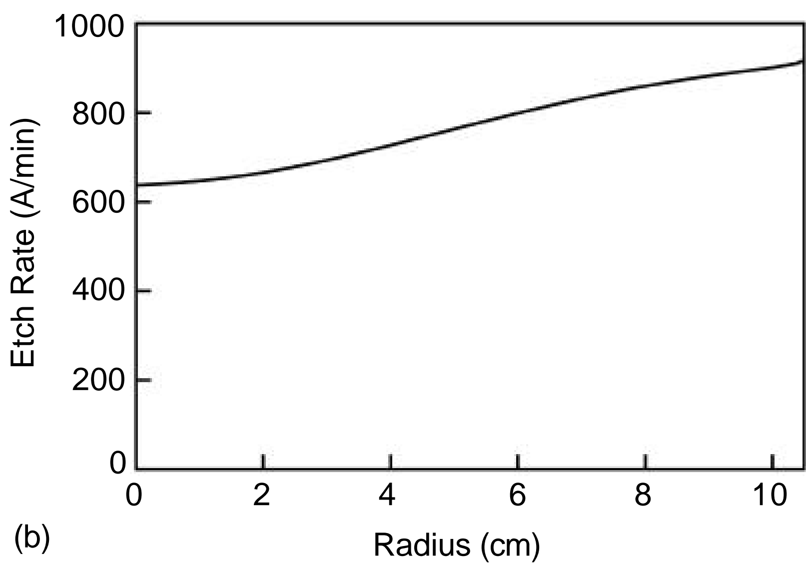

Fig. 3.5. Radial distributions of (a) sheath voltage drop above the wafer and (b) Si etch rate.

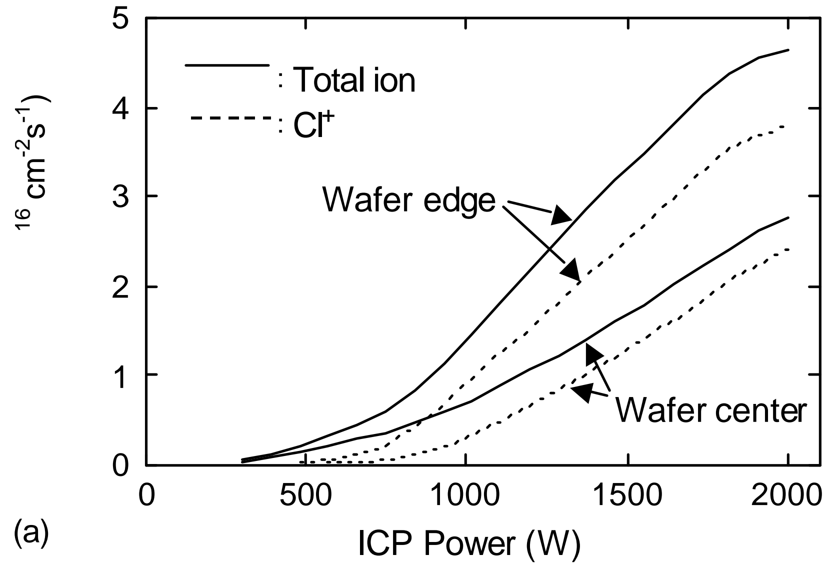

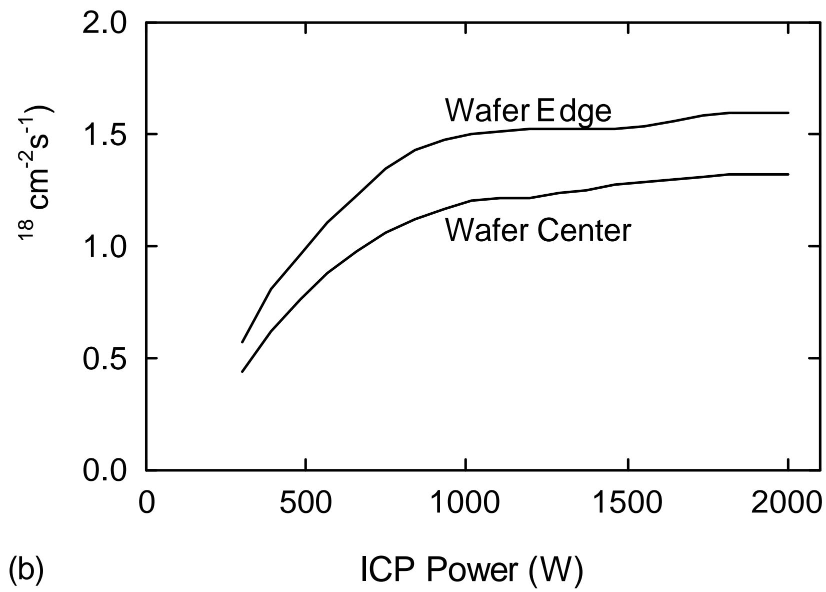

Fig. 3.6. Fluxes of (a) Cl^+ and total ion fluxes, and (b) Cl, at the center and edge of the wafer, as a function of ICP power. In (a) the dashed lines denote Cl^+ fluxes and the solid lines denote total ion fluxes.

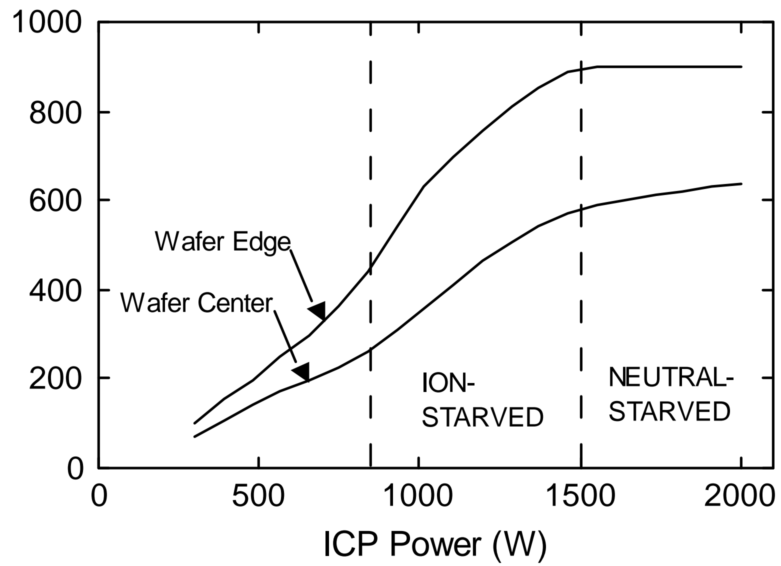

Fig. 3.7. Etch rates at the center and edge of the wafer as a function of ICP power. There are ion-starved and neutral-started regions for the etch rates.

3.4. References

[1] J. T. C. Lee, N. Layadi, K. V. Guinn, H. L. Maynard, F. P. Klemens, D. E. Ibbotson, I. Tepermeister, P. O. Egan, and R. A. Richardson, J. Vac. Sci. Technol. B **14**, 2510 (1996).

[2] B. E. E. Kastenmeier, P. J. Matsuo, G. S. Oehrlein, and J. G. Langan, J. Vac. Sci. Technol. A **16**, 2047 (1998).

[3] K. Nishikawa, T. Oomori, and K. Ono, J. Vac. Sci. Technol. B **17**, 127 (1999).

[4] M. Shaepkens, R. C. M. Bosch, T. E. F. M. Standaert, and G. S. Oehrlein, J. Vac. Sci. Technol. A **16**, 2099 (1998).

[5] T. E. F. M. Standaert, M. Schaepkens, N. R. Rueger, P. G. M. Sebel, G. S. Oehrlein, and J. M. Cook, J. Vac. Sci. Technol. A **16**, 239 (1998).

[6] N. R. Rueger, J. J. Beulens, M. Schaepkens, M. F. Doemling, J. M. Mirza, T. E. F. M. Standaert, and G. S. Oehlein, J. Vac. Sci. Technol. A **15**, 1881 (1997).

[7] W. Z. Collison, T. Q. Ni, and M. S. Barnes, J. Vac. Sci. Technol. A **16**, 100 (1998).

[8] N. Mantzaris, A. Boudouvis, and E. Gogolides, J. Appl. Phys. **77**, 6169 (1995).

[9] E. Meeks, R. S. larson, S. R. Vosen, and J. W. Shon, J. Electronchem. Soc. **144**, 357 (1997).

[10] B. A. Helmer and D. B. Graves, J. Vac. Sci. Technol. A **16**, 3502 (1998).

[11] D. E. Hanson, A. F. Voter, and J. D. Kress, J. Appl. Phys. **82**, 3552 (1997).

[12] C. F. Abrams and D. B. Graes, J. Appl. Phys. **86**, 2263 (1999).

[13] D. Dane and T. D. Mentai, Appl. Phys. Lett. **65**, 478 (1994).

4. MECHANISMS FOR CF_2 RADICAL GENERATION AND LOSS ON SURFACES IN FLUOROCARBON PLASMAS

4.1. Introduction

Fluorocarbon plasmas are widely used for silicon and silicon dioxide etching in microelectronics fabrication due to their high rates of etching and selectivity [1-2]. Investigating surface reactions in these plasmas continues to be of interest because, in addition to their direct effects on the etch process, they influence bulk plasma species densities which feed back to etch properties [3-7]. Of particular interest are surface reactions involving CF_2, as CF_2 is a precursor for wafer passivation. Controlling its density is therefore essential to obtaining desirable etch properties. Experiments have demonstrated that surfaces in fluorocarbon plasmas can act as both sinks and sources of CF_2. For example, Fisher et al. observed that beams of fluorocarbon radicals incident on polymerized surfaces produce additional CF_2 [8]. These results imply that reactions of C_xF_y radicals other than CF_2 produced that species at the surface. On the other hand, Sugai et al. measured a decrease in CF_2 density approaching the substrate in a capacitively coupled radio frequency (rf) plasma reactor, indicating that the surface acts as a sink [9]. This discrepancy can be explained by realizing that reactions resulting in the generation and consumption of radicals simultaneously occur at the surface, and it is the relative magnitudes of these processes that determine whether the surface is a net source or sink of CF_2. In fact, a surface in contact with the same plasma chemistry can act as both a source and a sink under different process conditions. These trends have been demonstrated by experiments by Booth et al [5]. They showed that in an rf discharge sustained in CF_4, the powered electrode was a CF_2 source at high bias power while the opposite grounded electrode was a sink. The powered electrode turned into a sink when the power was decreased.

In this chapter, the coupling of surface and plasma reactions is investigated using the integrated plasma-surface model described in Chapter 3.[10-12] The system of interest here is a capacitively coupled discharge sustained in CF_4 to enable comparison to Booth's experiments [5]. The surface processes responsible for CF_2 generation and consumption were investigated. We found that CF_2 formation by energetic ion bombardment can exceed CF_2 sticking losses at biased surfaces, making the surfaces a CF_2 source. With decreasing substrate bias, the CF_2 yield by ion-surface interactions decreases due to decreasing ion bombardment energy. The character of the surface (source or sink) is a function of pressure since the ratio of neutral to ion fluxes is pressure dependent. The surface reaction mechanism for CF_2 production in a CF_4 plasma is discussed in Section 4.2. Results for an rf CF_4 discharge are reported and discussed in Section 4.3. Concluding remarks are in Section 4.4.

4.2. CF_4 Plasma and Surface Reaction Mechanisms for CF_2 Production

Fluorocarbon plasmas are typically used for dielectric etching because of their high etch rates and favorable etch selectivity of SiO_2 over Si [1,2]. The complexity of fluorocarbon plasmas comes from the fact that many types of radicals and ions coexist and contribute differently to surface processes, resulting in simultaneous deposition of polymer passivation layers at surfaces (walls and wafer) during wafer etching [14-15]. The etch rate of Si or SiO_2 is sensitive to the thickness of the polymeric layer which is formed by C_xF_y deposition, usually decreasing with increasing polymer thickness. On the other hand, polymer passivation of the sidewall helps in obtaining anisotropic etch profiles. CF_2 radicals are precursors for both polymer deposition and SiO_2 etching, and so controlling the density of CF_2 is essential to

controlling etch properties. Surface reactions have the potential of either depleting or enhancing local CF_2 densities [4-5, 8-9, 16].

Experimental evidence of these surface processes is usually obtained by measuring the slope of the CF_2 gas phase density at the surface. A negative slope (decreasing density to the surface) indicates a net flux into the surface, or a sink. A positive slope indicates a source. As a neutral species, CF_2 radicals incident on a surface can chemisorb, thereby decreasing CF_2 density in the plasma region near the surface. One possible source for CF_2 near the surface is the dissociation of large C_xF_y neutrals by energetic ion collisions in the plasma sheath region [17]. In low pressure discharges, the sheath thickness is typically smaller than the mean free paths for ion collisions, and so this source is likely to be small. Reactions *at* the surface are more likely to be sources of CF_2.

In the steady state, the surface is partially or fully covered by polymers deposited from C_xF_y neutrals [8]. Energetic ion sputtering of the polymer layer can generate CF_2 radicals by bond breaking reactions. A net source of CF_2 by this process requires that deposition of the polymer layer be predominantly by C_xF_y radicals other than CF_2. Energetic ion bombardment on the surface (bare or polymer passivated) can also produce CF_2 by neutralization of CF_2^+ ions and dissociation of $C_xF_y^+$ ions. This process is, in principle, independent of the polymer coverage of the surface, so it can occur from all surfaces. The net effect of a surface on the production of CF_2 is then dependent on the relative strengths of the consumption and generation of CF_2 by these processes.

A reaction mechanism has been developed for a nonetching surface for a CF_4 plasma to account for these plasma-surface interactions. The mechanism is shown schematically in Fig. 4.1. The surface reactions are listed in Table 4.1, with reaction probabilities for the base case

which will be discussed in Section 4.3. Starting from a bare surface, C_xF_y neutral fluxes (CF, CF_2, C_2F_4, C_2F_5) can stick to the surface to form a polymer layer. C_xF_y fluxes incident on the polymer can also stick. F atoms etch the polymer layer and ion sputtering of the polymer layer erodes the polymer to produce a CF_2 flux from the surface. With the growth of the polymer layer, the polymer consumption by ion sputtering and F atom etching increases, and a steady state polymer coverage is reached where there is no net polymer growth. Large ions (CF_3^+, $C_2F_4^+$, $C_2F_5^+$) bombarding a bare or polymer-covered surface can dissociate to return CF_2 radicals to the plasma. The probabilities of these ion-surface interactions are ion energy dependent as described by Eq. 3.11.

There is considerable discussion in the literature on the sticking coefficient of CF_2 on surfaces in fluorocarbon plasmas. Goto et al. [18] and Sawin et al. [19] estimated that in the absence of ion activation of surface site, the sticking probability of CF_2 is small ($\sim 10^{-3}$). These results imply that any surface that appears to be a sink for CF_2 requires coincident ion bombardment. There is evidence from the work of Oehrlein et al. [20] that this apparent sticking is preferentially initiated by low energy ion bombardment which activates sticking on other polymers. On the other hand, the work of Booth et al. [5] indicates there is net sticking of CF_2 to surfaces when power is removed from his reactor. Granted there could be a small flux of low-energy ions which continue to initiate sticking sites late into the afterglow, though this is unlikely. Given these contradictory results, we choose to express CF_2 sticking in terms of an effective coefficient which may include some degree of ion activation.

The gas phase chemistry used in the simulation is summarized in the Appendix. The formation of CF_2 radicals mainly comes from electron impact dissociation of CF_4, CF_3, and C_2F_4. For the conditions in this work, CF_3^+ is the dominant ion.

4.3. CF_2 Production and Loss in an rf CF_4 Discharge

The capacitively coupled rf discharge used in this study is patterned after Booth et al. [5] and is shown schematically in Fig. 4.2. The reactor is cylindrical with a radius of 14.5 cm. The radius of the lower electrode (3 cm from the reactor bottom) is 5.5 cm, and the radius of the upper electrode, which is 3.3 cm above the lower electrode, is 14 cm. An rf bias at 13.56 MHz is applied to the lower electrode, which is surrounded by a dark space shield. The top and side walls of the reactor are grounded. Pure CF_4 gas is supplied through the top showerhead and is pumped from the bottom outlet. No wafer is used in the reactor. The base case conditions are CF_4 at 50 mTorr, 30 sccm gas flow rate, 250 V rf bias amplitude, and surface reaction probabilities as shown in Table 4.1.

CF_2 and CF_3^+ densities for the base case are shown in Fig. 4.2. The two densities peak close to the edge of the powered electrode due to electric field enhancement near the corner of the electrode. As a result the electron temperature in that region is also higher, as shown in Fig. 4.2c. For this case, the CF_2 density is highest near the powered surface, indicating that surface reactions there produce a net source of CF_2.

The axial CF_2 densities at a radius of 3.5 cm are shown in Fig. 4.3(a) for substrate biases of 30 - 250 V. On the grounded upper electrode, CF_2 densities decrease from the bulk plasma to the surface for all biases, indicating a sink. On the powered lower electrode, the CF_2 density is maximum at the surface for high bias, indicating a source. With decreasing substrate bias, the slope of axial CF_2 density decreases and eventually is negative at sufficiently low biases, indicating a sink. For example, the CF_2 density at 30 V bias is shown in Fig. 4.3(b), and shows a peak in the density in the bulk plasma.

The variation of substrate bias has two major effects on the CF_2 density. First, the power deposition increases with increasing bias, resulting in more dissociation and more production of CF_2 in the gas phase. The increase in power produces increases of CF_2 and ion densities in approximately the same proportion. As a result, the relative strengths of CF_2 loss and generation at the surface are unchanged. The second effect of varying bias is the change in plasma sheath voltages at surfaces. At 13.56 MHz, the time-averaged sheath voltage drop increases with increasing bias amplitude, thereby increasing the incident ion energies. Since sputter yields increase with energy,[13] thereby increasing CF_2 production, the spatial distribution of CF_2 can be a function of bias.

The sheath voltage drops as a function of substrate bias on both the powered and grounded electrodes at a radius of 3.5 cm are in Fig. 4.4. Due to the unequal areas of the grounded electrode and the biased electrode, there is a large dc bias on the powered electrode. This increases the sheath voltage drop at the powered electrode relative to that at the grounded electrode. For all biases from 30 to 250 V, the sheath voltages at the grounded electrode are low and near the threshold energies of ion sputtering or ion dissociation, having a maximum of only ≈ 25 V. This leads to small rates of ion-surface reactions, and so CF_2 generation rates are also small. For such conditions, the CF_2 sticking at the grounded surface dominates and the net effect of the grounded surface is as a sink for CF_2.

At the powered electrode, when the bias is 30 V the resulting average sheath potential is only ≈ 20 V, so the ion bombardment energy is low, making the surface a sink for CF_2. As the bias is increased to 100 V, the average sheath potential increases to 78 V, which is large enough to make the CF_2 generation rate by ion bombardment comparable with the rate of CF_2 sticking. As a result the axial CF_2 density profile is nearly flat at the surface. With a further increase of

the substrate bias, the CF_2 generation rate exceeds its sticking loss, and so the surface acts as a net source for CF_2. The CF_2 density then increases from the plasma region to the surface. The slope of the axial CF_2 density increases with bias due to the increasing CF_2 yield by ion bombardment.

The model results were validated by comparing to the experimental data of Booth et al. [5]. To compare to Booth's transient experiments , we performed simulations at 100 W rf bias until the plasma reached a steady state. The source power was then turned off and the simulation was continued for several milliseconds. Simulated and experimental CF_2 axial densities at 100 W and after power was turned off are shown in Fig. 4.5. When the power is on, CF_2 densities decrease from the powered lower electrode to the grounded upper electrode for both simulation and experiments, indicating a source of CF_2 at the powered electrode and a sink at the grounded electrode. When the power is turned off, the initially powered electrode transitions into a CF_2 sink, and so CF_2 densities decrease at the lower electrode as well as at the upper electrode. The simulation reproduced the experimental trends.

Gas pressure is an important process parameter due to its direct effect on the source neutral density, and its influence on plasma transports and species densities. We simulated discharges at 30, 50, and 70 mTorr while keeping other parameters the same as those in the base case. The resulting CF_2 densities and CF_2 source functions are shown in Figs. 4.6 and 4.7 respectively. The peak CF_2 density increases with pressure due to both a larger and more confined source and a lower rate of diffusion. At high pressure (70 mTorr), the peak CF_2 source occurs at a larger radius due to electric field enhancement and localized power deposition. As the pressure decreases, the electron energy relaxation length increases, and diffusion rates increase, resulting in the peak CF_2 area expanding to the reactor center. At all pressures the CF_2

densities are maximum at the surface of the powered electrode, implying a net CF_2 source there resulting from the high bias of 250 V. Axial CF_2 densities at a radius of 3.5 cm for 30, 50, and 70 mTorr are shown in Fig. 4.8(a). The powered electrode is a net source of CF_2 in all cases. The strength of the source is indicated by the slope of the density at the surface. At 30 mTorr, the slope is the steepest, becoming shallower with increasing pressure.

Pressure can impact the plasma floating potential through the electron temperature. Lower pressures imply higher electron temperatures and larger floating potentials. Since the floating potential is small compared with the applied bias (250 V), and since the sheath is largely noncollisional at these pressures, the majority of the plasma sheath potential comes from the bias. The influence of pressure on the incident ion energy is therefore weak. The ratio of ion to neutral fluxes to the surface, however, can change significantly with pressure. For example, after being normalized to the value at 30 mTorr, the ratios of ion to neutral fluxes at different pressures are shown in Fig. 4.8(b). The ratio decreases with increasing pressure, which means the CF_2 generation by ion bombardment decreases with increasing pressure relative to CF_2 sticking. Therefore the surface progressively appears as a sink, as indicated by the slopes in Fig. 4.8(b).

CF_2 generation comes from ion sputtering and ion dissociation, and so the probabilities of these processes determine the strength of the CF_2 source. Ion sputtering of CF_2, unlike ion dissociation, also depends on the polymer coverage. Thus far, we used $p_0 = 0.45$ for ion dissociation and $p_0 = 0.4$ for ion sputtering. (The final reaction probability is obtained from Eq. 3.11. For both processes $E_r = 150$ eV and $E_{th} = 5$ eV were used.) The polymer coverage for the base case is close to unity at ≈ 0.9. So the relative contributions of ion sputtering and ion dissociation to CF_2 generation are estimated to be $\approx 0.36 : 0.45$ or $4 : 5$. Given the fact that some

surface reaction probabilities change with process conditions (e.g., CF_2 sticking coefficients being a function of surface temperature [7]), and considering the uncertainty in selecting coefficients for the model, it is valuable to investigate the sensitivity of the simulation to the selection of coefficients. Axial CF_2 densities at a radius of 3.5 cm for different p_0 for ion dissociation are shown in Fig. 4.9(a). The CF_2 density at the powered electrode as a function of p_0 is plotted in Fig. 4.9(b). Other parameters are the same as in the base case. For small dissociation probabilities (0.1, 0.3), the powered surface acts as a sink for CF_2. CF_2 sources are dominated by sputtering, which is insufficient to produce a net source. When the dissociation probability is large enough, the powered surface becomes a CF_2 source. However on the grounded side, since the CF_2 generation by ion bombardment is negligible in all cases, the ion dissociation probability has little influence on the slope of the CF_2 density at that electrode.

The sensitivity of the model to the effective CF_2 sticking coefficient α was also investigated. The axial CF_2 densities at a radius of 3.5 cm are shown in Fig. 4.10(a) for CF_2 sticking coefficients from 0.05 to 0.6 (the base case value is 0.1). Large sticking coefficients ($\alpha \geq 0.2$) result in a net CF_2 loss at the surface, so the CF_2 density decreases with increasing sticking coefficient at both powered and grounded electrodes. As the sticking coefficient drops to $\alpha = 0.1$, the CF_2 generation rate exceeds the loss rate at the powered surface, and so the CF_2 density increases from the plasma region to the surface. At the grounded electrode, the CF_2 sticking always dominates as there is little effect by ion-surface reactions. The CF_2 density therefore decreases towards the surface in all cases. Sticking coefficients of $\alpha < 0.1$ are typically required for surfaces to be net sources for these biases. The CF_2 densities as a function of sticking coefficients at the powered surface (height = 3.0 cm) and in the bulk region (height = 3.8 cm) are

shown in Fig. 4.10(b). The density drops with increasing sticking coefficient at both locations. The density at the surface drops more rapidly due to the proximity of CF_2 consuming reactions.

The production of CF_2 is sensitive to both the ion dissociation probability p_0 and the CF_2 sticking coefficient α. The combined effects of p_0 and α on the slope of the CF_2 density approaching the surface were investigated statistically using a design of experiment (DOE) method, implemented in the commercial software ECHIP [21]. The results are shown in Fig. 4.10(c). The slopes (S) are labeled on the response lines with a unit of 10^{12} cm^{-4}. The S = 0.0 line defines the boundary between the source and sink regions, with $S > 0$ indicating a source and $S < 0$ a sink. S is more sensitive to α than to p_0, since the neutral flux is larger than the ion flux at the surface. The general trend is that increasing p_0 and decreasing α produce a surface source of CF_2.

4.4. Concluding Remarks

The integrated surface kinetics and plasma equipment model, HPEM-SKM, was used to investigate the effect of ion and neutral reactions at the surface of an rf CF_4 discharge on the CF_2 density. CF_2 sticking is a loss at the surface, while ion sputtering of deposited polymer layers and ion dissociation can generate CF_2. The net effect of the surface then depends on the relative rates of the CF_2 loss and ion generation. The reaction probabilities of ion-surface reactions increase with increasing incident ion energy, and so a surface can transition from a net CF_2 sink at low bias to a net CF_2 source at high bias. The ratios of ion flux to CF_2 density near a surface are a function of pressure, and this leads to different CF_2 density profiles near the surface at different pressures. The sensitivities of the model on rate coefficients were analyzed. Large ion dissociation probabilities and small CF_2 sticking coefficients produce a CF_2 source at the surface.

Table 4.1. Surface Reaction Mechanism

Species Definitions:

X_g	Gas phase species
W_s	Bare surface site
P_s	Polymer passivated surface site

Reaction[a, b]	Probability	Note
$CF_{2g} + W_s \rightarrow P_s$	0.1	c, i
$CF_{2g} + P_s \rightarrow P_s + P_s$	0.1	d, i
$CF_g + W_s \rightarrow P_s$	0.1	c
$CF_g + P_s \rightarrow P_s + P_s$	0.1	d
$C_2F_{4g} + W_s \rightarrow P_s + P_s$	0.03	c
$C_2F_{4g} + P_s \rightarrow P_s + P_s + P_s$	0.03	d
$C_2F_{5g} + W_s \rightarrow P_s + P_s$	0.025	c
$C_2F_{5g} + P_s \rightarrow P_s + P_s + P_s$	0.025	d
$CF_3{}^+{}_g + W_s \rightarrow CF_{2g} + F_g + W_s$	$p_0 = 0.45$	e, f, i
$CF_3{}^+{}_g + P_s \rightarrow CF_{3g} + CF_{2g} + W_s$	$p_0 = 0.4$	e, g
$CF_3{}^+{}_g + P_s \rightarrow CF_{2g} + F_g + P_s$	$p_0 = 0.45$	e, f, i
$C_2F_4{}^+{}_g + W_s \rightarrow CF_{2g} + CF_{2g} + W_s$	$p_0 = 0.45$	e, f
$C_2F_4{}^+{}_g + P_s \rightarrow C_2F_{4g} + CF_{2g} + W_s$	$p_0 = 0.4$	e, g
$C_2F_4{}^+{}_g + P_s \rightarrow CF_{2g} + CF_{2g} + P_s$	$p_0 = 0.45$	e, f
$C_2F_5{}^+{}_g + W_s \rightarrow CF_{2g} + CF_{3g} + W_s$	$p_0 = 0.45$	e, f
$C_2F_5{}^+{}_g + P_s \rightarrow C_2F_{5g} + CF_{2g} + W_s$	$p_0 = 0.4$	e, g
$C_2F_5{}^+{}_g + P_s \rightarrow CF_{2g} + CF_{3g} + P_s$	$p_0 = 0.45$	e, f
$F_g + P_s \rightarrow CF_{4g} + P_s$	0.001	h

Notes:

a. Unless otherwise specified, all ions neutralize on all surfaces, returning as their neutral counterparts.

b. All gas phase species have units of flux ($cm^{-2}s^{-1}$). All surface species have units of fractional coverage.

Table. 4.1. Continued

c. Neutral sticking to bare surface.
d. Neutral sticking to polymer passivated surface.
e. See Eq. 3.11. E_r = 150 eV, E_{th} = 5 eV.
f. Ion dissociation at surface.
g. Ion sputtering of polymer passivated surface.
h. F atom etching of the polymer layer.
i. Base case value.

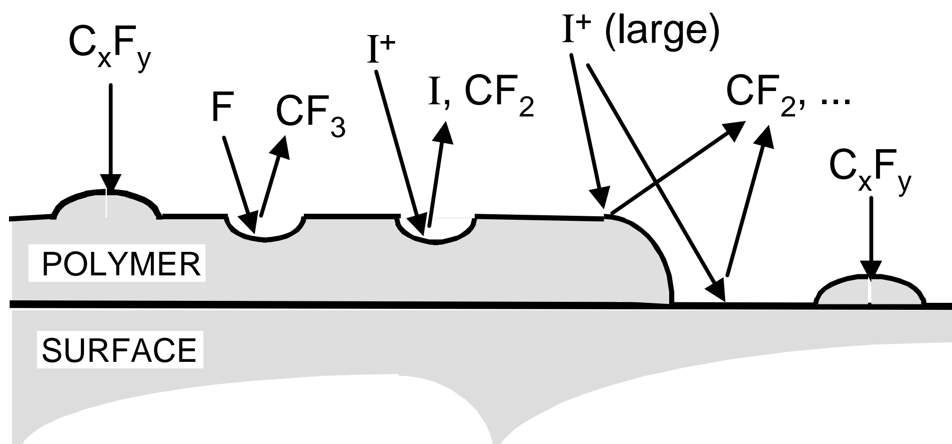

Fig. 4.1. Schematic of the surface reaction mechanism for a CF_4 discharge without etching. I^+ represents an ion species. Large I^+ species include CF_3^+, $C_2F_4^+$, and $C_2F_5^+$ which can dissociate to form CF_2.

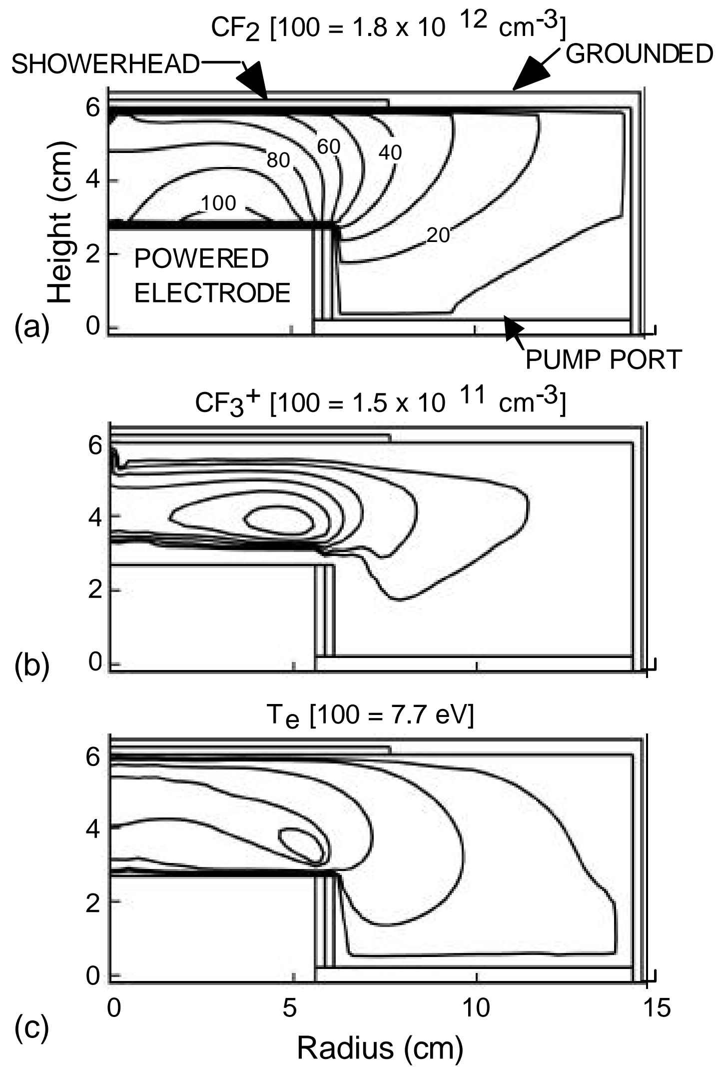

Fig. 4.2. Densities of (a) CF_2, (b) CF_3^+, and (c) electron temperature T_e in the rf reactor for the base case conditions (50 mTorr, 250 V bias, 30 sccm, surface reaction probabilities as shown in Table 4.1). The labels on the contour lines denote the percentage of the value shown at the top of each figure. Electric field enhancement produces peak values near the edge of the electrodes.

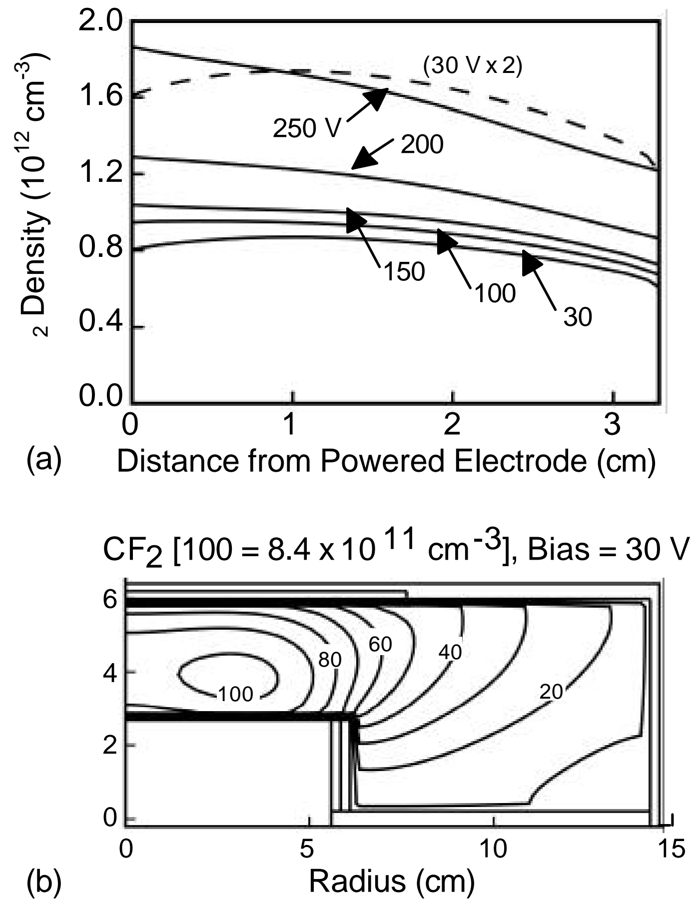

Fig. 4.3. CF_2 for different biases. (a) Densities at r = 3.5 as a function of height. (b) CF_2 density for 30 V bias. All cases are at 50 mTorr and 30 sccm. Increasing the bias increases the source of CF_2 at the powered electrode.

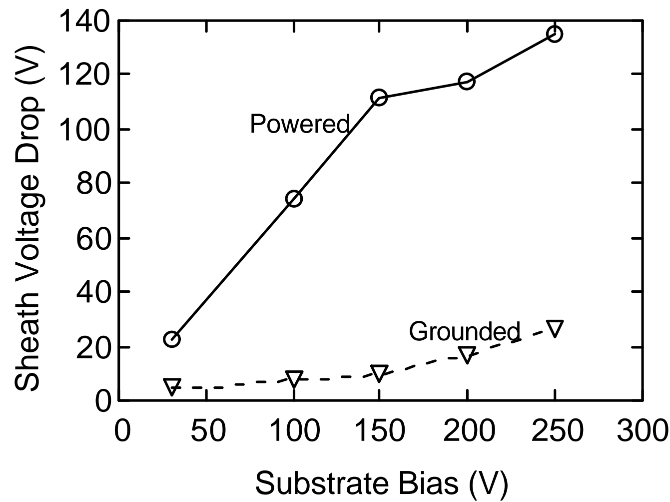

Fig. 4.4. Time averaged sheath voltage drop as a function of the substrate bias at the powered and the grounded surfaces. The sheath at the grounded electrode remains sufficiently low that the surface always appears to be a sink for CF_2.

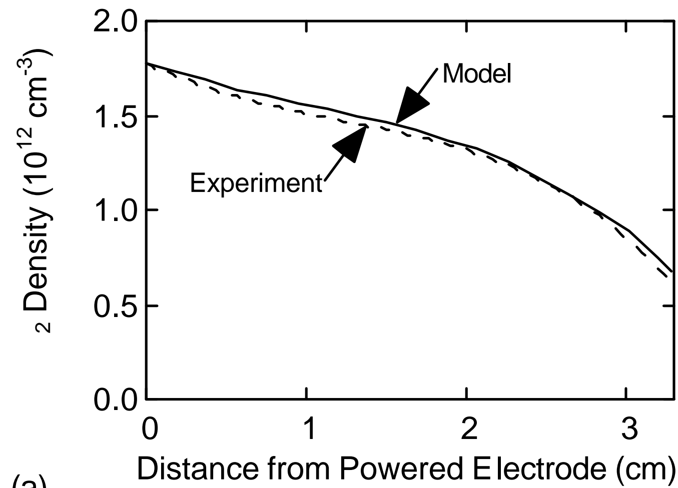

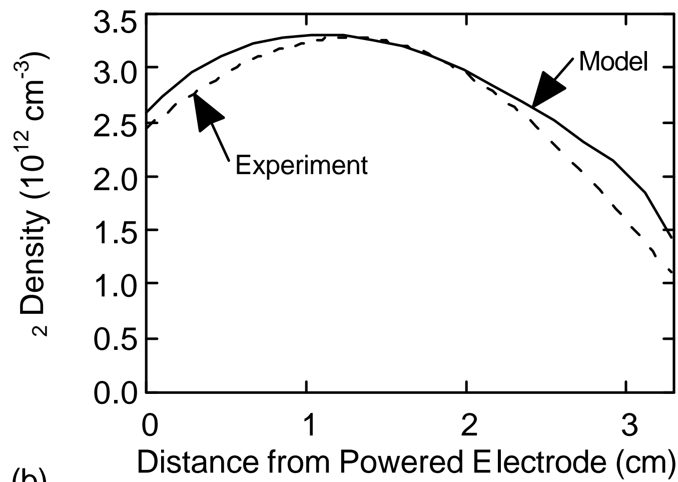

Fig. 4.5. Axial CF_2 densities at (a) 100 W rf power and (b) after the power is turned off. The solid lines are simulation results and the dashed lines are experimental results from Booth [5].

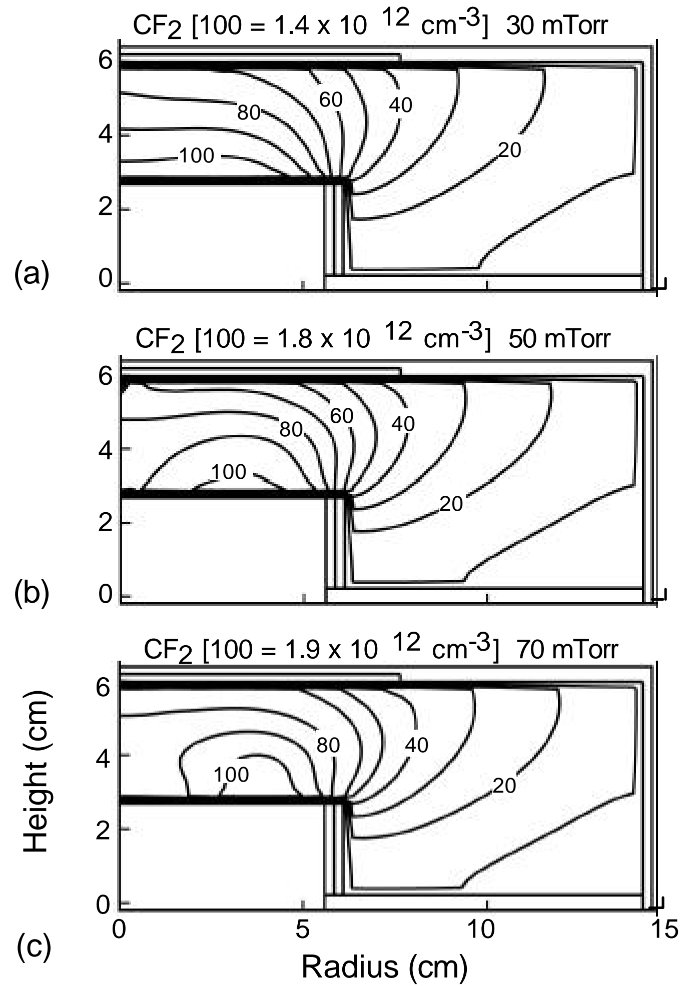

Fig. 4.6. CF_2 density distributions at (a) 30, (b) 50, and (c) 70 mTorr. All cases are at 250 V biases and 30 sccm. The labels on the contour lines denote the percentage of the value shown at the top of each figure. Increasing pressure localizes sources closer to the powered electrode.

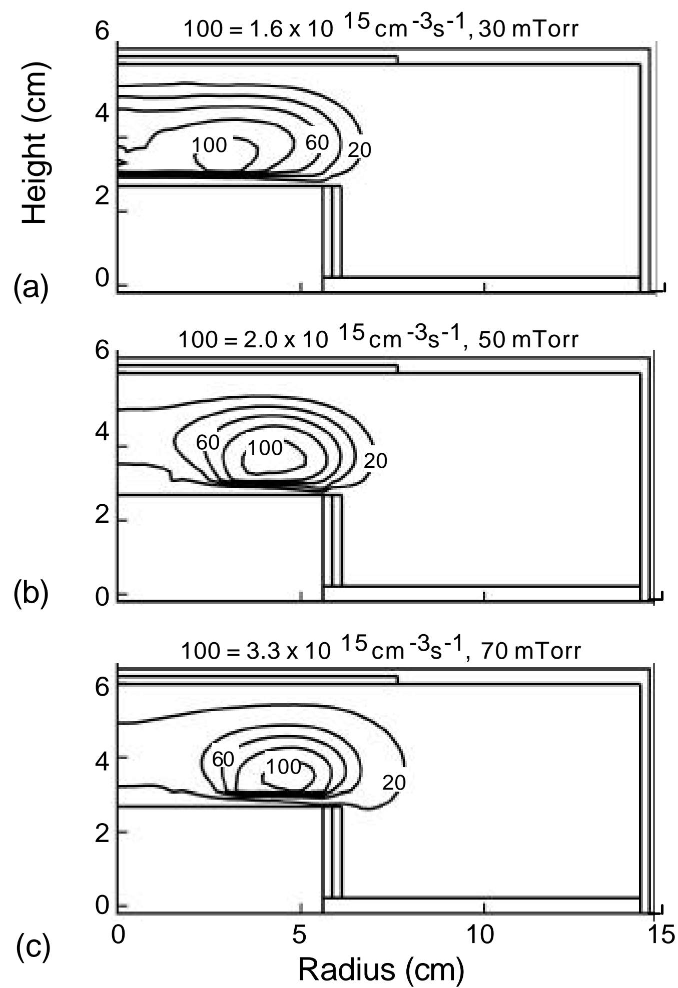

Fig. 4.7. CF_2 source functions at (a) 30, (b) 50, and (c) 70 mTorr. The conditions are the same as for Fig. 4.6. Increasing pressure shifts the maximum in the source to larger radius.

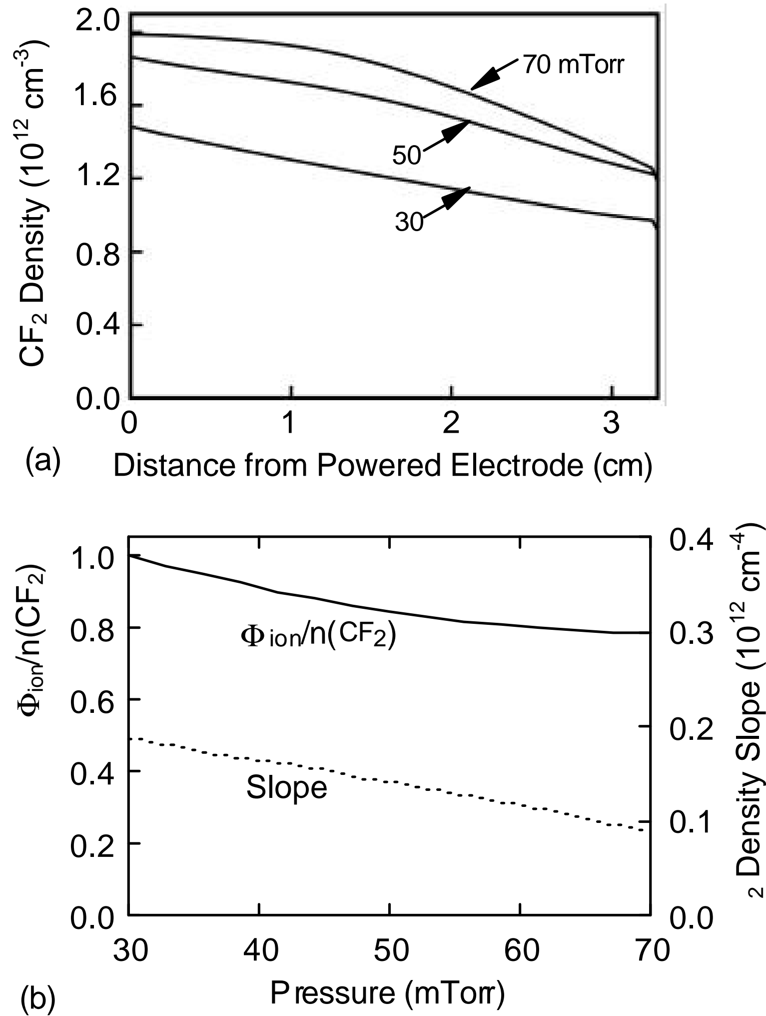

Fig. 4.8. CF_2 properties as a function of pressure. (a) Axial CF_2 densities at r = 3.5 cm for 30, 50, and 70 mTorr. (b) The ratio of ion flux to CF_2 density, and the slope of the CF_2 density, at the powered electrode surface of r =3.5 cm, as a function of pressure. The values of the ratios of ion flux to CF_2 density are normalized to that at 30 mTorr. The increase in pressure reduces the ion flux relative to the neutral flux, and as a result weakens the net source of CF_2, as indicated by the reduction in slope.

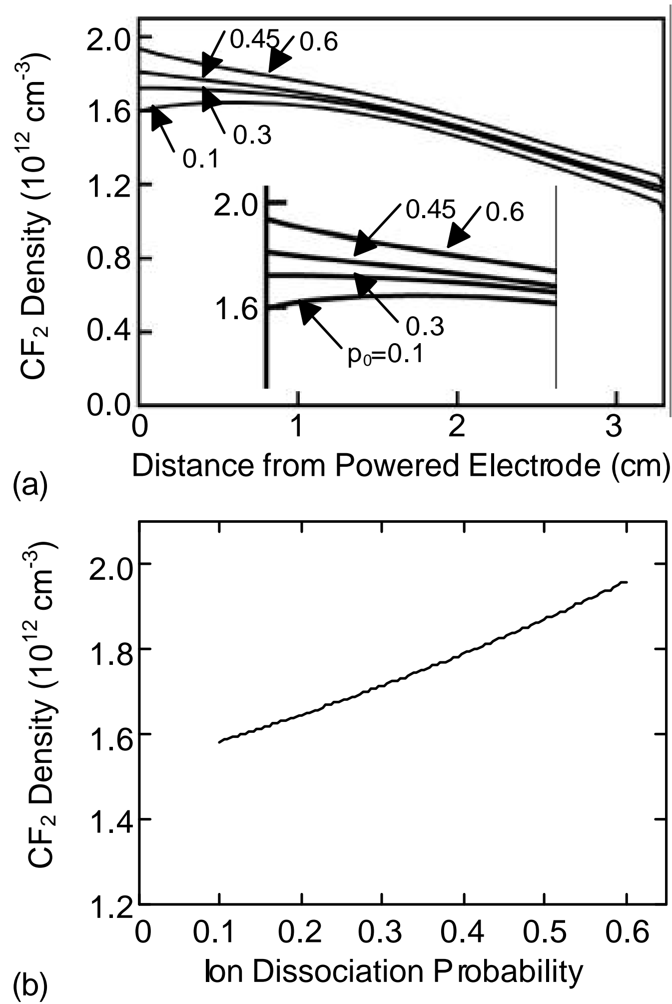

Fig. 4.9. CF_2 properties as a function of ion dissociation probability. (a) Axial CF_2 densities at r = 3.5 cm for different ion dissociation probabilities. All cases are at 50 mTorr, 250 V bias, and 30 sccm. (b) The CF_2 density at z = 3 cm as a function of the ion dissociation probability at the surface. Increasing the ion dissociation probability increases the net source of CF_2.

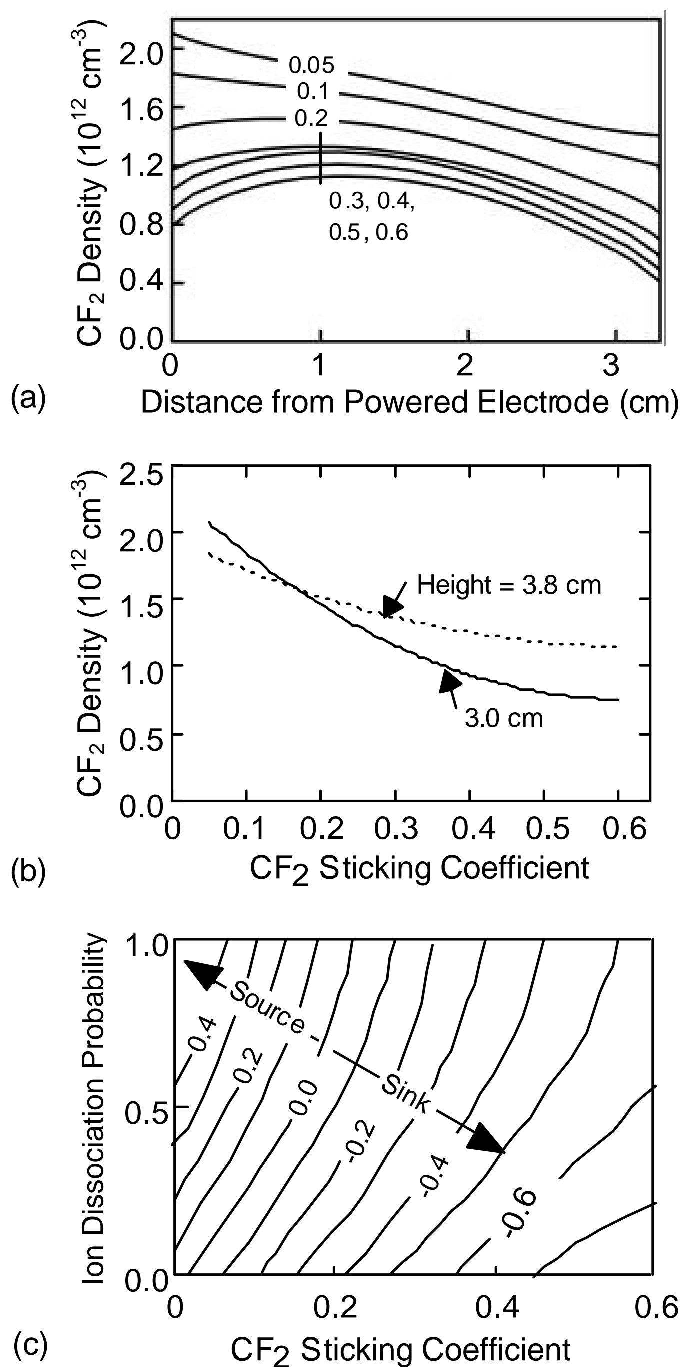

Fig. 4.10. CF_2 properties as a function of sticking probability. (a) Axial CF_2 density distributions at r = 3.5 cm for different CF_2 sticking coefficients at the surface. All cases are at 50 mTorr, 250 V bias, and 30 sccm. (b) The CF_2 densities at z = 3 cm and z = 3.8 cm as a function of the CF_2 sticking coefficient. (c) The slope of the CF_2 density approaching the powered surface as a function of the CF_2 sticking coefficient and the ion dissociation probability. The slopes are labeled on the response lines with a unit of 10^{12} cm^{-4}.

4.5. References

[1] N. R. Rueger, M. F. Doemling, M. Schaepkens, J. J. Beulens, T. E. F. M. Standaert, and G. S. Oehrlein, J. Vac. Sci. Technol. A **17**, 2492 (1999).

[2] T. E. F. M. Standaert, M. Schaepkens, N. R. Rueger, P. G. M. Sebel, G. S. Oehlein, and J. M. Cook, J. Vac. Sci. Technol. A **16**, 239 (1998).

[3] J. A. O'Neil and J. Singh, J. Appl. Phys. **77**, 497 (1995).

[4] G. M. W. Kroesen, H. Lee, H. Moriguchi, H. Motomura, T. Shirafuji, and K. Tachibana, J. Vac. Sci. Technol. A **16**, 225 (1998).

[5] J. P. Booth, G. Cunge, P. Chabert, and N. Sadeghi, J. Appl. Phys. **85**, 3097 (1999).

[6] G. Cunge and J. P. Booth, J. Appl. Phys. **85**, 3952 (1999).

[7] M. Schaepkens, R. C. M. Bosch, T. E. F. M. Standaert, and G. S. Oehrlein, J. Vac. Sci. Technol. A **16**, 2099 (1998).

[8] N. E. Capps, N. M. Mackie, and E. R. Fisher, J. Appl. Phys. **84**, 4376 (1998).

[9] Y. Hikosaka, H. Toyota, and H. Sugai, Jpn. J. Appl. Phys., Part 2 **32**, L353 (1993).

[10] S. Rauf and M. J. Kushner, J. Appl. Phys. **83**, 5087 (1998).

[11] M. J. Grapperhaus and M. J. Kushner, J. Appl. Phys. **81**, 569 (1997).

[12] D. Zhang and M. J. Kushner, J. Appl. Phys. **87**, 1060 (2000).

[13] C. F. Adams and D. B. Graves, J. Appl. Phys. **86**, 2263 (1999).

[14] A. J. Bariya, C. W. Frank, and J. P. McVittie, J. Electrochem. Soc. **137**, 2575 (1990).

[15] S. Samukawa and S. Furuoya, Jpn. J. Appl. Phys., Part 2 **32**, L1289 (1993).

[16] C. Suzuki, K. Sasaki, and K. Kadota, J. Vac. Sci. Technol. A **16**, 2222 (1998).

[17] M. Haverlay, W. W. Stoffels, E. Stoffels, G. M. W. Kroesen, and F. J. de Hoog, J. Vac. Sci. Technol. A **14**, 384 (1996).

[18] K. Teii, M. Hori, and T. Goto, J. Appl. Phys. **87**, 7185 (2000).

[19] D. C. Gray, I. Tepermeister, and H. H. Sawin, Proceedings of the 2nd International Conference on Reactive Plasmas, Yokohama, Japan, 1994.

[20] M. Shaepkens, G. S. Oehrlein, and J. M. Cook, J. Vac. Sci. Technol. B **18**, 848 (2000).

[21] X. Xu, S. Rauf, and M. J. Kushner, J. Vac. Sci. Technol. A **18**, 213 (2000).

5. INVESTIGATIONS OF SURFACE REACTIONS IN SI ETCHING BY FLUOROCARBON PLASMAS

5.1. Introduction

In semiconductor plasma etching, the trends of shrinking feature sizes and increasing wafer diameters make etch selectivity a large concern for optimizing processes [1-3]. As silicon is in most cases the under-layer material during fluorocarbon plasma etching of dielectrics, investigations of the kinetics of Si etching by fluorocarbon discharges are important [4-6]. Optimum control of etching processes, given their small critical dimensions and increasing equipment complexity, largely depend on obtaining an understanding of plasma-surface interactions [7-9]. Experimental studies agree that a polymeric C_xF_y layer grows on the wafer surface during fluorocarbon plasma etching of Si, and this polymer regulates the etching process [8, 10-12]. For example, in an investigation of C_2F_6 etching of Si in an ICP reactor, Oehrlein et al. observed nanometer-thick polymer layers on Si and an etch rate that scales inversely with the polymer thickness [8]. Details of the growth kinetics of the polymer, and the mechanism whereby it regulates Si etching, have not been previously addressed quantitatively. The goal of this work is to develop a numerical surface reaction model to correlate plasma conditions, polymer-forming kinetics, and wafer etch chemistry for fluorocarbon plasma etching of Si.

Plasma-surface interactions, in addition to determining wafer processes, can influence plasma properties by consuming or generating plasma species. In low-pressure, high-plasma-density systems, the plasma-surface reactions may be dominant over bulk reactions in determining plasma conditions [13]. Plasma equipment, surface chemistry, and molecular dynamics models have been successful in separately addressing certain aspects of plasma processing [14-16]. There have, however, been few efforts to date which have self-consistently

combined plasma and surface processes into one simulation. With the development of the integrated plasma-surface model described in Chapter 3, we are now capable of investigating Si etching by including the feedback effect of surface reactions (wafer and wall) on the bulk plasma.

In this work, we investigated Si etching by an inductively coupled C_2F_6 discharge using the integrated plasma-surface model described in Chapter 3. Reactions on wafer and wall surfaces are defined separately and are coupled to the bulk plasma. Surface reactions on the grounded wall are dominantly neutral-consuming, as discussed in Chapter 4. The Si wafer is passivated by an overlying polymer layer. Si etch precursors, F atoms, must diffuse through the layer to reach the Si surface and react. Details of the surface reactions will be addressed in Section 5.2. In Section 5.3 our results for Ar/C_2F_6 etching of Si in an ICP reactor will be discussed. The concluding remarks are in Section 5.4.

5.2. Description of the Reaction Mechanisms

During fluorocarbon plasma etching of Si, a polymeric C_xF_y layer is deposited on the wafer surface. The formation of this layer prevents direct contact between the plasma and the wafer surface. Wafer reactions therefore require diffusion of etch precursors through the passivation layer. We included polymer formation and precursor diffusion into our surface reaction mechanism for fluorocarbon plasma etching of Si, and the reaction mechanism is shown schematically in Fig. 5.1. Etching of bare silicon results from the adsorption of fluorine atoms (F) from the plasma onto bare silicon sites (Si_s). The adsorbed fluorine (F_I) then passivates the underlying silicon by chemisorption (=Si-F). Ion bombardment (I^+) provides the activation energy to desorb the etch product (SiF_n). In the presence of a fluorocarbon radical flux (CF_n), a

polymer layer is deposited on the silicon. Fluorine atoms adsorb on the top of the polymer (F_T) and diffuse through the polymer where they adsorb on the bare Si sites at the interface (F_I). The adsorbed fluorine passivates the silicon as in the bare case. Energetic ions incident on the polymer disperse energy through the layer to desorb etch products which diffuse back out the layer. The ions also sputter the polymer layer. Fluorine atoms diffusing through the polymer etch the polymer, forming a volatile product (CF_4) which diffuses out the layer.

Since diffusion fluxes generally decrease with increasing passivation thickness, under conditions when the wafer reactions are limited by reactant fluxes, the passivation can be very influential to etching [8, 10-13]. The SKM represents the deposition of passivation layers in the following manner. CF_x radicals from the plasma are the source material for growth of the passivation layer. The bombardment by energetic ions sputters away the passivation layer. CF_x deposition and ion sputtering are surface processes whose rates do not depend on the passivation thickness for layers larger than one monolayer. Therefore, a steady state passivation layer thickness is difficult, both computationally and experimentally, to obtain under anything other than coincidental conditions. A regulating process is required which depends on the thickness of the layer. In our mechanism, F atoms diffuse through the passivation to the underlying Si. The diffusing F atoms react with the polymer, etching it to form volatile CF_4. Since this is a bulk process and is dependent on the total thickness, a steady state thickness of the passivation layer at each surface site can then be obtained.

The thickness of the passivation (in terms of number of layers *L*) is obtained from

$$\frac{dL}{dt} = \frac{1}{T}\left(\sum_i \Phi_i k_{ij} \boldsymbol{q}_j + \sum_i \Phi_i k_{ip} (1 - \boldsymbol{q}_j) - \sum_i \Phi_i^+ k_{is} LT - [F] L k_E \right) \quad L < 1 \qquad (5.1a)$$

$$\frac{dL}{dt} = \frac{1}{T}\left(\sum_i \Phi_i k_{ip} - \sum_i \Phi_i^+ k_{is} T - [F] L k_E \right) \quad \text{L} > 1 \tag{5.1b}$$

where T is the number of sites in a monolayer, $[F]$ is the density of F atoms in the layer, $\boldsymbol{F}_i$ is the flux of passivating radicals, $\boldsymbol{F}_i^+$ is the flux of incident ions and $\boldsymbol{q}_j$ is the density of surface sites not yet passivated. k_{is} is the sputtering probability, k_{ij} is the sticking coefficient for passivants on the substrate, k_{ip} is the sticking coefficient of passivants on the polymer, and k_E is the etching coefficient of the polymer for F atoms. We enforce that a surface site at a given spatial location cannot have more than a single layer of passivation until all sites have at least one layer. After a single layer of passivation is deposited, passivation grows on top of passivation.

In order for the incident F radicals to react with the Si surface covered by the passivation layer, five steps must take place: (1) F atoms adsorb on the top surface of the passivation layer. (2) The absorbed F atoms diffuse through the polymer layer to reach the polymer-Si interface. (3) The F atoms at the interface adsorb onto the Si surface. (4) The adsorbed F atoms passivate Si sites to form SiF_x. (5) SiF_x is desorbed (either spontaneously or by ion bombardment) and diffuses back through the polymer layer. The intermediate state in which F is at the interface and is then adsorbed onto Si appears somewhat artificial, though necessary to allow for a smooth transition between a clean Si surface and an Si surface fully covered by polymer. Assuming Fick's law for diffusion of F atoms through the passivation layer, the diffusion flux Γ_F reaching the Si surface is

$$\Gamma_F = D \cdot \frac{F_t - F_i}{L}, \tag{5.2}$$

where D is the diffusion coefficient, F_t is the F atom density on the top surface of the passivation layer, F_i is the F atom density at the interface between the polymer and Si, and L is the passivation layer thickness at that surface site.

At the polymer-Si interface, Si surface sites are sequentially passivated by F atoms to form either intermediate -SiF_x sites or a volatile SiF_4 product:

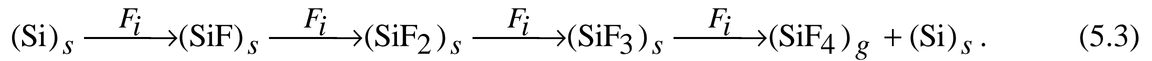

$$(\mathrm{Si})_s \xrightarrow{F_i} (\mathrm{SiF})_s \xrightarrow{F_i} (\mathrm{SiF}_2)_s \xrightarrow{F_i} (\mathrm{SiF}_3)_s \xrightarrow{F_i} (\mathrm{SiF}_4)_g + (\mathrm{Si})_s . \qquad (5.3)$$

Ion bombardment at any step during the sequential passivation process can release an etch product and free up a bare silicon site.

A summary of the surface reaction mechanism is in Table 5.1. For the reasons discussed below, the variety of the species in the model has been constrained. For example, there is only a single polymerizing species, CF_2. This is a simplification. For example, experiments by Capps et al. [17] and Mackie et al. [18] have shown that, depending on reactor conditions and gas mixture, CF_2 can be either consumed or evolved at the surface of a growing polymer film. The latter result implies that the dominant polymer-forming radical in their experiments is a species other than CF_2 and that CF_2 is chemically sputtered from the surface.

5.3. C_2F_6 etching of Si

We applied the SKM model to the investigation of C_2F_6 etching of Si in the ICP reactor shown in Fig. 5.2. The reactor is cylindrical with a radius of 17 cm. The height of the plasma zone is 5.8 cm. Pure C_2F_6 or Ar/C_2F_6 is supplied from the shower head, ICP power at 13.56 MHz is applied using a four-turn coil, and a 13.56-MHz bias is applied to the substrate. The gas

pressure is 10 mTorr, the ICP power is 650 W and the total gas flow rate is 200 sccm. These parameters produce moderate (about 50%) dissociation on a reactor-averaged basis using pure C_2F_6. No attempt was made to make the flux of reactants to the 20-cm-diameter wafer uniform. The gas phase reaction chemistry is shown in the Appendix. Although the gas phase chemistry has, in reality, a larger variety of neutral and charged species (such as CF^+) we have purposely chosen to use a more simplified gas phase mechanism. The intent is to minimize the variety of species incident on the substrate in order to isolate specific processes to investigate their importance. A more complex gas-phase reaction mechanism can be implemented as necessary. We will refer to polymer thickness in terms of number of layers, as opposed to actual thickness, due to the uncertainty of the chemical structure of the film. For example, polytetrafluoroethylene, a $[C_2F_4]_n$ polymer, has mass density of 0.58 g/cm^3, which corresponds to approximately 6.6 A/layer, or 1.5 layers/nm.

Typical plasma properties are shown in Fig. 5.2 where the densities of CF_2 (deposition precursor), CF_3^+ (the major ion) and the etch product SIF_4 are plotted for the base case. The rf bias is 100 V and the time-averaged sheath potential is 95 V. The peak CF_2 density of $\approx 8 \times 10^{12}$ cm^{-3} occurs at the center of the reactor. Due to the power deposition peaking under the center of the coils, the CF_3^+ density has an off axis peak of $\approx 3 \times 10^{11}$ cm^{-3}. The density of the etch product is $\approx 3 \times 10^{12}$ cm^{-3} above the wafer and decreases as it diffuses into the plasma and is pumped away. The density of F atoms has only a $\pm 10\%$ variation over the wafer with a peak value of 1.7×10^{13} cm^{-3}.

The fluxes of CF_2, CF_3^+, and F to the substrate are shown in Fig. 5.3(a). The reactive sticking coefficients of CF_2 and CF_3^+ on the walls of the reactor are, for this case 0.8 and 1.0, respectively. The CF_3^+ flux has a small off-axis peak due to its off axis source. With an ion flux

of ≈1.2 × 10^{16} cm^{-2}-s^{-1}, the power onto the wafer is about 180 mW-cm^{-2}. Since F atoms have a smaller reactive sticking coefficient (0.005) on the walls, their density is more uniform and produces a more uniform flux to the substrate. The predicted polymer thickness and etch rate for this case are shown in Fig. 5.3(b). As a consequence of the polymer-forming CF_2 peaking on the axis, the polymer thickness on the wafer also peaks on axis. For these conditions, F atom etching of the polymer dominates and, since the F atom flux is uniform, the radial dependence of the polymer thickness is dominantly determined by the CF_2 flux. As the etch rate is flux limited by the diffusion of F atoms through the polymer layer, the etch rate is lowest on the axis where the polymer thickness is greatest.

The total rate of deposition of CF_2 radicals on the reactor walls can be higher than that on the wafer since the area of the walls is typically larger. Therefore, as reactor wall conditions change, the CF_2 loss to the walls may have a larger influence on the plasma properties than the disposition of CF_2 on the wafer. For example, Schaepkens et al. [13] investigated the consequences of reactor wall temperature on the thickness of passivation layers, etch properties, and plasma properties in an ICP reactor operating in CHF_3 and C_3F_6. When the reactor wall temperature was changed from room temperature to ≈240 °C, they found a 40% increase in density for the CF_2 radical and a 10% decrease in density for the *F* atom radical based on plasma emission, as shown in Fig. 5.4(a). The subsequent variation of the plasma properties modified the passivation thickness and ultimately the etch rate. Higher wall temperature produced more CF_2 in the plasma, thicker passivation, and lower etch rates.

We simulated the change of reactor wall temperature by varying the CF_2 sticking probability (S_{CF2}) on the chamber walls with the hypothesis that high wall temperature corresponds to low $S_{CF2.}$ The chord averaged densities of CF_2 and F radicals at mid-reactor (as

would be observed by optical emission) are shown in Fig. 5.4(b). The increase of CF_2 density with increasing wall temperature directly results from the decreasing CF_2 sticking loss at the wall. The resulting gas chemistry then favors consumption of F atom, so F atom density decreases. Simulation also obtained a ~10% decrease in F atom density with a ~40% increase in CF_2 density, agreeing with experiments. By assuming that (1- S_{CF2}) scales as $T(wall)^{1/2}$, both experimental and simulated results of the normalized CF_2 densities as a function of S_{CF2} (or $T(wall)^{1/2}$) are shown in Fig. 5.5. The two lines fit well. The steady state passivation layer thickness and the etch rate as a function of radius on the wafer are shown in Fig. 5.6(a) and 5.6(b) for S_{CF2} = 0.1 - 0.8. The corresponding CF_2 fluxes, polymer thickness and etch rate at the center of the wafer are shown in Fig. 5.6(c). As the CF_2 sticking coefficient on the walls decreases, there is a corresponding increase in density of CF_2 and of its flux to the substrate. Lower sticking coefficients offer slightly more uniform fluxes. The polymer thickness also increases with decreasing S_{CF2} in proportion to the increase in CF_2 flux, becoming somewhat more uniform at low sticking coefficient, in agreement with Schaepkens et al. [13]. The rate of arrival of *F* atoms at the polymer-Si interface is inversely proportional to the passivation layer thickness. An increase of passivation layer thickness thus leads to a lower interface *F* atom density, and a decrease of the Si etch rate. The resulting etch rates vary inversely with the wall sticking coefficient and polymer thickness, becoming more uniform at lower wall sticking coefficients, in agreement with Schaepkens et al.

In high plasma density reactors, such as ICPs, rf substrate biases within several hundred volts typically do not contribute significantly to plasma generation. The bias does, however, determine the sheath potential, and so influences the etch process through the incident ion energy. To first order, the magnitudes of all reactive fluxes are insensitive to the magnitude of

the bias. Changing the bias only changes the energy of the ions striking the substrate, which, for this reaction mechanism, only affects the sputtering rate of the polymer and the rate of ion activated desorption of etch products. We varied the rf substrate bias from 50 to 150 V to vary the time-averaged sheath potential and show the resulting polymer thickness and etch rate as a function of time-averaged sheath potential in Fig. 5.7. Only the rate of polymer sputtering was allowed to change. As the bias and sheath potential increase, the ion energy incident on the passivation layer increases, thereby increasing the polymer erosion rate. The end result is a thinner polymer thickness and a higher etch rate.

Many of the transport coefficients and reaction rate coefficients used in our surface reaction mechanism are estimated or derived from parametric studies. Typically, in the absence of comprehensive fundamental measurements of these coefficients or coefficients derived from molecular dynamics simulations, the coefficients are derived by parameterizing the model and comparing predicted etch rates and polymer thicknesses to well characterized experiments. This methodology has been successfully used in deriving surface reaction rate coefficients for surface profile models by Vahedi et al. [19].

Given the method of selecting coefficients for the model, it is valuable to investigate the sensitivity of the model to variations in those coefficients. For example, the probability of polymer sputtering by ions is given by Eq. 3.11. In the results thus far, we chose $p_o = 0.1$ and $E_r = 150$ eV. The etch rate and polymer thickness as a function of p_o are shown in Fig. 5.8(a). As p_o decreases, the polymer thickness increases and the etch rate decreases. At $p_o = 0$, the polymer thickness is 8.2 layers. There is not unlimited polymer growth, and there is still a net etch rate, since the polymer continues to be etched by F atoms. The sensitivity of the silicon etch rate and polymer thickness to the rate of polymer etching by F atoms is shown in Fig. 5.8(b). The base

case value is 0.5 s^{-1}. Without polymer etching by F atoms, the polymer is 16.6 layers thick. As the polymer etch rate increases, the polymer thickness decreases and the etch rate increases, though not at the rate one might expect based solely on the decrease in polymer thickness. This trend results from the fact that F atoms which would otherwise be available to diffuse through the polymer layer are being depleted by their etching of the polymer. The sensitivity of silicon etch rate and polymer thickness to the rate of diffusion of F atoms through the polymer is shown in Fig. 5.8(c). (The base case has speed 25 layers/s.) Increasing rates of diffusion result in higher etch rates. There is an initial linear rate of increase in the etch rate with diffusion speed until all of the silicon surface sites are saturated. At that time the etch rate is limited by desorption of etch product. The polymer thickness experiences a small increase as the F atom diffusion speed increases. This results from the shorter time during which F atoms reside in and are likely to etch the polymer.

The predicted etch rate is also sensitive to the details of the etch model embodied, in part, in the identity of the etch products. In the absence of physical sputtering, Si sites are passivated by F atoms, forming chemisorbed $=SiF_n$. For $n \leq 3$, some amount of ion activation is likely required to remove the SiF_n etch product from the surface. If we assign a sufficiently high probability for ion desorption so that etching is not severely constrained by the desorption step, there is not an acute sensitivity of etch rate on the etch product. For example, assigning a unity ion activated desorption probability for the $-SiF_3 \rightarrow SiF_4$ passivation step, as in the base case, the etch rate is 596 A/min. Adding a 0.5 ion activated desorption probability for $-SiF_3$ raises the etch rate to 667 A/min. Adding an additional 0.25 ion activated desorption probability for $=SiF_2$ increases the etch rate to 739 A/min. The weak dependence of etch rate on the details of the etch product is, for these conditions, a consequence of the fact that the F atom flux and F atom

diffusion rates through the polymer are sufficiently high that passivation of the surface is not rate limited by the availability of fluorine.

Where the etch rate may, in fact, be sensitive to the identity of the etch product is in the ion activated desorption step. There is a complex, and not well understood, mechanism for transfer of ion energy through the polymer to activate the desorption. The mechanism could be kinematic, thermal, or a combination of the two. To investigate the sensitivity of etch rate on ion activated desorption, the probability for ion desorption was varied between 0.05 and 1.0. The resulting etch rates as a function of position are shown in Fig. 5.9(a) for the base case. The etch rate at r = 0 and the Si_s surface coverage (Si sites which are not passivated) are shown in Fig. 5.9(b). Recall that the polymer thickness is largest at r = 0 and decreases to larger radii as shown in Fig. 5.3. For high probabilities of ion activated desorption, the etch rate is not limited by the desorption step but rather by the rate of diffusion of F atoms through the polymer. The etch rate is therefore smallest on axis. The Si_s surface coverage is large, 0.2 for unity ion activation, indicating that as Si sites are passivated by F atoms, they are rapidly etched, leaving a reasonably large fraction of sites available for repassivation. As the ion activated desorption probability decreases, the etch rate becomes progressively more limited by the rate of desorption, as opposed to the rate of passivation. The etch rate transitions from being largest at large radii, where the polymer is thinnest, to being largest at small radii, where the ion flux is largest. There is a commensurate decrease in the etch rate. The degree to which the etch rate is limited by ion activated desorption is indicated by the Si_s surface coverage. At low values of the ion activated desorption, for example 0.1, the Si_s surface coverage is less than 0.03, indicating that nearly all sites are passivated and “waiting” for ion activated desorption.

The Si etch rate is ultimately a first-order function of three fluxes: the ion flux, the

polymerizing precursor (in this case, CF_2) and the F atom flux. For otherwise constant conditions, the etch rate correlates inversely with the thickness of the polymer layer, and all three fluxes contribute to determining the thickness of the polymer layer. The F atom and ion flux decrease its thickness through etching and sputtering, while the CF_2 flux adds to its thickness. The ion flux also desorbs the etch product. Unless there is severe depletion of the feedstock C_2F_6, it is difficult to significantly change the ratios of these fluxes since varying power or pressure changes all fluxes in approximately the same proportion.

One can, however, change the relative proportions of these fluxes by varying the gas mixture. For example, while keeping pressure, power deposition and total flow rate constant (10 mTorr, 650 W, 200 sccm), the gas mixture was varied from Ar/C_2F_6 = 0/100 to 95/5. The resulting fluxes, etch rates, and polymer thickness are shown in Fig. 5.10. By diluting the C_2F_6 with argon, the fluxes of F and CF_2 to the substrate generally decrease, though at a slower rate than the decrease in the C_2F_6 mole fraction. This results from the plasma density and electron temperature increasing with decreasing C_2F_6 mole fraction. The lower flow rate of C_2F_6 is compensated by the higher electron density, thereby producing commensurate dissociation rates of C_2F_6. In fact, the CF_2 flux actually peaks at an intermediate mole fraction of C_2F_6 for this reason.

Due to the increase in the ion flux (which erodes the polymer layer) and overall decrease in the CF_2 flux (which builds the polymer layer), the ratio of the (ion flux)/(CF_2 flux) increases with increasing Ar dilution. The polymer thickness therefore decreases with increasing Ar dilution. When the etch rate is constrained by diffusion of F atoms through the polymer, the etch rate increases with decreasing polymer thickness, provided that the F atom flux is above a critically high value which saturates the Si surface sites. As the F atom flux decreases below this

value, the etch rate decreases in spite of a decrease in the polymer thickness. For these conditions, the maximum etch rate occurs at Ar/C_2F_6 = 0.8/0.2, where the polymer layer is thin but the F atom flux has not decreased below its critical value. Although the etch rate maximizes at this low C_2F_6 mole fraction, desirable etch characteristics such as selectivity and low lateral etch rates, which largely depend on polymer layers, will degrade with increasing Ar dilution.

5.4. Concluding Remarks

Ar/C_2F_6 etching of Si in a high-plasma-density ICP reactor was investigated by the integrated plasma-surface model described in Chapter 3. Results demonstrated that with a decreasing CF_2 sticking coefficient on the reactor wall, the bulk CF_2 density increases, which leads to a thicker polymer layer on the wafer and a lower Si etch rate. Higher biases produce larger sputtering rates and thinner passivation. A sensitivity analysis was performed on rate coefficients employed in the model. Both the magnitude and radial dependence of the etch rate depend on the rate of ion activated desorption of etch products. For conditions where ion-desorption is not rate limiting, etch rates generally vary inversely with polymer thickness. For conditions where the ion-desorption is rate limiting, the etch rate and its spatial dependence vary with ion flux.

Table 5.1. Surface Reaction Mechanism

Species Definitions:

X_g	Gas phase species
P_S	Surface site on top of polymer layer
F_T	F adsorbed on top of polymer layer
F_I	F adsorbed on Si or at the interface of Si and polymer
F_A	Site on Si surface available for adsorption
W_S	Reactor wall site
R_S	Surface site available for polymer growth
P	Polymer layer
SiF_{xs}	Si site on surface passivated by x F atoms
α	Fraction of Si sites overlayed by polymer
T	Surface density of sites

Reaction[a, b, d]	Probability	Note
$F_g + P_S \rightarrow F_T$	0.3α	
$F_g + P_S \rightarrow P_S + F_{2g}$	0.005α	
$F_g + P \rightarrow P + F_{2g}$	$0.005\ (1-P_S)$	
$CF_{2g} + R_S \rightarrow P + R_S$	0.3	
$CF_{3g} + P \rightarrow C_2F_{6g} + P$	0.005 min(P,1)	
$CF_3{}^+{}_g + P \rightarrow CF_{2g} + CF_3$	p_o=0.1, E_t=150 eV	c, f
$Ar^+{}_g + P \rightarrow CF_{2g} + Ar$	p_o=0.1, E_t=150 eV	c, f
$F_T + P \rightarrow CF_{4g} + P_S$	0.5T	c
$F_T + F_A \rightarrow F_I + P_S$	$25T(F_T - F_A)F_A/\max(P,0.1)$	e
$F_g + F_A \rightarrow F_I$	$0.05(1-\alpha)$	
$F_g + F_A \rightarrow F_A + F_2$	$0.005(1-\alpha)$	
$F_I + SiF_{XS} \rightarrow SiF_{(X+1)S} + F_A$	25T	
$CF_3{}^+ + SiF_{XS} \rightarrow SiF_X + CF_{3g} + F_A$	1.0	e
$Ar^+ + SiF_{XS} \rightarrow SiF_X + Ar_g + F_A$	1.0	e
$F_g + SiF_{XS} \rightarrow F_{2g} + SiF_{XS}$	$0.005(1-\alpha)$	
$F_g + W_S \rightarrow F_{2g} + W_S$	0.005	
$CF_{2g} + W_S \rightarrow W_S$	0.8	e
$CF_{3g} + W_S \rightarrow C_2F_{6g} + W_S$	0.005	

Table 5.1. Continued

Notes:

a. Unless otherwise specified, all ions neutralize on all surfaces, returning as their neutral counterparts.
b. Processes not listed (e.g., CF_{4g} + W_S →Products) are nonreactive. Incident species reflect with unity probability.
c. The sum of probabilities of gas phase species with surface sites shown here may not sum to unity. The remaining probability is assigned to the incident species reflecting without reaction.
d. All gas phase species have units of flux ($cm^{-2}s^{-1}$). All surface species have units of fractional coverage. P has units of layers. Derivatives for surface species are divided by the surface site density, T. In this work, T = 1 x 10^{15} cm^{-2}.
e. Base case value. See text for sensitivity analysis.
f. See Eq. 3.11.

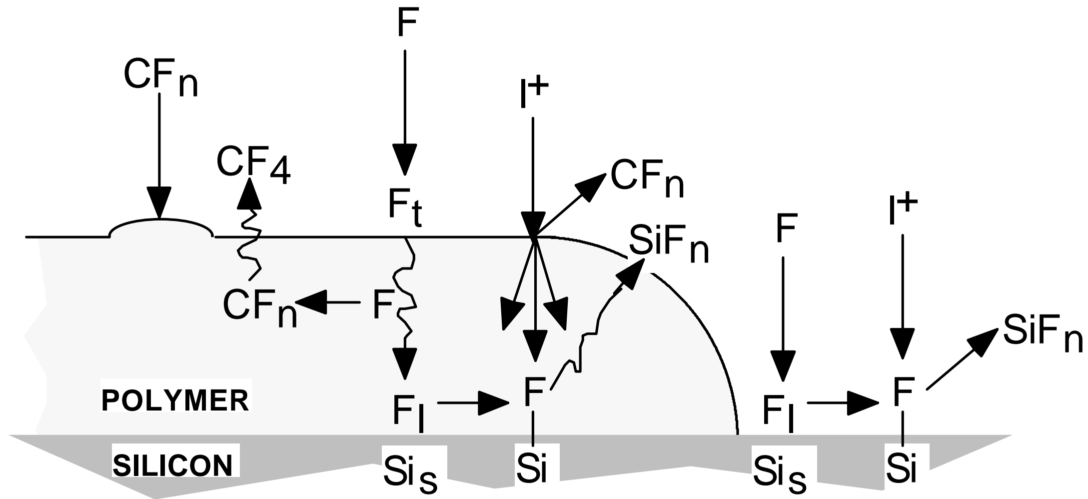

Fig. 5.1. Schematic of the surface reaction mechanism for Si etching by fluorocarbon lasma.

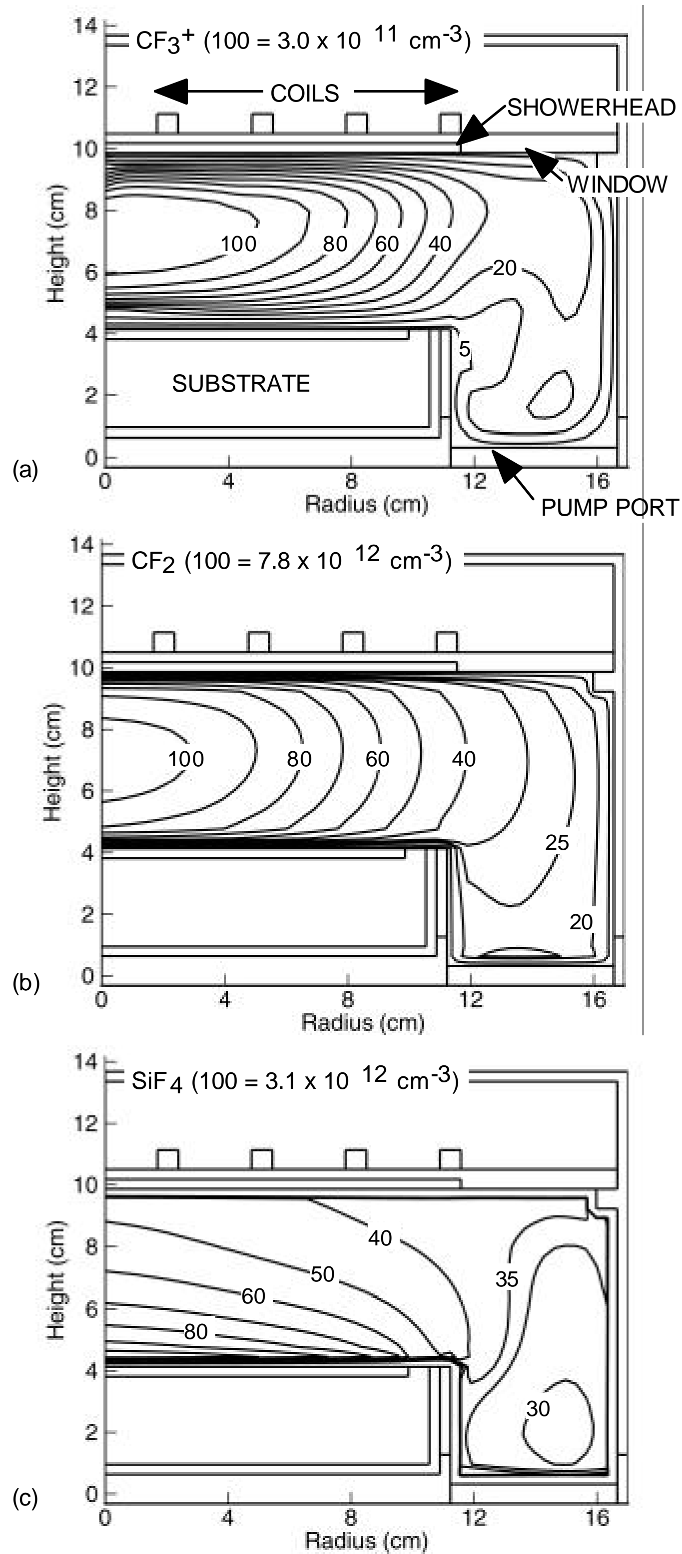

Fig. 5.2. Densities of (a) CF_3^+, (b) CF_2, and (c) SiF_4 in the ICP reactor for the base case conditions (10 mTorr, 650 W, 200 sccm, 100 V bias). The contours are labeled with the percentage of the maximum value shown at the top of each figure.

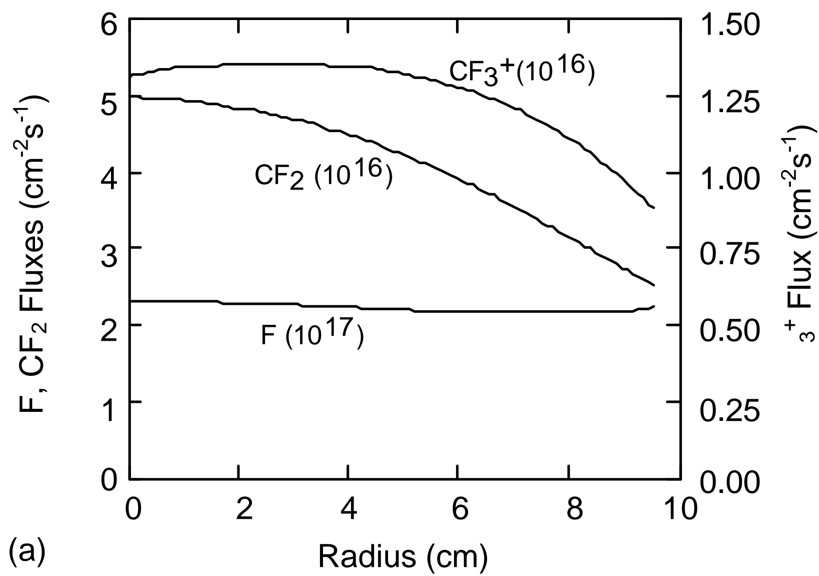

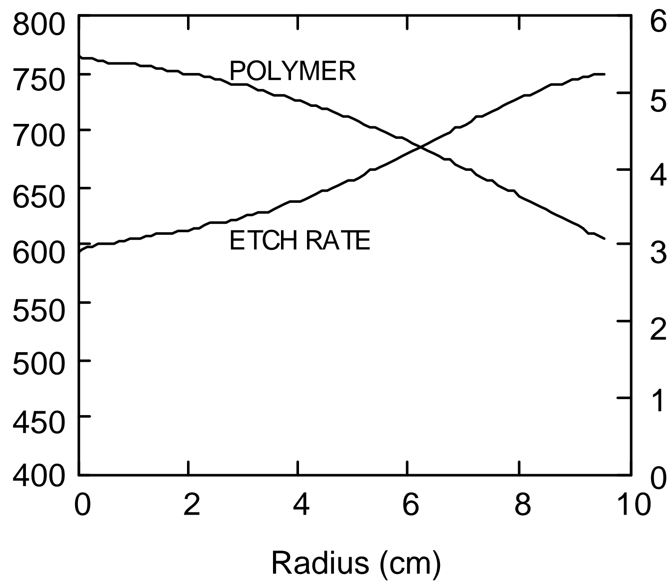

Fig. 5.3. Plasma and surface properties for the base case as a function of radius. (a) Fluxes of CF_3^+, CF_2 and F to the wafer. (b) Polymer layers and etch rates. The etch rate is constrained by the diffusion of F atoms through the polymer layer, giving rise to a minimum at the center of the wafer where the polymer layer is thickest.

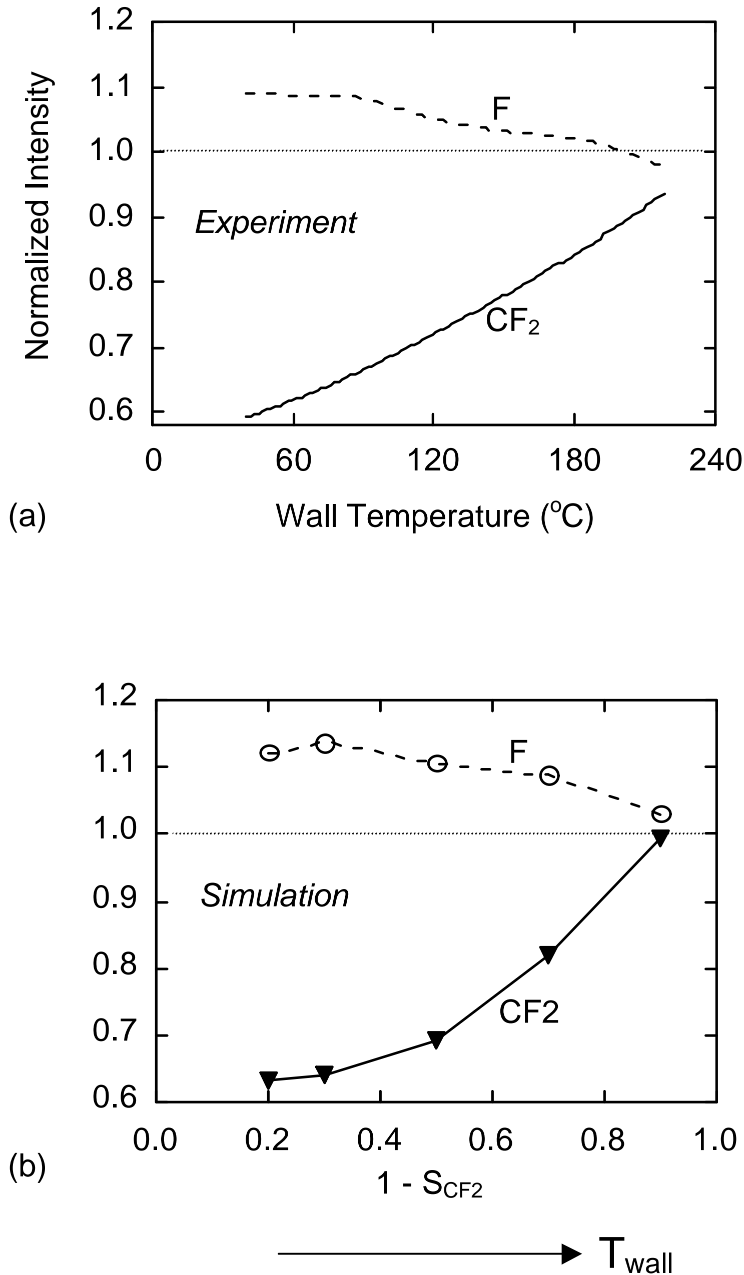

Fig. 5.4. Influences of reactor wall condition on plasma properties. (a) Experimental data of normalized CF_2 and F densities as a function of the reactor wall temperature [13]. (b) Simulated results of normalized CF_2 and F densities as a function of (1 - S_{CF2}), where S_{CF2} is the sticking coefficient of CF_2 on the wall and it decreases with increasing reactor wall temperature.

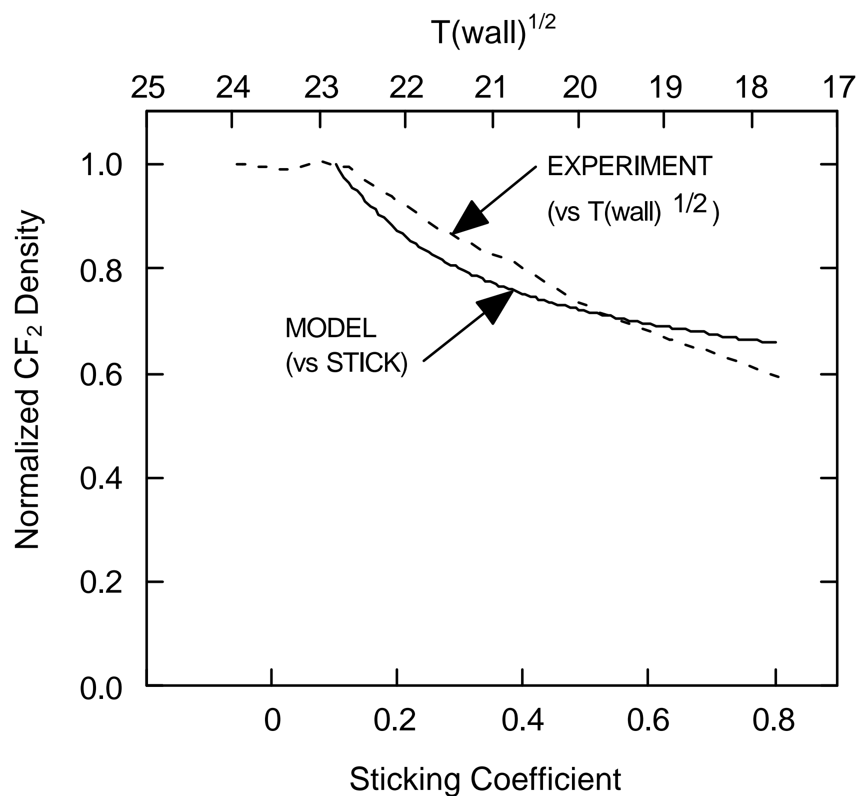

Fig. 5.5. Simulated CF_2 normalized density as a function of sticking coefficient of CF_2 radicals on the reactor walls. Experimental results of Shaepkens et al. [13] are shown plotted as a function of $T(wall)^{1/2}$. A decreasing sticking coefficient for CF_2 increases its gas phase density.

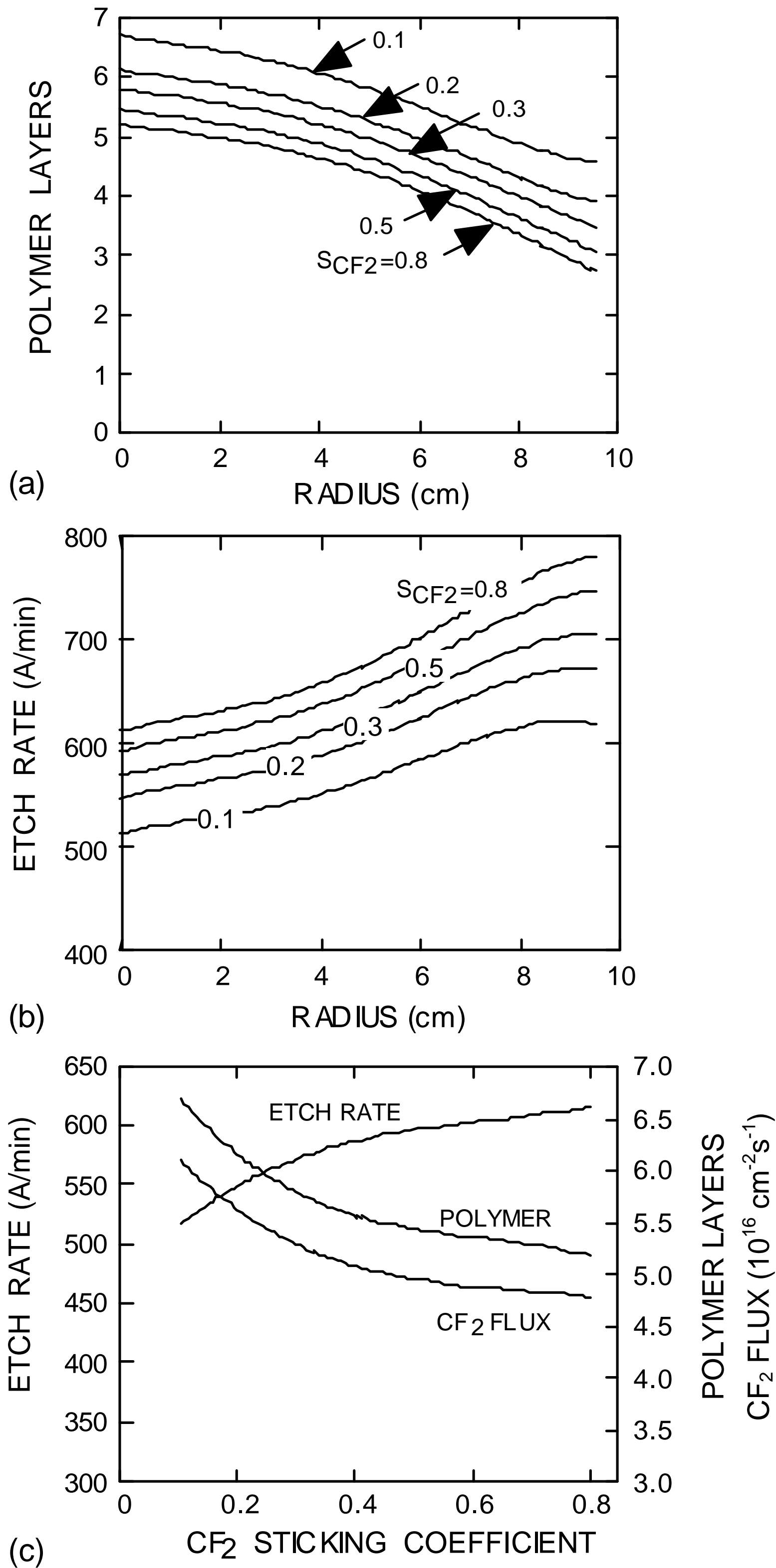

Fig. 5.6. Surface properties as a function of CF_2 sticking coefficient (S_{CF2}) on the walls of the reactor. (a) Polymer layers as a function of radius for different sticking coefficients. (b) Etch rates for different sticking coefficients. (c) Polymer layers, CF_2 flux, and etch rate at the center of the wafer as a function of S_{CF2}.

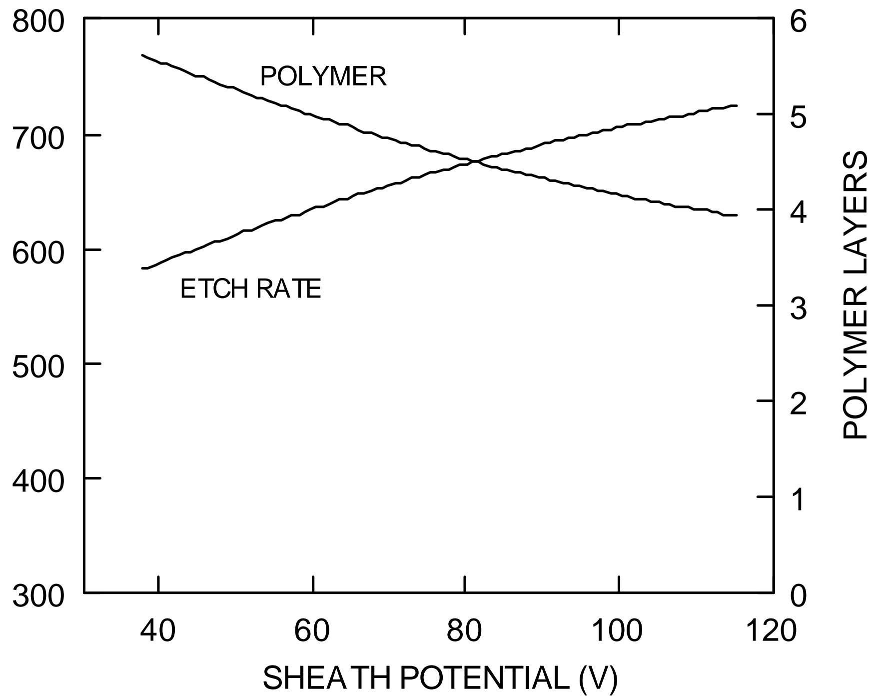

Fig. 5.7. Polymer thickness and etch rate at the center of the wafer as a function of sheath potential. Increased sputtering of the polymer layer with increasing bias decreases its thickness and increases the etch rate.

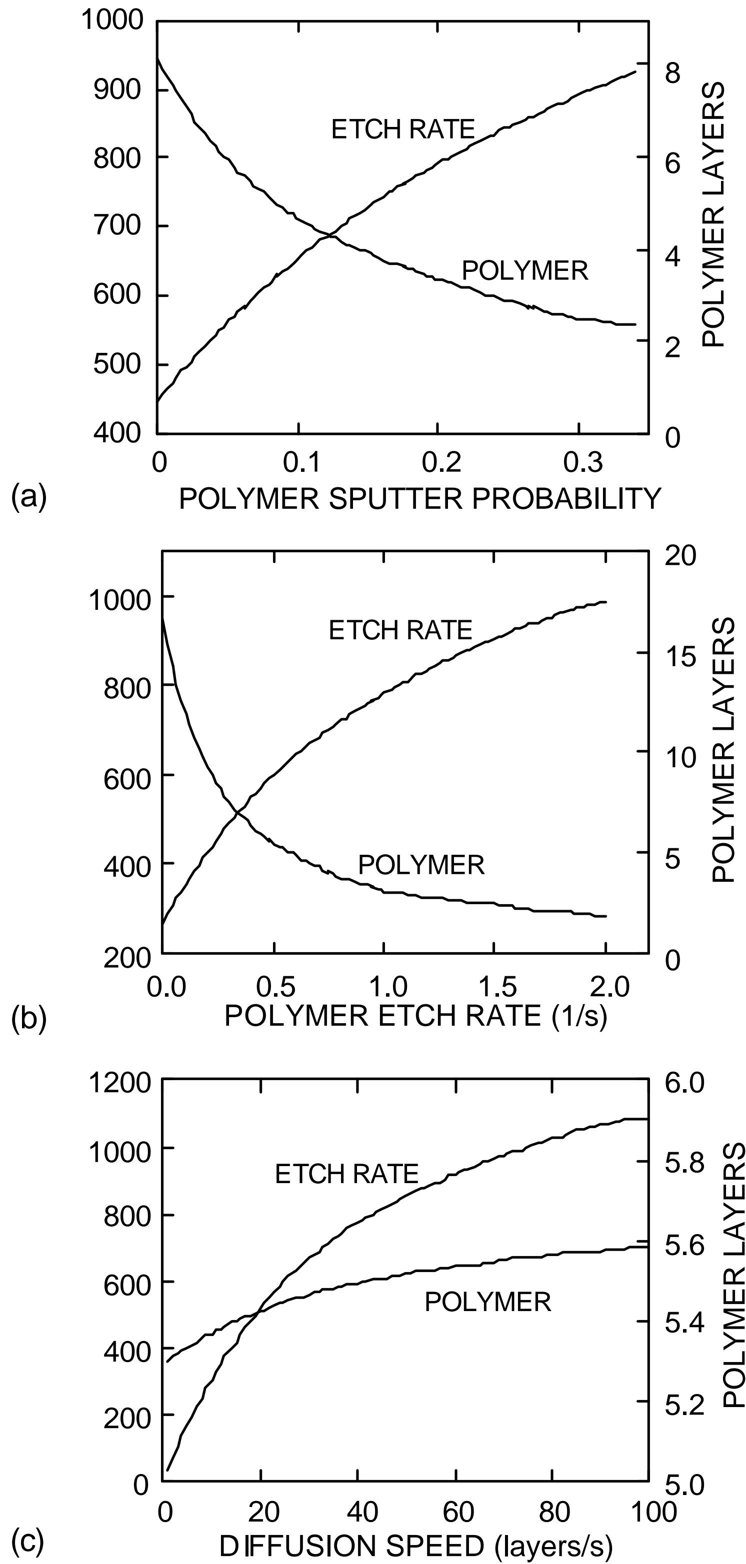

Fig. 5.8. Results from a sensitivity study of etch rates and polymer thickness while varying rate coefficients in the surface reaction mechanism. (a) Polymer sputter probability (base case has $p_o = 0.1$). (b) Polymer etch rate by F atoms (base case has $k = 0.5\ s^{-1}$). (c) F atom diffusion rate (base case = 25 layers/s).

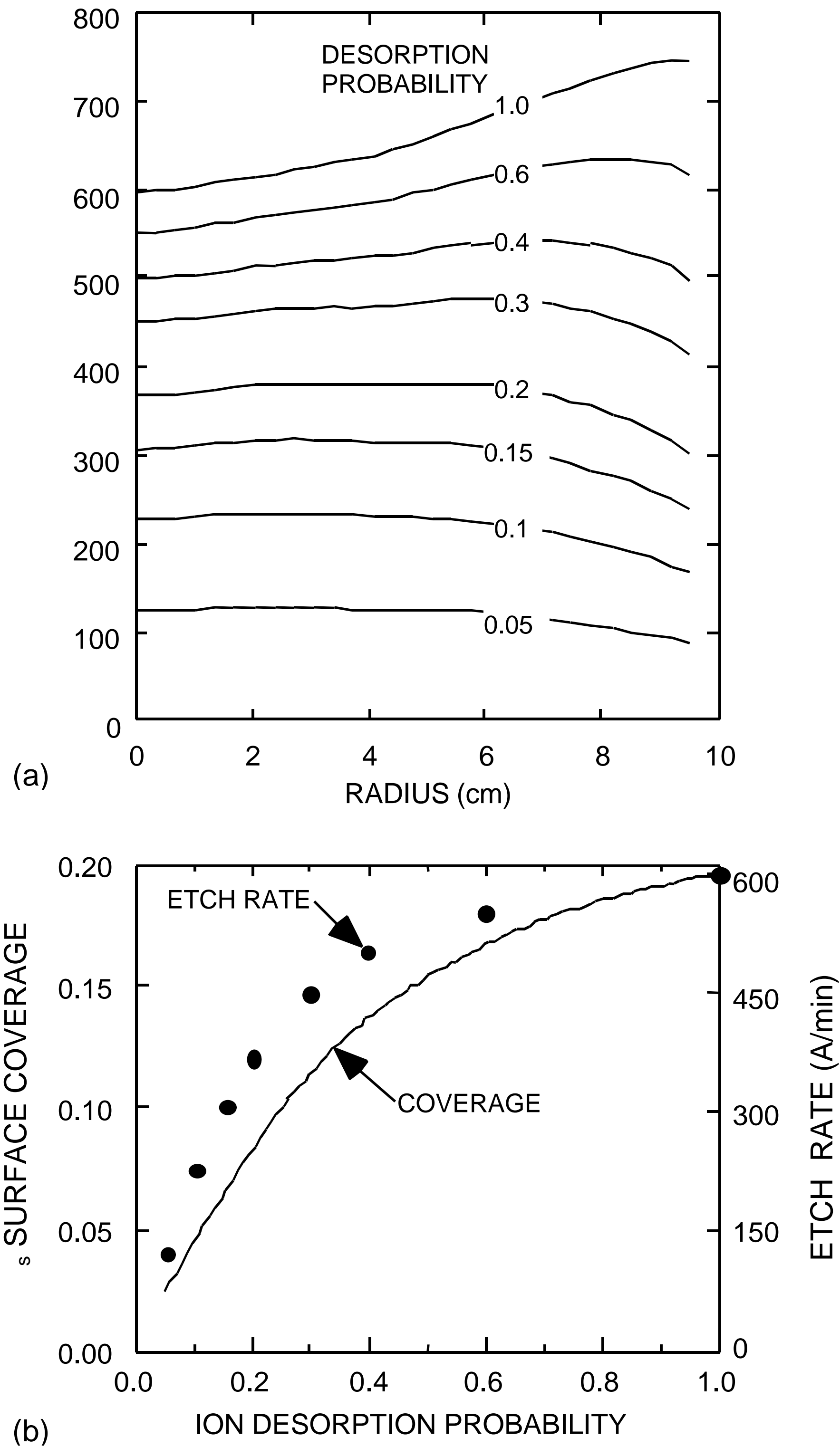

Fig. 5.9. Surface properties as a function of the ion desorption probability of the etch products. (a) Etch rate as a function of radius for different desorption probabilities. (b) Etch rate and coverage of Si_s at the center of the wafer as a function of ion desorption probability. At high desorption probability, the etch rate is limited by the diffusion of F atoms through the polymer. At low ion desorption probability, the etch rate is limited by

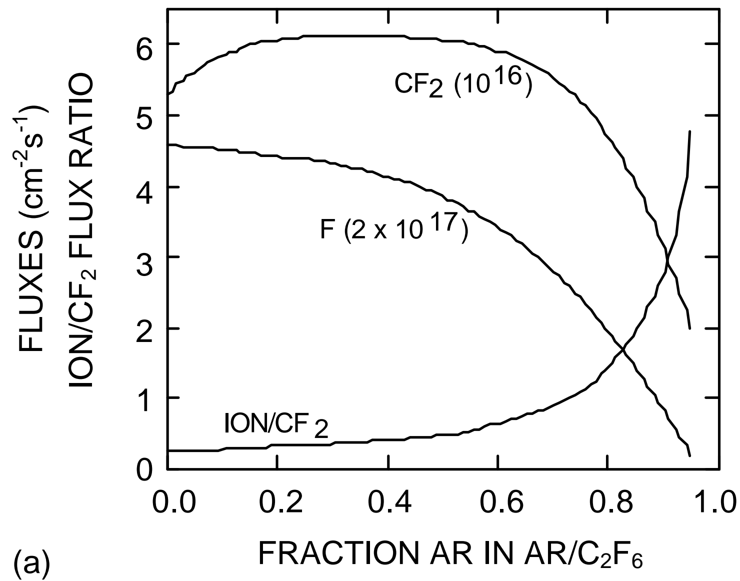

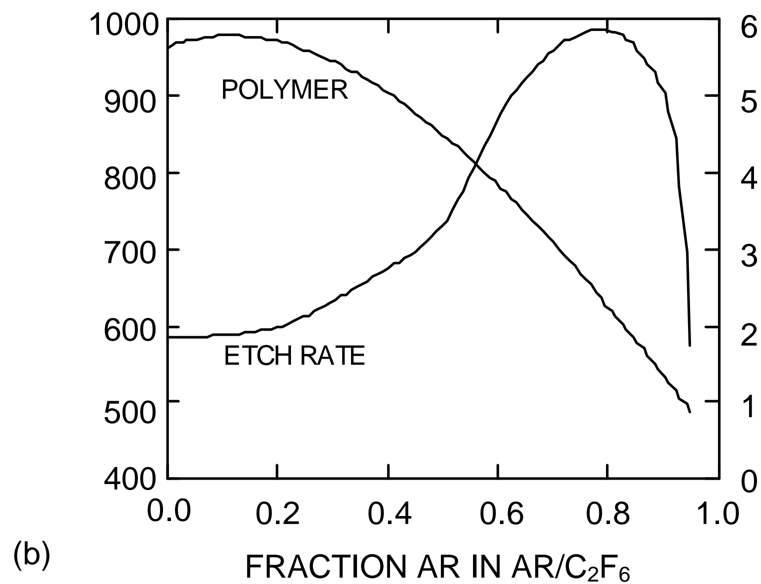

Fig. 5.10. Plasma and surface properties as a function of dilution with argon in an Ar/C_2F_6 gas mixture. (a) Fluxes of CF_2, F atoms and the ratio of the ion flux to the CF_2 flux. (b) Etch rate and polymer thickness. The etch rate increases with decreasing polymer thickness until the F atom flux is insufficient to fully passivate silicon sites.

5.5. References

[1] Y. Wang and Leroy Luo, J. Vac. Sci. Technol. A **16**, 1582 (1998).

[2] N. R. Rueger, M. F. Doemling, M. Shaepkens, J. J. Beulens, T. E. F. M. Standaert, and G. S. Oehrlein, J. Vac. Sci. Technol. A **17**, 2492 (1999).

[3] V. Ku and D. Parks, J. Vac. Sci. Technol. B **17**, 2306 (1999).

[4] C. F. Abrams and D. B. Graves, J. Appl. Phys. **86**, 5938 (1999).

[5] B. O. Cho and S. W. Hwang, J. Electrochem. Soc. **146**, 350 (1999).

[6] G. S. Oehrlein, Y. Zhang, D. Vender, and O. Joubert, J. Vac. Sci. Technol. A **12**, 333 (1994).

[7] G. M. W. Kroesen, H. J. Lee, H. Moriguchi, H. Motomura, T. Shirafuji, and K. Tachibana, J. Vac. Sci. Technol. A **16**, 225 (1998).

[8] T. E. F. M. Standaert, M. Shaepkens, N. R. Rueger, P. G. M. Sebel, G. S. Oehrlein, and J. M. Cook, J. Vac. Sci. Technol. A **16**, 239 (1998).

[9] S. Hiroyuki, K. Akisiro, O. Naomichi, S. Shoso, and T. Takayuki, Jpn. J. Appl. Phys., Part 1 **36**, 2477 (1997).

[10] A. J. Bariya, C. W. Frank, and J. P. McVittie, J. Electrochem. Soc. **137**, 2575 (1990).

[11] B. E. E. Kastenmeiter, P. J. Matsuo, G. S. Oehrlein, and J. G. Langan, J. Vac. Sci. Technol. A **16**, 2047 (1998).

[12] S. Samukawa and S. Furuoya, Jpn. J. Appl. Phys., Part 2 **32**, L1289 (1993).

[13] M. Schaepkens, R. C. M. Bosch, T. E. F. M. Standaert, and G. S. Oehrlein, J. Vac. Sci. Technol. A **16**, 2099 (1998).

[14] W. Z. Collison, T. Q. Ni, and M. S. Barnes, J. Vac. Sci. Technol. A **16**, 100 (1998).

[15] E. Meeks, R. S. larson, S. R. Vosen, and J. W. Shon, J. Electronchem. Soc. **144**, 357

(1997).

[16] B. A. Helmer and D. B. Graves, J. Vac. Sci. Technol. A **16**, 3502 (1998).

[17] N. E. Capps, N. M. Mackie, and E. R. Fisher, J. Appl. Phys. **84**, 4736 (1998).

[18] N. M. Mackie, V. A. Venturo, and E. R. Fisher, J. Phys. Chem. B **101**, 9425 (1997).

[19] V. Vahedi, D. J. Cooperberg, J. M. Cook, L. Marquez, E. Hudson, and J. Winniczek, 45th International Symposium of the American Vacuum Society, Baltimore, MD, November 1998, page PS2-TuM9.

6. INVESTIGATIONS OF THE SURFACE REACTIONS IN C_2F_6 PLASMA ETCHING OF SiO_2 WITH EQUIPMENT AND FEATURE SCALE MODELS

6.1. Introduction

Dry plasma etching of SiO_2 is widely employed in the fabrication of multilayer ultra-large-scale integrated circuits. Fluorocarbon plasmas are most frequently used for this purpose. It is well known that during fluorocarbon plasma processing, a CF_x polymer layer is deposited on the surface, thereby regulating wafer etching [1-5]. The CF_x polymer is deposited from C_xF_y neutrals having sufficient dangling bonds and is consumed by F atom etching and energetic ion sputtering [6-8]. Since the major effects of the polymer are to limit species diffusion through the layer and to dissipate ion bombarding energy, the etch rate generally scales inversely with the polymer thickness [9-10]. For example, in an investigation of SiO_2 etching in an inductively coupled discharge sustained in C_2F_6, Oehrlein et al. observed an increasing etch rate with increasing substrate bias, which was attributed in part to the decreasing polymer thickness [9]. Similar dependencies of etch rate, polymer thickness, and substrate bias were also observed in CHF_3 plasma etching of SiO_2 [10]. Although fluorocarbon plasma etching of SiO_2 has been experimentally investigated, there are few theoretical descriptions which address the details of the polymerization kinetics and their relation to plasma conditions and etch properties.

In this work, a surface reaction mechanism for C_2F_6 plasma etching of SiO_2 is discussed. The model determines the polymer thickness by accounting for polymer formation and consumption in a plasma environment. SiO_2 etching results from a series of events including neutral passivation, ion assisted dissorption, and fluorination or ion chemical sputtering. The rates of plasma-surface reactions depend on the overlaying polymer thickness. The mechanism was first applied to the simulation of blanket etching in the integrated plasma equipment -

surface kinetics model described in Chapter 3 [11]. We found that the ion-energy-dependent sputtering yield of the polymer strongly regulates the processes due to their dependencies on the polymer thickness and the delivery of activation energy through the polymer. Ion energy is in turn controlled by the substrate bias. Low-energy ion activation of surface sites can assist polymer formation and therefore suppress wafer etching. The etch selectivity of SiO_2 over Si is due to the preferential polymer etching by the oxygen in SiO_2, which leads to thinner passivation on SiO_2 than on Si under the same process conditions. Good agreement for etch rates and selectivity between model and experimental results was achieved. The reaction mechanism was also implemented into the Monte Carlo Feature Profile Model (MCFPM) [13-14] to simulate the evolution of microtrenches during the etch process. Similar dependencies of the etch rate on the substrate bias were obtained from the topographic simulation. Tapered profiles were obtained under process conditions yielding strong sidewall passivation. Higher energies lead to less tapered profiles due to increasing polymer sputtering. The tapering effect also depends on the ratio of passivating neutral to ion fluxes and so can be regulated by judicious choice of gas mixture, such as argon dilution. Transitions of profiles from tapered to straight to bowed outlines with decreasing passivating neutral-to-ion flux ratio were observed. The surface reaction mechanism for SiO_2 etching by a C_2F_6 plasma is discussed in Section 6.2. Results from the equipment and the feature scale simulations are presented in Sections 6.3 and 6.4, respectively. Our concluding remarks are in Section 6.5.

6.2. Surface Reaction Mechanisms in C_2F_6 Plasma Etching of SiO_2

The SiO_2 reaction mechanism is schematically shown in Fig. 6.1. The major steps in the mechanism are as follows. In summary, a polymer is grown on the SiO_2 surface by C_xF_y

deposition. Low-energy ion bombardment activates polymer surface sites for faster neutral sticking. Ion sputtering, F atom etching, and ion assisted polymer-wafer interaction consume the polymer, and the steady state thickness of the polymer is reached as the balance of its deposition and consumption. The polymer-wafer interaction consumes the SiO_2 wafer as well as the polymer. $CF_{x\leq 2}$ chemisorption on SiO_2 sites produces SiF_xCO_2 surface complexes which dissociate to SiF_x sites upon ion bombardment or F atom interaction. The SiF_x species are then removed by either ion chemical sputtering or F atom etching. Because the polymer passivation layer limits mass diffusion and dissipates energy, the rates of reactions involving energy transfer or species diffusion through the polymer are polymer thickness dependent. The surface reactions encompassing this mechanism are listed in Table 6.1. To investigate the etch selectivity of SiO_2 over Si, surface reactions valid for Si etching are also specified in Table 6.1. The reaction probabilities in Table 6.1 are values for the base case study which will be discussed in Section 6.3.

One feature of fluorocarbon plasma processes is the deposition of a CF_x-containing polymer on the wafer during etching. The polymer strongly influences the etch rate by limiting the fluxes of reactants to the wafer, dissipating ion bombarding energy, and providing reactants for removal of oxygen from the film. SiO_2 and Si etch rates generally decrease with increasing polymer thickness due to this barrier to mass and energy transport [5, 9-10]. The first step in describing the surface reaction mechanisms is to capture the kinetics of the polymer formation. The precursors for the polymer growth are generally believed to be C_mF_n radicals with sufficient dangling bonds to build a polymeric network [6-8, 15]. For example, Oehrlein et al. observed increasing passivation thickness with increasing CF_2 density in an ICP discharge sustained in CHF_3 [5]. Booth et al observed a decreasing CF/CF_2 density toward the surface at low bias

power in a CF_4 rf plasma, indicating surface consumption of these species [16]. In our work, these polymerizing species are CF, CF_2, C_2F_3, and C_2F_4.

It has been observed that polymer layers can achieve a steady state thickness during etching [9-10], which implies that some polymer consumption processes occur simultaneously during its deposition. One such process is the F atom etching of the polymer. F atoms terminate the dangling bonds of carbon in the polymer to form volatile products such as CF_4. As F atoms can diffuse into the polymer to react internally, this process appears to be a bulk reaction. Another polymer consuming process is energetic ion sputtering. For example, Oehrlein et al. observed decreasing polymer thickness with increasing substrate bias in inductively coupled plasmas [10]. In these systems the substrate bias does not significantly change the magnitude of the reactant flux and only changes the ion bombarding energy. As such, the decreasing passivation thickness with increasing bias should be attributed to the increasing rate of ion sputtering consumption of the polymer. The sputtering process itself may be more complicated in that it may involve chemical reactions as well as physical sputtering. For example, in addition to breaking polymer bonds, the incident ions may dissociate to release F atoms which contribute to etching the film. In our reaction mechanism we included only physical ion sputtering of the polymer. Another role ions may play in polymerization kinetics is to activate surface sites. Sputtering dominates the contribution of ions to the polymerization kinetics when the ion energy is large (e.g., > 100 eV). However, when the ion energy is low (10s of eV), enhancement of polymer formation by ions has been observed. Goto et al. investigated polymer growth on a grounded surface by a CF_2 beam with an Ar microwave plasma [17]. The plasma sheath voltage at the surface is close to the floating plasma potential, which was estimated to be in the low 10s of V. This resultes in ion energies being in the low 10s of eV. They found that the polymer

deposition rate was low when only the CF_2 beam was applied, and that the deposition rates was significantly increased by applying the CF_2 beam and the Ar plasma together. These observations were attributed to the low-energy ion activation of polymeric surface sites for neutral radical sticking. With this mechanism, the low CF_2 self-sticking probability suggested by Sawin et al. [18], and the high effective CF_2 sticking rate in a low-power rf discharge environment observed by Booth et al. [16], can be rationalized. Oehrlein et al.'s observation of increasing polymer thickness with decreasing bias also covers this low-energy region and is consistent with an increase in the efficiency of the low-energy ion activation for polymerization with decreasing ion energy. We modeled the ion activation process as having an ion-energy-dependent reaction probability k of

$$k = k_0 \times \text{Max}\left(0, 1 - \frac{E_i}{E_c}\right), \quad (6.1)$$

where E_i is the incident ion energy, E_c is the maximum energy allowable for the process, and k_0 is the probability at zero incident ion energy. After being activated, the surface sites are more likely to chemisorb polymerizing neutrals.

Another consuming process for the polymer occurs at the polymer-wafer interface. Experiments have shown that for the same process conditions, thinner passivation occurs on SiO_2 than on Si [9]. After the passivation thickness exceeds one monolayer, the kinetics of polymer growth should be the same for different wafer materials if the kinetics depends only on incident neutral and ion fluxes. The observation that the polymer thickness depends on the wafer material implies that interactions at the polymer-wafer interface can consume the polymer. For SiO_2 substrates, the oxygen atoms in the film react with the carbon atoms in the polymer to release

volatile products such as CO_2 [19]. In fact, the polymer-etching ability of oxygen atoms is well known as oxygen plasmas are often used to strip photoresist. The same effect can be observed during etching [19-20]. The polymer-wafer interactions, however, require activation energy which must be provided by ion bombardment through the overlying polymer layer. During the transfer of the ion bombarding energy through the layer, some portion of the energy is dissipated in the polymer by bond breaking and heating with only a fraction reaching the surface. Consequently, the efficiency of the energy transfer decreases with increasing polymer thickness, and as a result the probabilities of polymer-wafer reactions depend on the polymer thickness. Assuming that the power transfer is governed by Fick's law, and that the power consumption at a given depth in the polymer is proportional to the power reaching the location, it can be shown that the power reaching the polymer-wafer interface exponentially decays with the polymer thickness. Considering that the polymer thickness under steady state conditions is small (on the order of nanometer), the exponential term may be expanded to a polynomial. Following this logic, we used the following semiempirical expression for the dependence of ion activation energy delivered to the surface as a function of polymer thickness:

$$c = c_0 \times \frac{1}{1 + \boldsymbol{a} \cdot [P] + \boldsymbol{b} \cdot [P]^2}, \tag{6.2}$$

where $[P]$ represents the number of polymer monolayers, c_0 is the reaction probability when no polymer is present, and $\boldsymbol{a}$ and $\boldsymbol{b}$ are constants. In this work we used $\boldsymbol{a} = 0.6$ and $\boldsymbol{b} = 0.1$. We define $\lambda = \frac{1}{1 + \boldsymbol{a} \cdot [P] + \boldsymbol{b} \cdot [P]^2}$ as the transfer coefficient.

In addition to polymer consumption, polymer-surface interactions also contribute to wafer etching. The carbon atoms in the polymer in contact with SiO_2, coincident with ion bombardment through the polymer layer, abstract oxygen atoms from the oxide. This process generates volatile CO_2 and leaves the target Si atoms in the oxide partially passivated by F atoms. The F atoms which diffuse through the polymer successively passivate the Si sites, eventually forming volatile SiF_n products. In this part of the mechanism the first layer of the polymer passivation is a precursor for etching.

Another pathway for neutral passivation of the SiO_2 wafer is through direct $CF_{x\leq 2}$ neutral chemisorption to SiO_2 sites to form SiF_xCO_2 intermediate complexes. These complexes dissociate to SiF_x surface sites and CO_2 gas upon ion bombardment or F atom passivation. As in Si etching, F atoms then saturate the dangling bonds of SiF_x until producing volatile products. Due to the comparatively thin polymer passivation on SiO_2, incident energetic ions can penetrate through the polymer and chemically sputter surface species, a process which is difficult for Si etching due to the thicker polymer layer. This gives SiO_2 fluorocarbon etching additional selectivity over Si.

6.3. Etching of SiO_2 in an C_2F_6 Plamsa

SiO_2 etching in an inductively coupled discharge sustained in C_2F_6 was investigated with the integrated plasma equipment and surface kinetics model. To enable comparison between simulated and experimental results, the reactor geometry and the process conditions follow those of Oehrlein et al. [9]. The cylindrical reactor is schematically shown in Fig. 6.2. Inductive power is supplied through a 3-turn inductive coil 16 cm in diameter. The coil sits on a 2-cm-thick quartz window that is 23 cm in diameter. A 12.5-cm-diameter wafer is placed on a

substrate located 7 cm below the quartz window. An rf bias is applied to the wafer substrate. The source gas is supplied from a gas inlet ring, which is located under the quartz window. The gas inlet flow rate is 40 sccm and the gas pressure is controlled at 6 mTorr by throttling the pump rate. The source current is at 13.56 MHz, delivering 1400 W of inductive power. The frequency of the rf bias on the wafer substrate is 3.4 MHz, and the base case amplitude of the bias is 100 V. The bias voltage is used to control the ion bombarding energy while it has a small influence on other plasma conditions. The gas phase reaction chemistry is shown in the Appendix.

Typical plasma conditions for the base case study are shown in Fig. 6.2. The electron temperature T_e peaks near the inductive source as shown in Fig. 6.2(a), where the azimuthal electric field and the power deposition are maximum. The electron temperature changes little within the plasma chamber. At this low pressure, the electron density is high (2.7×10^{11} cm^{-3}) and the electron-neutral collision frequency is small, producing a large plasma conductivity. This leads to a quite uniform plasma potential in the process chamber, as shown in Fig. 6.2(a). To balance the currents in the asymmetric reactor, a negative dc-bias voltage (namely the self-bias voltage) is generated, which is -84 V. Although the time-averaged plasma potential peaks at only 16.8 V, the sheath potential above the wafer is actually large (98 V for this case). The CF_3^+ and CF_2^+ ion densities are shown in Fig. 6.2(b) and contribute to a peak positive ion density of 4.7×10^{11} cm^{-3}. As diffusion processes dominate at low pressure, both densities peak near the center of the reactor. Since one of the major sources for CF_3^+ is the electron impact ionization of the feedstock C_2F_6 gas, whose density is largest near the ring nozzle, its peak area expands to larger radii. For CF_2^+, which is dominantly produced by ionization of dissociation products of C_2F_6, its density is more diffusion dominated. The two ion densities are of the same order,

though CF_3^+ is the most abundant ion species. CF and CF_2 radical densities are shown in Fig. 6.2(c). The high input power produces ≈ 95% dissociation of the C_2F_6. As a result, neutral products having highest densities are F, CF_2, and CF, which do not have C-C bonds. Both CF and CF_2 densities are fairly uniform.

Radical and ion fluxes to the wafer surface for the base case are shown in Fig. 6.3. As a consequence of the uniform gas phase distributions, the fluxes are also fairly uniform, in general peaking on axis. The fluxes of CF_2 and CF, the major precursors for the polymer deposition, decrease radially a bit more than the ion and F atom fluxes do, and this leads to a slight radial decrease of the polymer thickness, as shown in Fig. 6.3(c). (We used the number of polymer monolayers to represent the polymer thickness. We assumed each monolayer contains 10^{15} cm^{-2} carbon atoms. Assuming the polymer composition and density mimic $(C_2F_4)_n$, each monolayer is ≈ 6 A.) Although the decreasing polymer thickness in this range would normally enhance the rate of SiO_2 etching, the decrease in ion flux with increasing radius compensates. As a result the SiO_2 etch rate is more uniform than that of the polymer thickness, as shown in Fig. 6.3c. Fluxes of C_2F_3, C_2F_4, $C_2F_4^+$, and $C_2F_5^+$ are smaller than those of the C-monomer species due to the highly dissociating environment. The fluxes of these reactive species to the center of the wafer are listed in Table 6.2.

To investigate the influence of ion energy on SiO_2 etching, the rf bias was varied. Increasing substrate bias does not change the plasma potential noticeably; however, it does increases the magnitude of the self-bias voltage on the substrate, which increases the time averaged sheath voltage drop above the wafer. The magnitudes of the self-bias voltage V_s and the sheath voltage drop above the wafer V_d, as a function of the substrate bias, are shown in Fig. 6.4. These values are actually negative. We will being referring to the magnitude in our

discussion. Both V_s and V_d increase linearly with substrate bias. A similar linear relationship between the self-bias voltage and substrate bias power was obtained by Oehrlein et al. in a CHF_3 discharge produced in the identical reactor under the same process conditions [21]. In our simulations we observed little variation of the magnitude of ion flux with substrate bias voltage (<3%) in the process range. This agrees with the observation by Oehrlein et al. that the ion current density measured with a Langmuir probe changes little with rf bias power [21]. Since the bias power is approximately the product of total ion flux and sheath potential, the relationship between bias power and bias voltage is also linear. So our simulation results about the linear dependencies of V_s and V_d on the bias voltage are equivalent to their experimental conclusion.

The polymer thickness as a function of the self-bias voltage for different E_c, the maximum energy for ion activation of polymerizing sites, is shown in Fig. 6.5. When no such ion activation process is used ($E_c = 0$), decreasing polymer thickness with increasing V_s was observed, which is due to the increasing ion sputtering of the polymer. This produces an increase in the wafer etch rate with increasing V_s as shown in Fig. 6.5(b). The decreasing polymer thickness favors transfer of energy and etchant through the passivation to the wafer surface. The general trends obtained with $E_c = 0$ agree with most experimental reports [9-10]. However, the sharp increase in passivation thickness and the sharp decrease in etch rate with decreasing V_s in the low-bias region, which are observed experimentally [9-10], are not captured with $E_c = 0$. This implies that there may be some additional low-energy-ion assisted polymerization process. We included such a process in the mechanism, using an energy-dependent activation efficiency as described in Eq. 6.1. The polymer thickness in the low-bias region is sensitive to the maximum ion activation energy E_c. For example, when $E_c = 65$ eV, a sharp increase of polymer thickness with decreasing V_s was obtained at low biases, as shown in

Fig. 6.5(a). The increasing thickness results in less efficient wafer etching processes involving energy transfer or species diffusion through the polymer, as shown by the transfer coefficient λ in Fig. 6.5(c). This leads to a decrease in etch rate at E_c = 65 eV as compared with E_c = 0. The differences in polymer thickness and etch rate between E_c = 65 eV and E_c = 0 increases with decreasing bias because the ion activation efficiency increases with decreasing ion energy. A further increase in E_c to 85 eV provides an additional increase of polymer thickness and decrease in etch rate in the low bias region.

To evaluate our model and to calibrate simulation parameters, computed results were compared to experiments [9] for SiO_2 and Si etch rates versus self-bias voltage, as shown in Fig. 6.6(a) where E_c = 65 eV in the model. The experimental process conditions are the same as in the simulation. There is generally good agreement. The etch selectivity of SiO_2 over Si is due to the difference in the deposition of the passivation. Ion-assisted polymer-wafer interactions occur for SiO_2 etching, which, for lack of oxygen atoms present to react with the polymer, are absent from Si etching. This leads to thinner polymer passivation on SiO_2 than on Si under the same process conditions, and more efficient transfers of energy and reactants to the wafer surface in SiO_2 etching, as shown in Fig. 6.6(b). The thin passivation on SiO_2 also makes it possible for energetic ions to penetrate through the polymer and chemically sputter the wafer [9, 22], contributing to additional selectivity over Si.

To investigate etching behavior at high ion energies, we extended our study to higher biases than were covered in the experiments. Other process parameters follow those for the base case. The SiO_2 etch rate and the polymer thickness as a function of the self-bias voltage are shown in Fig. 6.7(a) in solid lines. Process parameters other than the substrate bias follow those in the base case. The passivating neutral-to-ion flux ratio is 12. The average ion energy is

approximately the same as the bias voltage. In the high ion energy range (> 150 eV), the etch rate tends to saturate. This is due to the depletion of the polymer passivation. Recall that etching of SiO_2 requires CF_x for volatilization of both the Si and O. The CF_x can be supplied either directly by neutral adsorption or by the first layer of passivation. When the ion energy exceeds 150 eV, the passivation drops below one monolayer over the SiO_2 wafer. For ion energies greater than 250 eV, the passivation covers only a small fraction (~0.3) of surface sites. As a result, the etch process is limited by the availability of neutral passivation which serves as a precursor for SiO_2 etching. If this analysis is correct, decreasing the neutral flux in the passivation-starved etch region should decrease the etch rate, while in the low-energy regime where the polymer thickness is already above one layer, the etch rate should increase. The passivating neutral flux was artificially decreased by 30% with respect to that obtained in the base case simulation. The resulting passivating neutral-to-ion flux ratio is around 8.4. The results are shown in Fig. 6.7(a) in dashed lines. Through the entire energy range the polymer thickness decreases with decreasing passivating neutral flux. In the low-energy region, where the polymer is thick and its major influence is limiting the transfer of energy and species, the decrease of polymer thickness leads to an increase in the etch rate. In the high-energy region, the polymer is thin, so its influence on energy or species transfer is less significant. Under such conditions the availability of passivation limits wafer etching, and so decreasing passivation by reducing neutral flux actually leads to a drop in the etch rate. These trends are not observed for Si, as shown in Fig. 6.7(b). Here the etch rate always increases with decreasing passivating neutral flux and decreasing polymer thickness, because the passivation layer does not serve as a precursor for Si etching.

The etch selectivity of SiO_2 over Si for the two passivating neutral-to-ion flux ratios, as a function of self-bias voltage, is shown in Fig. 6.7(c). The high ICP power produces a high density of F atoms, which etch polymer layers in both SiO_2 and Si processing. As a result the polymer-wafer interactions do not dominate polymer consumption during SiO_2 etching, and under the same process conditions the difference in polymer thickness on SiO_2 and Si is not large. As a result the etch selectivity obtained is not large. For these process conditions, decreasing the passivating neutral flux leads to a larger decrease of passivation on Si than on SiO_2. As a result the etch selectivity decreases with decreasing passivating neutral flux.

Due to the lack of fundamental data, the reaction probabilities used in the model were more or less determined by the calibration with experiments from Oehrlein et al. [9]. Some of these reaction probabilities may change with reactor conditions. For example, neutral sticking probabilities change with surface temperature [5]. Given these uncertainties in choosing the probabilities, it is valuable to investigate the sensitivity of the model to variations of these parameters. We first examined the sticking coefficient $\boldsymbol{s}$ for a passivating neutral to polymerize on an un-activated polymer surface site. The base case value is $\boldsymbol{s}$ = 0.005, and σ was parameterized from 0.003 to 0.007. The radial distributions of polymer thickness and etch rate for different $\boldsymbol{s}$ values are shown in Fig. 6.8. The substrate bias was 100 V. The polymer thickness increases with increasing $\boldsymbol{s}$ because of the increase in deposition source. The increase in polymer thickness produces a decrease in the etch rate. Since there is no ion-assisted polymerization at this bias ($E_c < E_{ion}$), neutral polymerization occurs only at unactivated sites. As a result, the increase in polymer thickness is approximately proportional to the increase in $\boldsymbol{s}$. The polymer thickness and etch rate as a function of the self-bias voltage for different values of $\boldsymbol{s}$ are shown in Fig. 6.8(c) and 6.8(d) respectively. The absolute increase in polymer thickness is

proportional to the increase in $\boldsymbol{s}$. However, in the low-bias region, because there is additional passivation on activated sites, the relative change in polymer with varying $\boldsymbol{s}$ is smaller than that in the high bias region. For $\boldsymbol{s}$ = 0.007, the polymer is more than one monolayer throughout the bias range. Consequently, the SiO_2 etch rate increases with V_s with a slope that changes little from low to high biases, as shown in Fig. 6.8(d). With smaller σ, at high biases the polymer thickness drops below one monolayer, and that leads to the saturation of the etch rate.

Since ion sputtering is a major consumption of the polymer, its probability was also parameterized. The polymer thickness as a function of p_0 for different substrate biases is shown in Fig. 6.9(a). In the base case we used p_0 = 0.025. For all biases the polymer thickness decreases with increasing p_0. When the bias is low (< 40 V), the small ion sputtering rate and the ion-assisted polymerization combine to make the passivation thick. As a consequence the etch rates are low. When the bias voltage is high (100 or 170 V), the polymer is thin and to a large degree its consumption is determined by the ion sputtering process. So increasing p_0 leads to a large decrease in the polymer thickness at high biases. Consequently the etch rates increase noticeably with increasing p_0 for 100- and 170-V biases, as shown in Fig. 6.9(b). For 170-V bias, the polymer drops below one monolayer at large p_0, and so the etch rate tends to saturate with increasing p_0.

Direct reactions of ions and wafer surface may occur in SiO_2 etching where the polymer passivation is thin. We investigated the sensitivity of the model to the probability of ion etching of SiF_3 surface species that produces volatile SiF_4 and exposes new SiO_2. This reaction is $C_xF_y{}^+{}_g + SiF_{3s} \rightarrow C_xF_{y-1} + SiF_{4g} + SiO_{2s}$. In the base case we assumed an ion etch probability $\boldsymbol{h}$ of 0.11 for a 70-eV ion hitting a bare surface (no polymer coverage). According to Eqs. 3.11 and 6.2, this corresponds to an effective etch probability of 0.064 because the base case produces an

average ion energy of 98 eV and a polymer coverage of 1.94 layers. The SiO_2 etch rate and the SiF_3 surface coverage as a function of $\boldsymbol{h}$ are shown in Fig. 6.10. With increasing $\boldsymbol{h}$ from 0 to unity, a decrease of SiF_3 coverage from 0.22 to 0.03 results, which is accompanied by an increase in the etch rate from 380 to 495 nm/min. The reason that at $\boldsymbol{h} = 0$ the SiF_3 coverage is not high is that F atoms also etch the species. When $\boldsymbol{h}$ is small (< 0.4), the SiF_3 coverage drops fast with increasing $\boldsymbol{h}$, and the etch rate is sensitive to variation of $\boldsymbol{h}$. In the large $\boldsymbol{h}$ region (> 0.4), since the SiF_3 coverage is depleted to a small value, further increase of $\boldsymbol{h}$ does not significantly change the coverage. As a result, the etch rate changes little with varying $\boldsymbol{h}$. Note that for $\boldsymbol{h} = 0$, the etch rate is still ≈ 385 nm/min. This rate is a consequence of ion-activated etching but not of direct ion etching.

6.4. Profile Simulations of SiO_2 Etching by C_2F_6 Plasma

In microelectronics fabrication, one frequent and challenging application of fluorocarbon plasma etching of SiO_2 is to produce vias with high aspect ratio (HAR). Due to complex surface reactions on the bottom and sidewalls of the trench, etch profiles often deviate from the vertically straight ideal. To investigate the mechanisms responsible for profile evolution, we used the surface reaction mechanism described above in the MCFPM to model SiO_2 profile evolution. Since the MCFPM uses a Monte Carlo algorithm for surface reactions, the analytical approach describing the polymer-thickness-dependent reactions that is used in the equipment scale model needed to be modified. In the feature scale model, thick polymer coverage occurs by “stacking” mesh cells representing polymer on the surface. The height of the polymer mesh cells is equivalent to the polymer thickness. The polymer-thickness-dependent plasma-wafer reactions

are realized by the fact that increasing polymer cells decreases the chance for the wafer surface to be exposed to the plasma and to react.

It has been found experimentally that in HAR etching of SiO_2 by fluorocarbon plasmas, tapering of the trench generally occurs under conditions where there is excessive passivation [23]. We simulated processes of HAR SiO_2 etching by the previously described C_2F_6 plasma. Although some mask erosion by direct sputtering was allowed, the mask remains largely intact. Trench profiles after equal etch times at 100- and 160-V substrate biases are shown in Fig. 6.11(a). There is a shrink of the critical trench dimension at the bottom of the profiles at both biases. The trench is less tapered with the higher bias, and the trench depth at the higher bias is larger after equal etch times. The tapered profiles are attributed to the strong sidewall passivation. Since neutral fluxes have broad angular distributions and low sticking coefficinets, they reflect many times in the trench, eventually sticking to the sidewalls and the bottom of the trench at nearly equal rates. However, ion bombardment has narrow ion angular distributions. As a result, most ions at best graze sidewalls and reflect specularly, having a low reaction probability, while the bottom of the trench receives a larger normal flux having higher reaction probability. This leads to stronger passivation on the sidewall than at the bottom. During etching the sidewall passivation grows, shadowing the area of the bottom that can receive vertical ion bombardment and leading to a tapered profile of the trench. With increasing bias voltage, the ion incident energy increases, resulting in a larger sputtering yield of the polymer. The increasing polymer consumption leads to both a broader critical dimension at the bottom, and a higher etch rate, as shown in Fig. 6.11(a).

To investigate the range of such a bias dependence in etching, we performed profile simulations at a range of higher biases. We use the ratio of the trench width at 0.5 μm above the

bottom of the trench (W_b) to the width at the top (W_t) to represent the degree of tapering, and the trench depth after equal etch times to represent the etch rate. The ratio W_b/W_t and the trench depth as a function of the substrate bias are shown in Fig. 6.11(b). With increasing substrate bias from 100 V to 300 V, initially both W_b and the trench depth increases due to increasing sputtering of the passivation and higher ion activation rates. In the high bias region, both metrics tend to saturate. That is because insufficient passivation at high biases limits the etching process. The dependence of the etch rate on the substrate bias obtained from our profile simulation agrees well with that obtained from the equipment scale modeling discussed earlier.

As tapering is produced by sidewall passivation, it is related to the ratio of the flux of passivating neutrals to ions, $\boldsymbol{w} = \Phi_n/\Phi_{ion}$. To investigate the influence of ω on the etch profiles, we artificially scaled the neutral fluxes from the base case ($\boldsymbol{w}$ = 12) while keeping other parameters the same. (Although the fluxes so obtained may not specifically correspond to given process parameters, this methodology is helpful in understanding the mechanism of etching.) Trench profiles for different $\boldsymbol{w}$ are shown in Fig. 6.12(a). W_b/W_t and trench depth after equal etch times as a function of $\boldsymbol{w}$ are shown in Fig. 6.12(b). In these figures $\boldsymbol{w}$ has been normalized to that obtained from the base case, with $\boldsymbol{w}$ = 100% corresponding to the base case. The base case produces a tapered profile due to the strong passivation. With decreasing $\boldsymbol{w}$, the passivation decreases, leading to increasing etch rates and less tapered profiles. When $\boldsymbol{w}$ decreased to 70%, a nearly straight trench was obtained. Further decrease of $\boldsymbol{w}$, however, leads to an insufficient sidewall passivation. As a result the sidewalls are also etched to some degree, leading to a bowed profile at low $\boldsymbol{w}$, as shown in Fig. 6.13(a). The critical dimension W_b/W_t then exceeds unity. These results demonstrate that, to obtain optimal feature profiles, The proper balance of ion and neutral fluxes in the process is important.

One effective approach for controlling ***w*** is dilute the C_2F_6 with a chemically inert gas. By adding Ar to the feedstock C_2F_6, the passivating neutral densities are diluted, while ion densities are to some degree enhanced due to larger ionization cross sections of Ar. As a result, increasing the ratio of Ar/C_2F_6 in the feedstock gas decreases ***w***. To investigate the effect of gas mixture on feature profiles, we performed simulations at different Ar/C_2F_6 ratios when keeping other process parameters the same as in the base case. The profiles after reaching nearly equal depths are shown in Fig. 6.13(a). Normalized ***w*** and W_b/W_t as a function of Ar fraction are shown in Fig. 6.13(b), and ω decreases with increasing Ar fraction. The base case, which has no Ar, produced a tapered profile. With 20% Ar, a nearly straight trench was obtained because of the decrease in ω. Further increase of the Ar fraction to 40% leads to a bowed profile due to insufficient sidewall protection by passivation, and the bowing increases with increasing Ar fraction to 60%.

6.5. Concluding Remarks

A surface reaction mechanism accounting for polymer passivation and passivation-thickness-dependent wafer etching has been developed for SiO_2 etching by fluorocarbon plasma. The polymer is formed by C_xF_y neutral deposition and is consumed by ion sputtering and F atoms etching. Low-energy ion activation of surface sites assists neutral polymerization. The thickness of the polymer is determined by the balance of its formation and consumption. SiO_2 etching is preceded by neutral passivation, and it evolves through either ion chemical sputtering or successive fluorination. Since plasma-wafer interactions involve transfers of energy and species through the polymer, their rates scale inversely with the polymer thickness. The etch

selectivity of SiO_2 over Si is attributed to the thinner polymer passivation on the SiO_2 surface as a result of polymer-SiO_2 interactions.

The reaction mechanism was first applied to an integrated plasma equipment model to investigate the SiO_2 etching by an ICP discharge sustained in C_2F_6. Increasing substrate bias increases the ion bombarding energy while hardly changing other plasma properties. Consequently the polymer thickness decreases with increasing bias due to increasing polymer yield by ion sputtering, producing an increase in the etch rate. Increasing E_c, the maximum ion activation energy for polymerization, leads to increasing polymer thickness and lower etch rate in the low bias region. Good agreement with experiments for the bias-dependent etch rates of SiO_2 and Si was obtained at E_c = 65 eV. The SiO_2 etch rate saturates at high ion energy due to depletion of passivation. Therefore increasing neutral flux at high biases increases the etch rate while decreasing the etch rate at low bias. The sensitivity of the model to major simulation parameters was also investigated. The etch rate decreases with increasing probability for neutral sticking. When the bias is high, the etch rate is sensitive to the probability for ion sputtering of the polymer. The etch rate is insensitive to the variation of the probability for reactive ion etching when the probability is high, because in that region the fluorinated surface species are depleted.

The surface reaction mechanism was also applied to a feature scale model to investigate the SiO_2 profiles produced by the C_2F_6 discharge. Simulations produced tapered trenches in HAR SiO_2 etching, an effect attributed to the strong sidewall passivation. Increasing bias leads to less tapered profiles due to increasing ion sputtering of the polymer. The dependence of the etch rate on the substrate bias obtained in the feature model (the increase of etch rate until saturating at high biases) is similar to that obtained in the equipment scale model. A tapered

profile transitions to a straight profile and further to a bowed feature with decreasing passivating neutral-to-ion flux ratio Φ_n/Φ_{ion}, accompanied by an increase in the etch rate. The ratio Φ_n/Φ_{ion} decreases with increasing Ar fraction in an Ar/C_2F_6 mixture, and profile optimization can be achieved by controlling the Ar fraction.

Table 6.1. Surface Reaction Mechanism

Species Definitions:

X_g	Gas phase species
X_s	Surface site
P	Polymer layer component
P*	Low-energy-ion activated polymerization site

Reaction[a, b]	Probability	Note
Polymer Formation:		
$CF_{2g} + SiO_{2s} \rightarrow P + SiO_{2s}$	0.0033	c
$CF_{2g} + Si_s \rightarrow P + Si_s$	0.0033	c, i
$CF_{2g} + P \rightarrow P + P$	0.005	e, j
$CF_{2g} + P^* \rightarrow P + P$	0.08	e, j
$CF_g + SiO_{2s} \rightarrow P + SiO_{2s}$	0.0033	c
$CF_g + Si_s \rightarrow P + Si_s$	0.0033	c, i
$CF_g + P \rightarrow P + P$	0.005	e, j
$CF_g + P^* \rightarrow P + P$	0.08	e, j
$C_2F_{3g} + SiO_{2s} \rightarrow P + P + SiO_{2s}$	0.0033	c
$C_2F_{3g} + Si_s \rightarrow P + P + Si_s$	0.0033	c, i
$C_2F_{3g} + P \rightarrow P + P + P$	0.005	e, j
$C_2F_{3g} + P^* \rightarrow P + P + P$	0.08	e, j
$C_2F_{4g} + SiO_{2s} \rightarrow P + P + SiO_{2s}$	0.0033	c
$C_2F_{4g} + Si_s \rightarrow P + P + Si_s$	0.0033	c, i
$C_2F_{4g} + P \rightarrow P + P + P$	0.005	e, j
$C_2F_{4g} + P^* \rightarrow P + P + P$	0.08	e, j
Polymer Consumption:		
$F_g + P \rightarrow CF_{4g}$	0.00057	h, j
$CF_3{}^+{}_g + P \rightarrow CF_{3g} + CF_{2g}$	$p_0 = 0.0225$	e, f, j
$CF_2{}^+{}_g + P \rightarrow CF_{2g} + CF_{2g}$	$p_0 = 0.0225$	e, f, j
$C_2F_4{}^+{}_g + P \rightarrow C_2F_{4g} + CF_{2g}$	$p_0 = 0.0225$	e, f, j

Table 6.1. Continued

$C_2F_5{}^+{}_g + P \rightarrow C_2F_{5g} + CF_{2g}$	$p_0 = 0.0225$	e, f, j
$Ar^+{}_g + P \rightarrow Ar_g + CF_{2g}$	$p_0 = 0.0225$	e, f, j
Low-energy Ion Activation of Polymerization Site:		
$CF_3{}^+{}_g + P \rightarrow CF_{3g} + P^*$	$k_0 = 0.011$	e, g, j
$CF_2{}^+{}_g + P \rightarrow CF_{2g} + P^*$	$k_0 = 0.011$	e, g, j
$C_2F_4{}^+{}_g + P \rightarrow C_2F_{4g} + P^*$	$k_0 = 0.011$	e, g, j
$C_2F_5{}^+{}_g + P \rightarrow C_2F_{5g} + P^*$	$k_0 = 0.011$	e, g, j
$Ar^+{}_g + P \rightarrow Ar_g + P^*$	$k_0 = 0.011$	e, g, j
Ion Assisted Polymer-SiO_2 Interaction:		
$CF_3{}^+{}_g + P + SiO_{2s} \rightarrow SiF_{2g} + CO_{2g} + CF_{3g} + SiO_{2s}$	$p_0 = 0.023$	d, f
$CF_2{}^+{}_g + P + SiO_{2s} \rightarrow SiF_{2g} + CO_{2g} + CF_{2g} + SiO_{2s}$	$p_0 = 0.023$	d, f
$C_2F_4{}^+{}_g + P + SiO_{2s} \rightarrow SiF_{2g} + CO_{2g} + C_2F_{4g} + SiO_{2s}$	$p_0 = 0.023$	d, f
$C_2F_5{}^+{}_g + P + SiO_{2s} \rightarrow SiF_{2g} + CO_{2g} + C_2F_{5g} + SiO_{2s}$	$p_0 = 0.023$	d, f
$Ar^+{}_g + P + SiO_{2s} \rightarrow SiF_{2g} + CO_{2g} + Ar_g + SiO_{2s}$	$p_0 = 0.023$	d, f
Neutral Passivation:		
$CF_{2g} + SiO_{2s} \rightarrow SiF_2CO_{2s}$	0.0085	d
$CF_g + SiO_{2s} \rightarrow SiFCO_{2s}$	0.0085	d, j
Fluorination:		
$F_g + Si_s \rightarrow SiF_s$	0.008	d, j
$F_g + SiF_s \rightarrow SiF_{2s}$	0.008	d, j
$F_g + SiF_{2s} \rightarrow SiF_{3s}$	0.0085	d, j
$F_g + SiF_{3s} \rightarrow SiF_{4g} + SiO_{2s}$	0.0085	d, j
$F_g + SiF_{3s} \rightarrow SiF_{4g} + Si_s$	0.0085	d, j
$F_g + SiF_2CO_{2s} \rightarrow SiF_{3s} + CO_{2g}$	0.0085	d
$F_g + SiFCO_{2s} \rightarrow SiF_{2s} + CO_{2g}$	0.0085	d

Table 6.1. Continued

Ion Activated Dissociation:

$CF_3{}^+{}_g + SiF_2CO_{2s} \rightarrow SiF_{2s} + CF_{3g} + CO_{2g}$	$p_0 = 0.1$	d, f
$CF_3{}^+{}_g + SiFCO_{2s} \rightarrow SiF_s + CF_{3g} + CO_{2g}$	$p_0 = 0.1$	d, f
$CF_2{}^+{}_g + SiF_2CO_{2s} \rightarrow SiF_{2s} + CF_{2g} + CO_{2g}$	$p_0 = 0.1$	d, f
$CF_2{}^+{}_g + SiFCO_{2s} \rightarrow SiF_s + CF_{2g} + CO_{2g}$	$p_0 = 0.1$	d, f
$C_2F_4{}^+{}_g + SiF_2CO_{2s} \rightarrow SiF_{2s} + C_2F_{4g} + CO_{2g}$	$p_0 = 0.1$	d, f
$C_2F_4{}^+{}_g + SiFCO_{2s} \rightarrow SiF_s + C_2F_{4g} + CO_{2g}$	$p_0 = 0.1$	d, f
$C_2F_5{}^+{}_g + SiF_2CO_{2s} \rightarrow SiF_{2s} + C_2F_{5g} + CO_{2g}$	$p_0 = 0.1$	d, f
$C_2F_5{}^+{}_g + SiFCO_{2s} \rightarrow SiF_s + C_2F_{5g} + CO_{2g}$	$p_0 = 0.1$	d, f
$Ar^+{}_g + SiF_2CO_{2s} \rightarrow SiF_{2s} + Ar_g + CO_{2g}$	$p_0 = 0.1$	d, f
$Ar^+{}_g + SiFCO_{2s} \rightarrow SiF_s + Ar_g + CO_{2g}$	$p_0 = 0.1$	d, f

Ion Chemical Sputtering:

$CF_3{}^+{}_g + SiF_s \rightarrow SiF_{2g} + CF_{2g} + SiO_{2s}$	$p_0 = 0.11$	d, f
$CF_3{}^+{}_g + SiF_{2s} \rightarrow SiF_{2g} + CF_{3g} + SiO_{2s}$	$p_0 = 0.11$	d, f
$CF_3{}^+{}_g + SiF_{3s} \rightarrow SiF_{4g} + CF_{2g} + SiO_{2s}$	$p_0 = 0.11$	d, f
$CF_2{}^+{}_g + SiF_s \rightarrow SiF_{2g} + CF_g + SiO_{2s}$	$p_0 = 0.11$	d, f
$CF_2{}^+{}_g + SiF_{2s} \rightarrow SiF_{2g} + CF_{2g} + SiO_{2s}$	$p_0 = 0.11$	d, f
$CF_2{}^+{}_g + SiF_{3s} \rightarrow SiF_{4g} + CF_g + SiO_{2s}$	$p_0 = 0.11$	d, f
$C_2F_4{}^+{}_g + SiF_s \rightarrow SiF_{2g} + C_2F_{3g} + SiO_{2s}$	$p_0 = 0.11$	d, f
$C_2F_4{}^+{}_g + SiF_{2s} \rightarrow SiF_{2g} + C_2F_{4g} + SiO_{2s}$	$p_0 = 0.11$	d, f
$C_2F_4{}^+{}_g + SiF_{3s} \rightarrow SiF_{4g} + C_2F_{3g} + SiO_{2s}$	$p_0 = 0.11$	d, f
$C_2F_5{}^+{}_g + SiF_s \rightarrow SiF_{2g} + C_2F_{4g} + SiO_{2s}$	$p_0 = 0.11$	d, f
$C_2F_5{}^+{}_g + SiF_{2s} \rightarrow SiF_{2g} + C_2F_{5g} + SiO_{2s}$	$p_0 = 0.11$	d, f
$C_2F_5{}^+{}_g + SiF_{3s} \rightarrow SiF_{4g} + C_2F_{4g} + SiO_{2s}$	$p_0 = 0.11$	d, f
$Ar^+{}_g + SiF_s \rightarrow SiF_g + Ar_g + SiO_{2s}$	$p_0 = 0.11$	d, f
$Ar^+{}_g + SiF_{2s} \rightarrow SiF_{2g} + Ar_g + SiO_{2s}$	$p_0 = 0.11$	d, f
$Ar^+{}_g + SiF_{3s} \rightarrow SiF_{3g} + Ar_g + SiO_{2s}$	$p_0 = 0.11$	d, f

Table 6.1. Continued

Notes:

a. Unless otherwise specified, all ions neutralize on all surfaces, returning as their neutral counterparts.
b. All gas phase species have units of flux ($cm^{-2}s^{-1}$). All surface species have units of fractional coverage.
c. Process limits to surface sites not covered by polymer.
d. Process rate depends on the polymer coverage. See Eq. 6.2.
e. Process limits to the top layer of the polymer.
f. See Eq. 3.11. $E_r = 70$ eV, $E_{th} = 3$ eV.
g. See Eq. 6.1. $E_c = 65$ eV unless otherwise specified.
h. Bulk process.
i. Equivalent process in Si etching.
j. Process also valid for Si etching.

Table 6.2. Reactant Fluxes to the Center of the Wafer[a]

Species	Fluxes ($cm^{-2}s^{-1}$)
CF_2	5.58×10^{17}
CF	2.28×10^{17}
C_2F_3	9.50×10^{14}
C_2F_4	1.02×10^{15}
F	1.21×10^{18}
CF_3^+	4.78×10^{16}
CF_2^+	1.74×10^{16}
$C_2F_4^+$	2.28×10^{14}
$C_2F_5^+$	3.45×10^{13}

Note:

a. Process Conditions: C_2F_6, 1400 W ICP power, 6 mTorr, 40 sccm gas flow rate, 100 V bias.

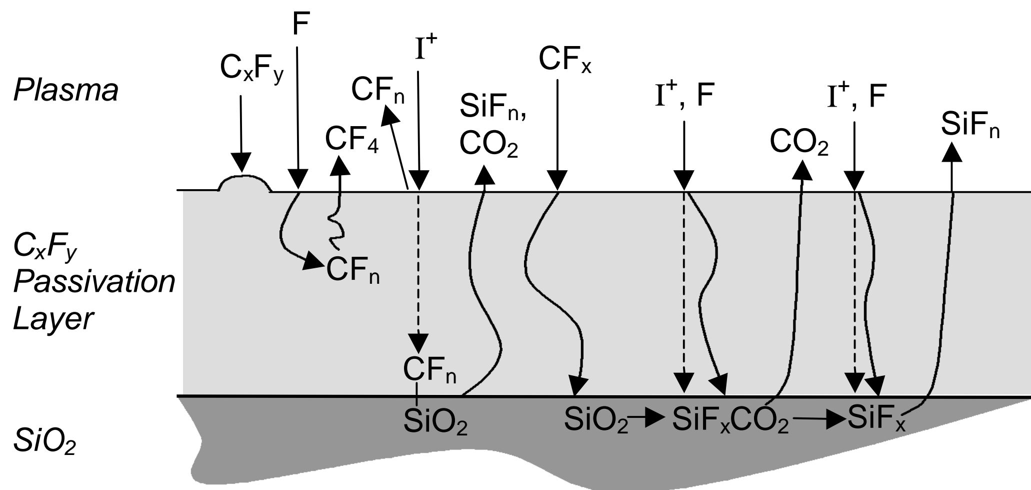

Fig. 6.1. Schematic of the surface reaction mechanism for SiO_2 etching by fluorocarbon plasma.

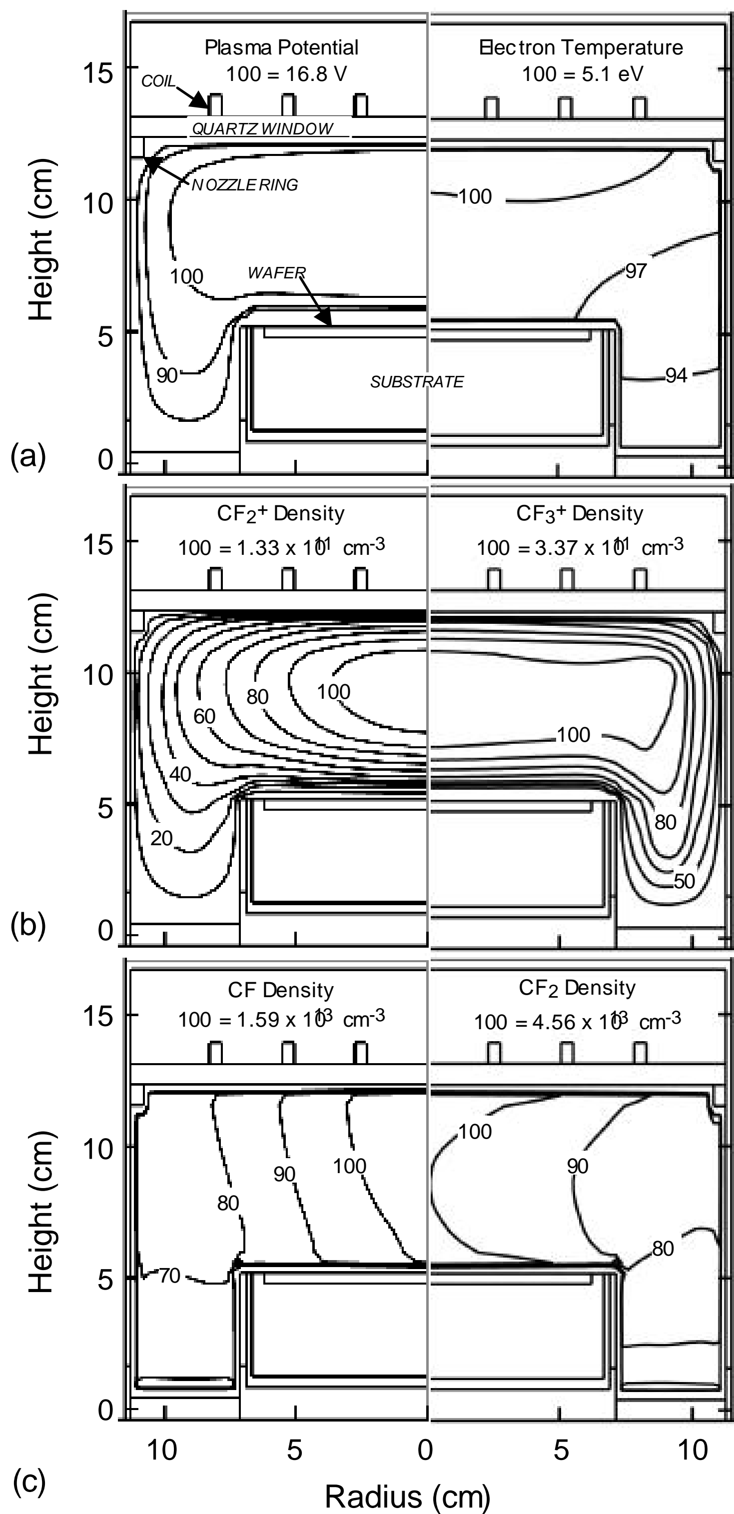

Fig. 6.2. Plasma properties for the base case simulation (C_2F_6, 1400 W ICP power, 6 mTorr, 40 sccm, 100 V bias. (a) Plasma potential and electron temperature. (b) CF_2^+ and CF_3^+ ion densities. (c) CF and CF_2 densities. The labels on the contour lines are percentage of the maximum value shown at the top of each figure.

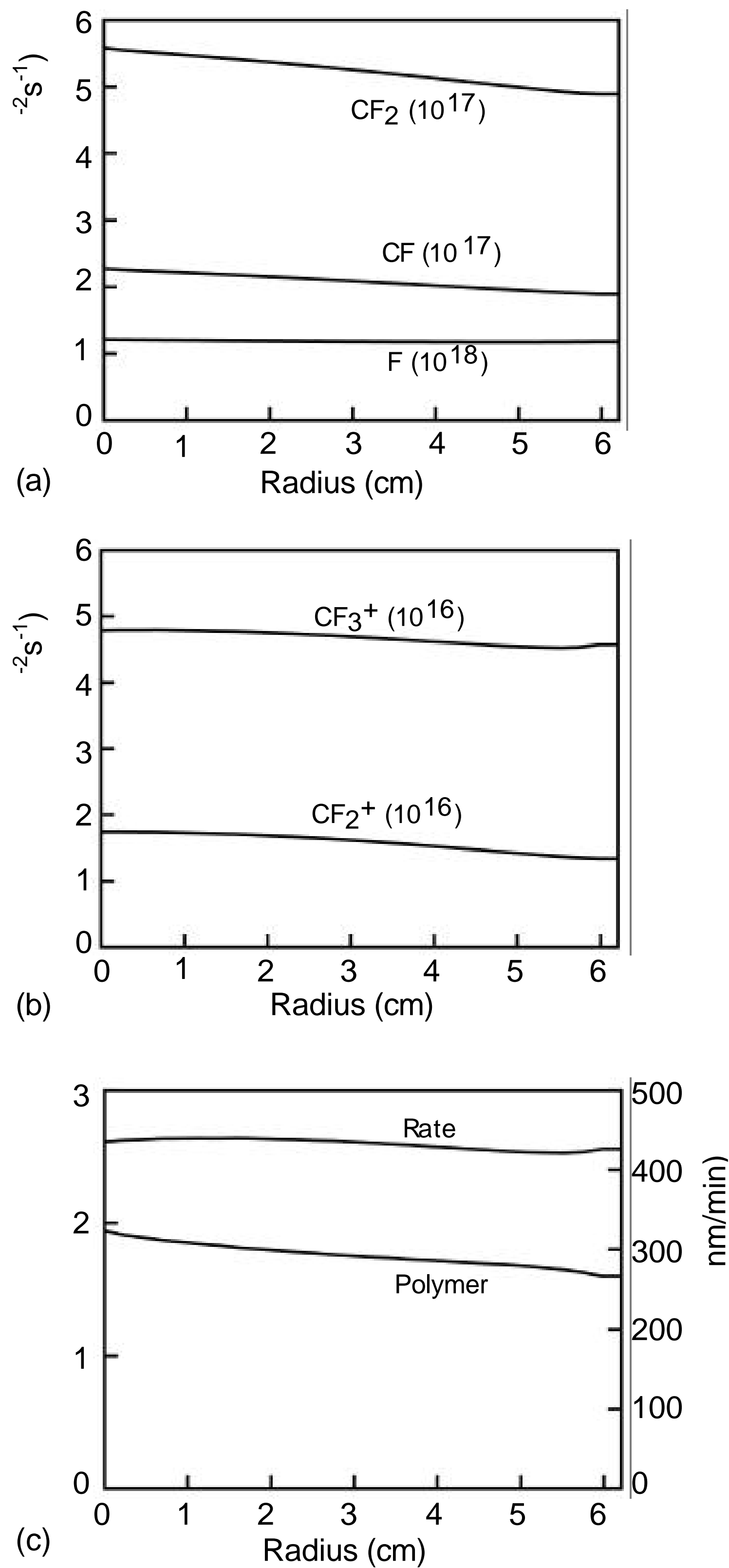

Fig. 6.3. Plasma and process properties on the wafer as a function of radius for the base case. (a) Fluxes of CF_2, CF, and F. (b) Fluxes of CF_3^+ and CF_2^+. (c) Polymer thickness and etch rate.

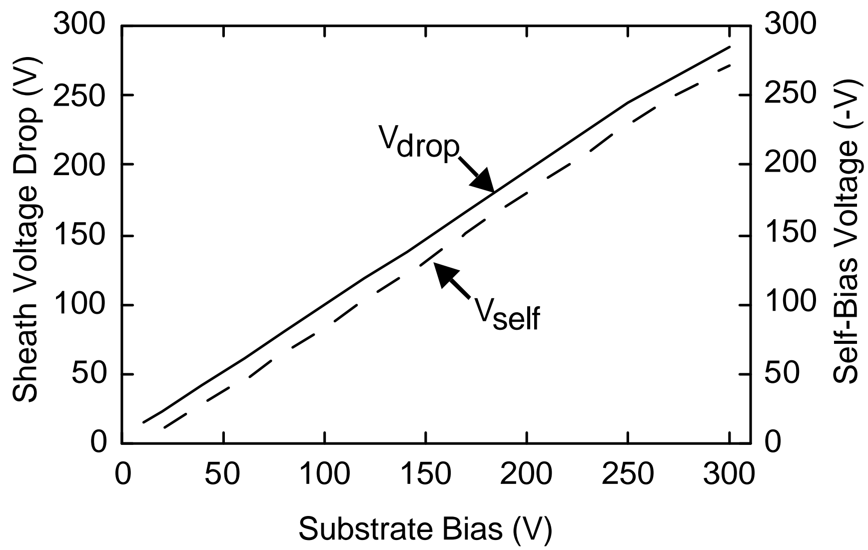

Fig. 6.4. Sheath voltage drop and self-bias voltage on the wafer surface as a function of substrate bias. The self-bias voltages are negtive.

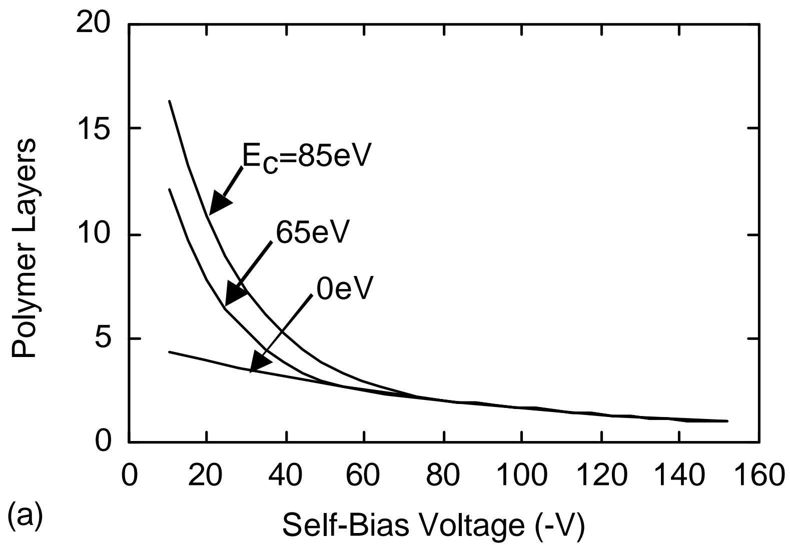

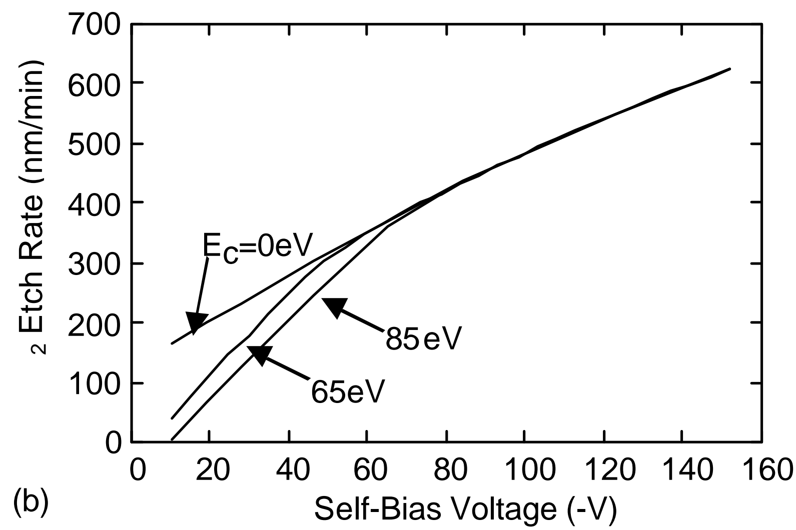

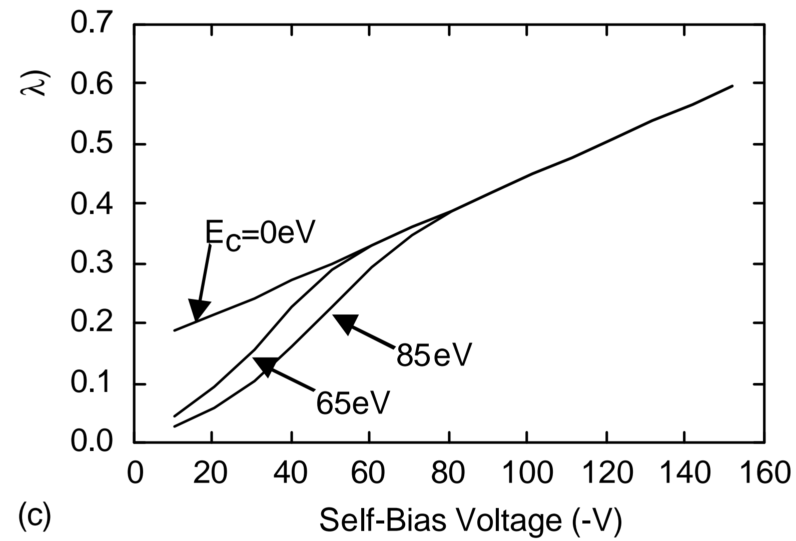

Fig. 6.5. Surface process properties as a function of self-bias voltage at different E_c. (a) Polymer thickness. (b) SiO_2 etch rate. (c) Transfer coefficient (λ).

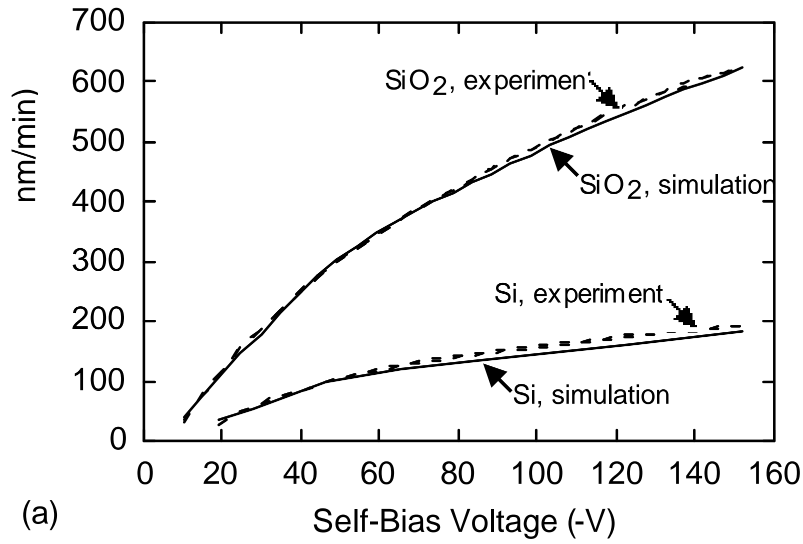

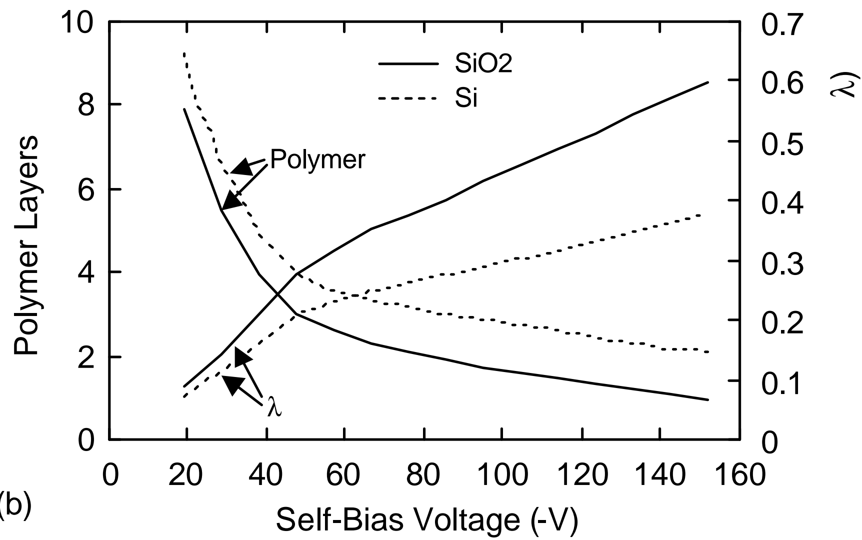

Fig. 6.6. SiO_2 and Si etch properties as a function of self-bias voltage. (a) Simulated and experimental results [9] of etch rates. Simulation results were obtained at $E_c = 65$ eV. (b) Simulation results of polymer thickness and transfer coefficient (λ) at $E_c = 65$ eV.

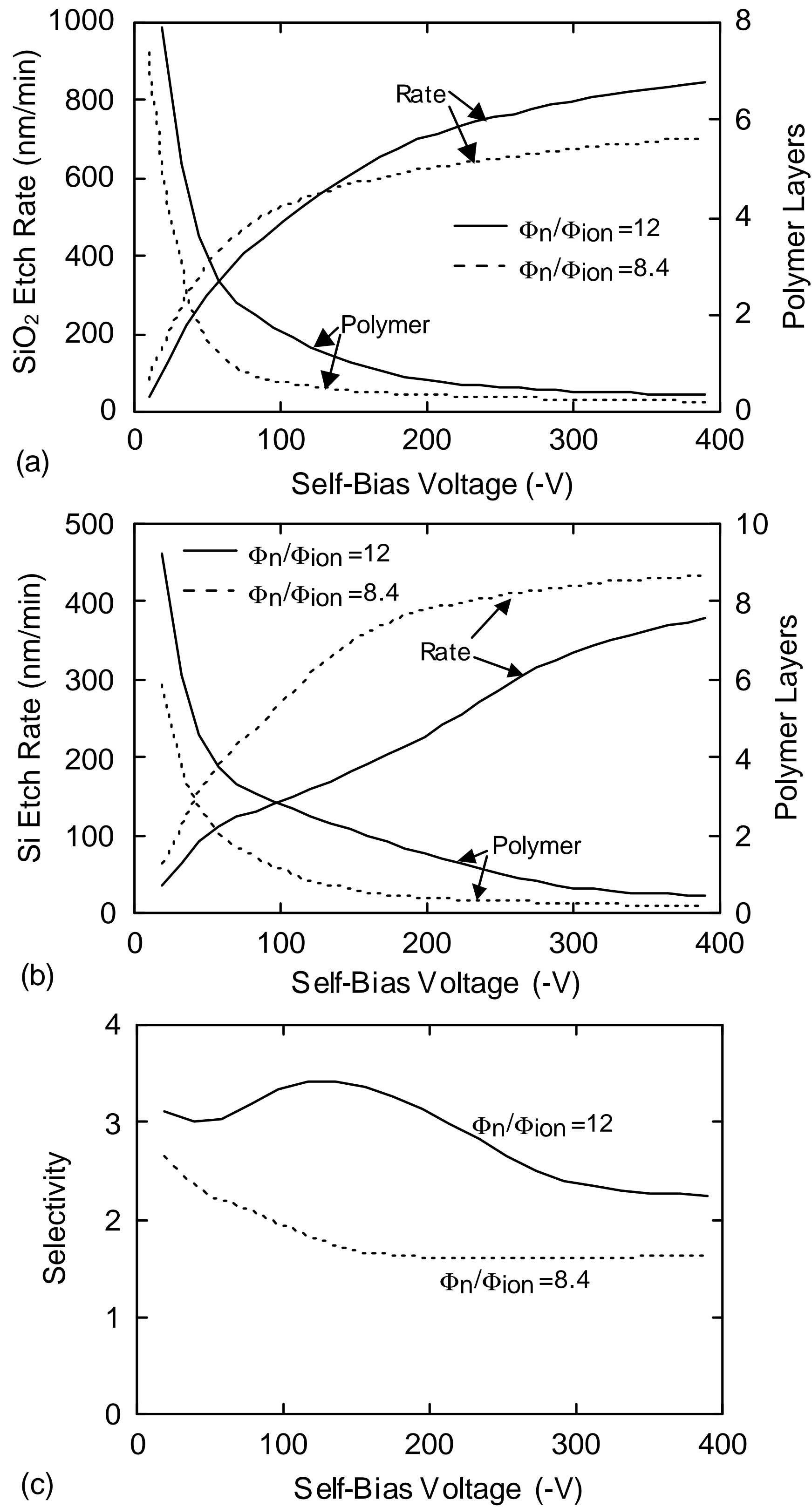

Fig. 6.7. SiO_2 and Si etch properties as a function of ion energy at different passivating neutral to ion flux ratios (Φ_n/Φ_{ion}). (a) Polymer thickness and etch rate in SiO_2 etching. (b) Polymer thickness and etch rate in Si etching. (c) Etch selectivity of SiO_2 over Si.

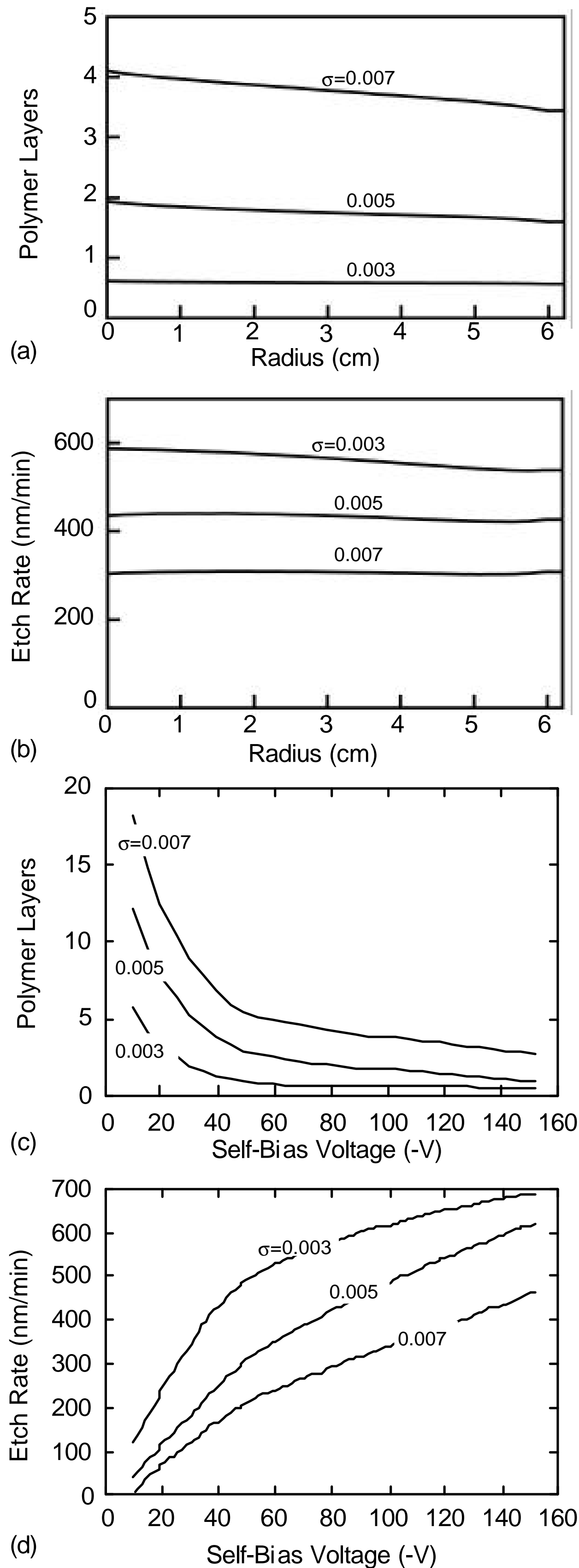

Fig. 6.8. Surface process properties as a function of neutral sticking coefficient. (a) SiO_2 etch rate, and (b) polymer thickness, as a function of radius, for different sticking coefficients. (c) SiO_2 etch rate, and (d) polymer thickness, as a function of self-bias voltage, for different sticking coefficients.

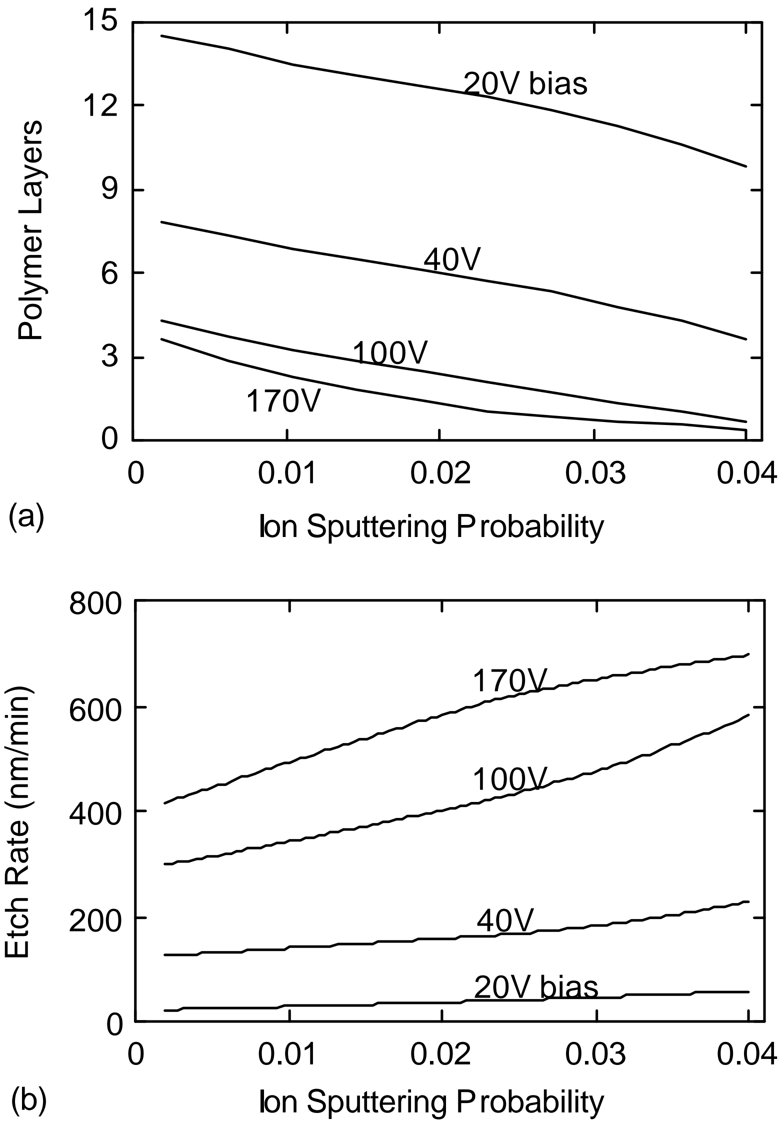

Fig. 6.9. Surface process properties as a function of ion sputtering probability p_0 for different substrate biases: (a) Polymer thickness. (b) SiO_2 etch rate.

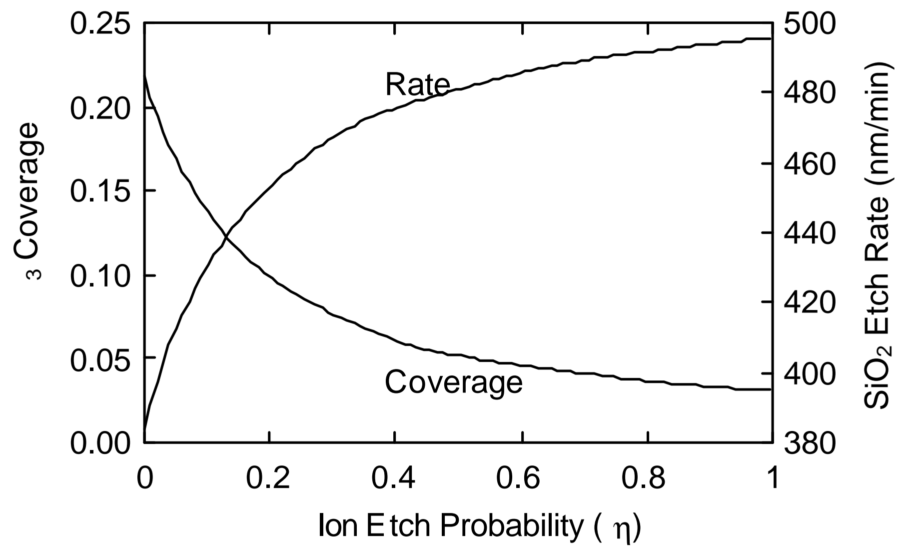

Fig. 6.10. SiF_3 surface coverage and SiO_2 etch rate as a function of ion etch probability (η).

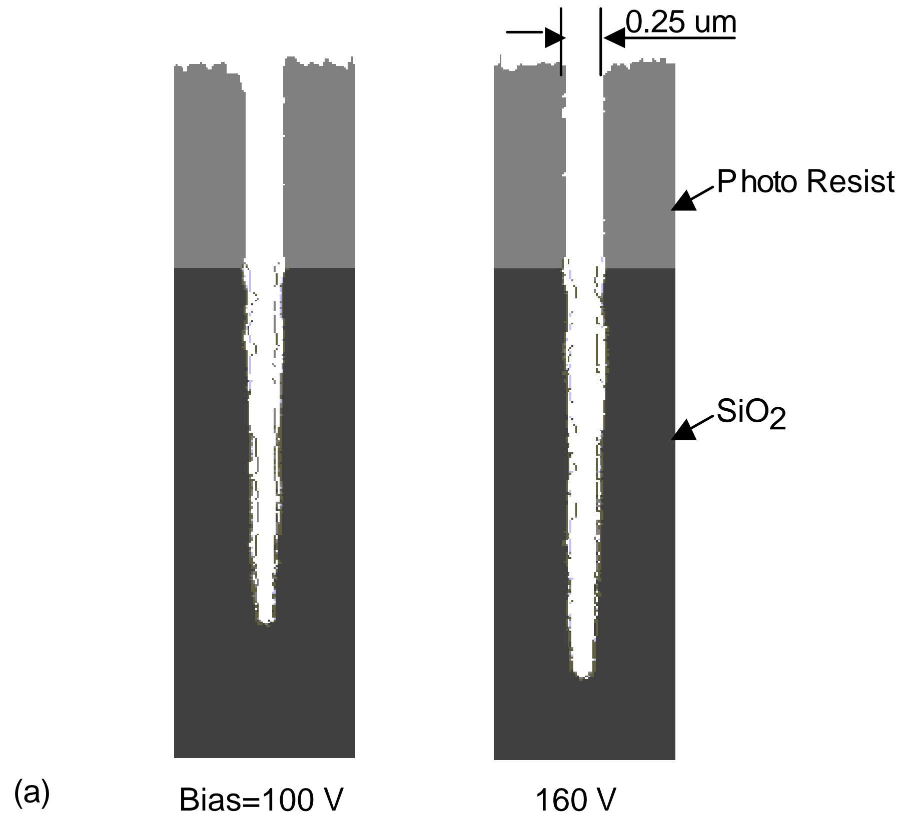

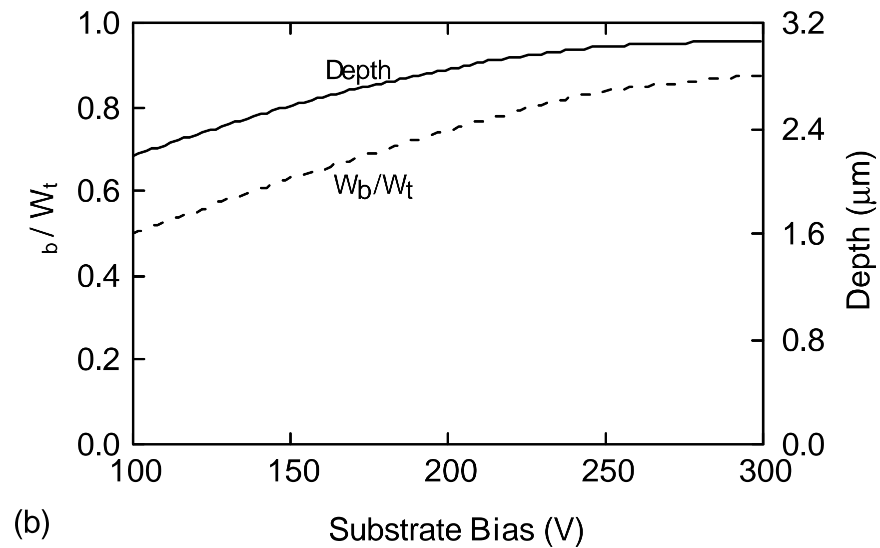

Fig. 6.11. Influences of substrate bias on feature profiles. (a) High aspect ratio profiles of SiO_2 etched by C_2F_6 plasma at 100-V and 160-V biases. The profiles taper to the bottom. (b) W_b/W_t and trench depth as a function of substrate bias. W_b refers to the trench width 0.5 **m**m above the trench bottom, and W_t is the trench width at the top. Results were obtained after equal etch times.

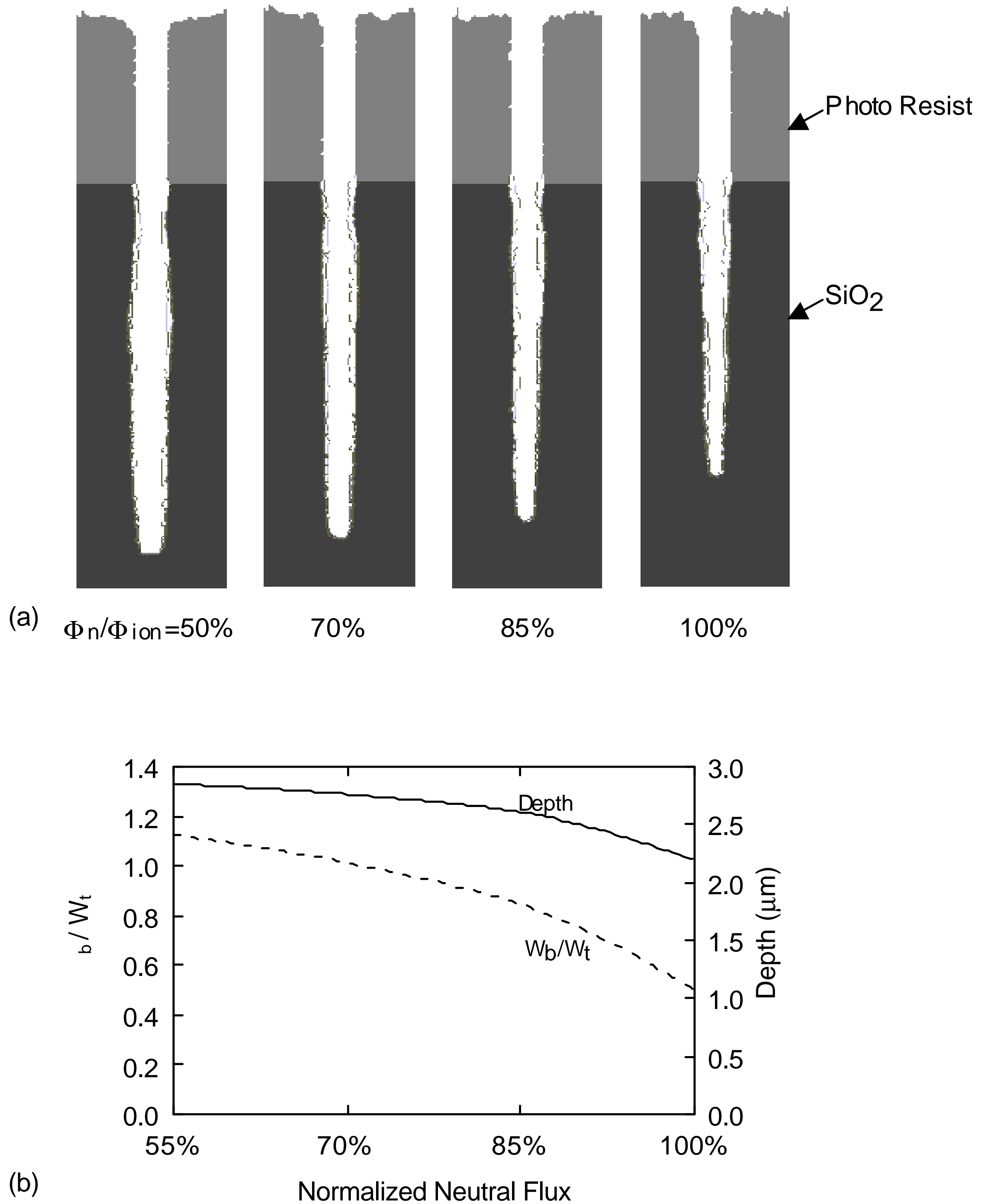

Fig. 6.12. Influences of passivating neutral-to-ion flux ratio Φ_n/Φ_{ion} on SiO_2 feature profiles. (a) Profiles for different Φ_n/Φ_{ion} ratios. The Φ_n/Φ_{ion} ratios have been normalized to the value obtained from the base case, which is labeled 100%. (b) W_b/W_t and trench depth as a function of normalized neutral flux. Results were obtained after equal etch times.

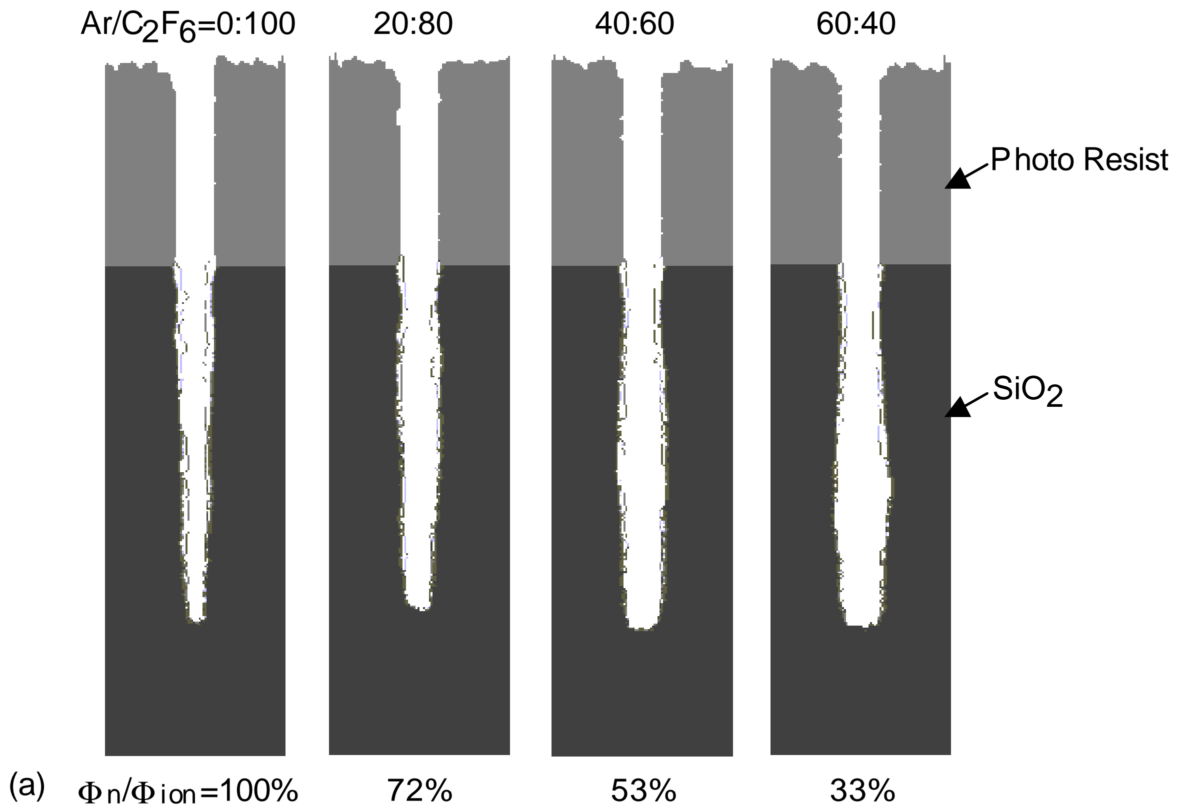

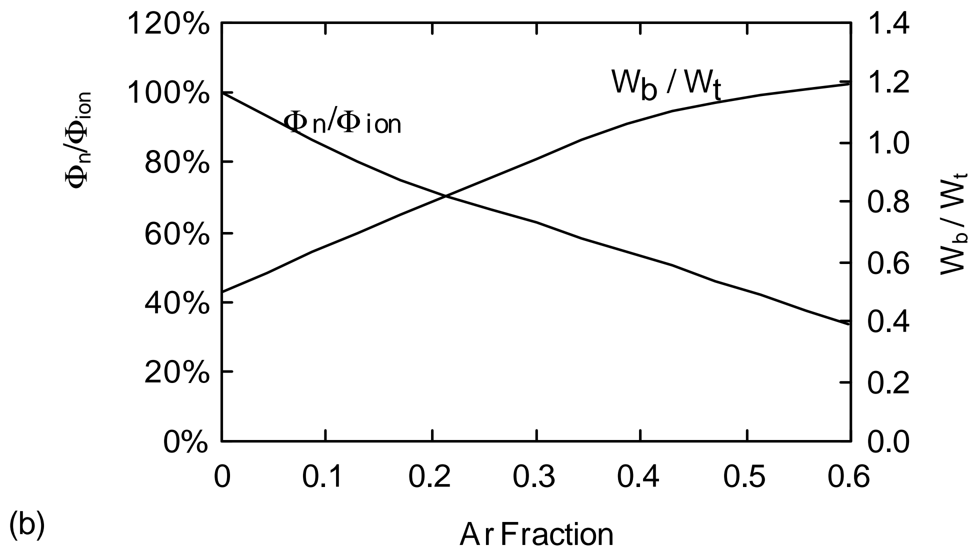

Fig. 6.13. Influences of Ar mixture in the Ar/C_2F_6 plasma source on SiO_2 feature profiles. (a) Profiles for different Ar/C_2F_6 ratios in the gas source. (b) Normalized passivating neutral-to-ion flux ratio Φ_n/Φ_{ion}, and W_b/W_t, as a function of Ar fraction in the gas source. The Φ_n/Φ_{ion} ratios have been normalized to the base case value.

6.6. References

[1] N. R. Rueger, M. F. Doemling, M. Schaepkens, J. J. Beulens, T. E. F. M. Standaert, and G. S. Oehrlein, J. Vac. Sci. Technol. A **17**, 2492 (1999).

[2] A. J. Bariya, C. W. Frank, and J. P. McVittie, J. Electrochm. Soc. **137**, 2575 (1990).

[3] B. E. E. Kastenmerier P. J. Matsuo, G. S. Oehrlein, and J. G. Langan, J. Vac. Sci. Technol. A **16**, 2047 (1998).

[4] S. Samukawa and S. Furuoya, Jpn. J. Appl. Phys., Part 2 **32**, L1289 (1993).

[5] M. Schaepkens, R. C. M. Bosch, T. E. F. M. Standaert, and G. S. Oehrlein, J. Vac. Sci. Technol. A **16**, 2099 (1998).

[6] T. E. F. M. Standaert, M. Schaepkens, N. R. Rueger, P. G. M. Sebel, G. S. Oehlein, and J. M. Cook, J. Vac. Sci. Technol. A **16**, 239 (1998).

[7] K. Miyata, M. Hori, and T. Goto, J. Vac. Sci. Technol. A **14**, 2083 (1996).

[8] M. Kitamura, H. Akiya, and T. Urisu, J. Vac. Sci. Technol. B **7**, 14 (1989).

[9] M. Schaepkens, T. E. F. M. Standaert, N. R. Rueger, P. G. M. Sebel, G. S. Oehlein, and J. M. Cook, J. Vac. Sci. Technol. A **17**, 26 (1999).

[10] N. R. Rueger, J. J. Beulens, M. Schaepkens, M. F. Doemling, J. M. Mirza, T. E. F. M. Standaert, and G. S. Oehrlein, J. Vac. Sci. Technol. A **15**, 1881 (1997).

[11] D. Zhang and M. J. Kushner, J. Appl. Phys. **87**, 1060 (2000).

[12] C. F. Abrams and D. B. Graves, J. Appl. Phys. **86**, 2263 (1999).

[13] R. J. Hoekstra and M. J. Kushner, J. Vac. Sci. Technol. B **16**, 2102 (1998).

[14] R. J. Hoekstra, M. J. Grapperhaus, and M. J. Kushner, J. Vac. Sci. Technol. A **15**, 1913 (1997).

[15] K. Teii, M. Hori, and T. Goto, J. Appl. Phys. **87**, 7185 (2000).

[16] J. P. Booth, G. Cunge, P. Chabert, and N. Sadeghi, J. Appl. Phys. **85**, 3097 (1999).

[17] M. Inayoshi, M. Ito, M. Hori, and T. Goto, J. Vac. Sci. Technol. A **16**, 233 (1998).

[18] D. C. Gray, I. Tepermeister, and H. H. Sawin, Proceedings of the 2nd International Conference on Reactive Plasmas, Yokohama, Japan, 1994.

[19] G. S. Oehrlein and J. F. Rembetski, IBM J. Res. Develop. **36**, 140 (1992).

[20] P. J. Mastuo, B. E. E. Kastenmeier, J. J. Beulens, and G. S. Oehrlein, J. Vac. Sci. technol. A **15**, 1801 (1997).

[21] M. Schaepkens, G. S. Oehlein, and J. M. Cook, J. Vac. Sci. Technol. B **18**, 848 (2000).

[22] J. W. Butterbaugh, D. C. Gray, and H. H. Sawin, J. Vac. Sci. Technol. B **9**, 1461 (1991).

[23] A. C. Westerheim, A. H. Labun, J. H. Dubash, J. C. Arnold, H. H. Sawin, and V. Yu-Wang, J. Vac. Sci. Technol. A **13**, 853 (1995).

7. CONCLUDING REMARKS

In plasma etching, plasma-surface interactions are important in that, in addition to determining the rate and quality of the process, they can influence the properties of the bulk plasma by consuming and generating plasma species. To address this coupling of bulk and surface processes, the Surface Kinetics Model (SKM) was developed for the Hybrid Plasma Equipment Model (HPEM), a two-dimensional, equipment scale simulation tool for low-temperature plasma processes. The SKM was designed to be an in-line module of the HPEM. The SKM accepts reactant fluxes from the HPEM and generates surface species coverages, process rates, and returning fluxes to the plasma by implementing a modified surface site-balance model defined by the user. To simulate fluorocarbon plasma etching processes, in which polymeric deposition on surfaces coincides with wafer etching, the SKM includes the capability of addressing the surface processes of polymer deposition, transfer of species and energy through the polymer, and polymer-thickness-dependent plasma-wafer interactions. The integration of the SKM and the HPEM provides a combined self-consistent simulation of plasma chemistry and surface chemistry.

The integrated plasma-surface model was applied to the investigation of surface effects on the CF_2 radical density in an rf CF_4 discharge. Experiments have shown that surfaces in fluorocarbon plasmas can act as both sinks and sources of CF_2. This implies that surface reactions resulting in the generation and consumption of CF_2 radicals simultaneously occur at the surface, and it is the relative magnitudes of these processes that determine whether the surface is a net source or sink of CF_2. Our simulations demonstrated that CF_2 self-sticking is a loss at the surface, while ion sputtering of the polymer deposited from C_xF_y neutrals other than CF_2, and ion

dissociation at the surface, can generate CF_2. The probabilities of ion-surface interactions increase with increasing incident ion energy, and so a surface can transition from a net CF_2 sink at low bias to a net CF_2 source at high bias. The ratio of ion flux to CF_2 density near a surface is a function of pressure, and this leads to different CF_2 density profiles at different pressures.

The mechanism of Si etching by an inductively coupled Ar/C_2F_6 plasma was investigated with the integrated plasma-surface model. A C_xF_y polymeric passivation layer is deposited on surfaces of the wafer and the reactor wall, and its steady state thickness is mainly determined by the balance of CF_x sticking, ion sputtering, and F etching of the polymer layer. Wafer etching requires chemisorption of etch precursors (F atoms) on the passivation surface, diffusion of etch precursors through the passivation layer, and successive fluorination of Si atoms. The passivation layer influences wafer etching by limiting the diffusion fluxes of etch precursors through the polymer. As a result, thicker passivation generally leads to lower Si etch rate. Increasing reactor wall temperature reduces the CF_2 sticking coefficient at the heated surface, resulting in an increasing CF_2 density in the bulk plasma. Consequently the passivation on the wafer increases and the Si etch rate drops. The ratio of Ar to C_2F_6 in the feedstock gas determines the relative densities of ions and passivating neutrals produced in the plasma. With increasing Ar fraction in the feedstock gas, the ratio of ion to passivating neutral fluxes increases, and so the polymer thickness decreases. Due to the depletion of F atoms at large Ar fractions, there is an optimal Ar fraction that produces the highest etch rate. A sensitivity analysis of the reaction mechanism demonstrates that both the magnitude and the radial dependence of the etch rate depend on the rate of ion-activated desorption of etch products.

A surface reaction mechanism for fluorocarbon plasma etching of SiO_2 was developed. The mechanism includes polymer-SiO_2 wafer interactions in the kinetics of the polymerization

process. The mechanism also describes the SiO_2 etching process which is polymer thickness dependent as a consequence of neutral passivation, reactive ion etching, and fluorination. The reaction mechanism was first applied to the integrated plasma-surface model to investigate SiO_2 etching by an inductively coupled discharge sustained in C_2F_6. Due to oxygen etching of the polymer during SiO_2 etching, the passivation thickness is smaller than its counterpart in Si etching. This provides etch selectivity of SiO_2 over Si. Increasing substrate bias increases the ion bombarding energy, so the ion sputtering yield of the polymer increases. As a result, the polymer thickness decreases and the etch rate increases with increasing substrate bias. Due to depleted passivation at high biases, the etch rate saturates. Low-energy ions activate surface sites for more rapid polymerization. That leads to enhanced polymer formation and suppressed wafer etching at low biases.

The reaction mechanism was also incorporated into the Monte Carlo Feature Profile Model (MCFPM) to investigate the feature profiles produced by this etching process. In high aspect ratio etching of SiO_2, tapered profiles were obtained, and they were attributed to the strong sidewall passivation resulting from the broad angular distributions of neutral fluxes and their low sticking coefficients. Increasing ion energy leads to less tapered profiles due to increasing polymer sputtering by ions. The tapering effect is also related to the ratio of ion to passivating neutral fluxes. Transitions of profiles from tapered to straight to bowed features with decreasing passivating neutral fluxes were observed.

APPENDIX A. $Ar/CF_4/C_2F_6$ REACTION MECHANISM[a]

Species:

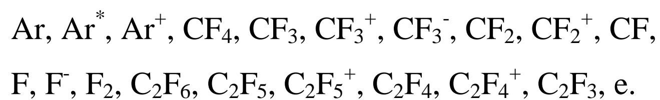

Ar, Ar^*, Ar^+, CF_4, CF_3, CF_3^+, CF_3^-, CF_2, CF_2^+, CF,

F, F^-, F_2, C_2F_6, C_2F_5, $C_2F_5^+$, C_2F_4, $C_2F_4^+$, C_2F_3, e.

Reaction	Rate Coefficient[b]	Reference
$e + Ar \rightarrow Ar^* + e$	c	[1]
$e + Ar \rightarrow Ar^+ + e + e$	c	[2]
$e + Ar^* \rightarrow Ar^+ + e + e$	c	[3]
$e + Ar^* \rightarrow Ar + e$	c	[3]
$e + CF_4 \rightarrow CF_3 + F^-$	c	[4]
$e + CF_4 \rightarrow CF_3^- + F$	c	[4]
$e + CF_4 \rightarrow CF_3 + F + e$	c	[4]
$e + CF_4 \rightarrow CF_3^+ + F + e + e$	c	[4]
$e + CF_4 \rightarrow CF_2 + F + F + e$	c	[4]
$e + CF_3 \rightarrow CF_2 + F + e$	c	[4][d]
$e + CF_3 \rightarrow CF_2 + F^-$	c	[4][d]
$e + CF_3 \rightarrow CF_3^+ + e + e$	c	[15]
$e + CF_2 \rightarrow CF_2^+ + e + e$	c	[16]
$e + CF_2 \rightarrow CF + F + e$	c	[5][d]
$e + CF_2 \rightarrow CF + F^-$	c	[5][d]
$e + C_2F_6 \rightarrow CF_3^+ + CF_3 + e + e$	c	[5]
$e + C_2F_6 \rightarrow CF_3 + CF_3^-$	c	[5]
$e + C_2F_6 \rightarrow C_2F_5 + F^-$	c	[5]
$e + C_2F_6 \rightarrow CF_3 + CF_3 + e$	c	[5]
$e + C_2F_4 \rightarrow CF_2 + CF_2 + e$	c	[5][e]
$e + C_2F_4 \rightarrow C_2F_4^+ + e + e$	c	[5][e]
$e + C_2F_4 \rightarrow F^- + C_2F_3$	c	[5]

$e + F_2 \rightarrow F^- + F$	c	[6][f]
$e + F_2 \rightarrow F + F + e$	c	[6][f]
$e + CF_3^+ \rightarrow CF_2 + F$	2.0×10^{-8}	[6][f]
$e + C_2F_5^+ \rightarrow CF_3 + CF_2$	2.0×10^{-8}	[6][f]
$e + C_2F_4^+ \rightarrow CF_2 + CF_2$	2.0×10^{-8}	[6][f]
$Ar^+ + Ar \rightarrow Ar + Ar^+$	1.0×10^{-9}	[7]
$Ar^+ + CF_4 \rightarrow CF_3^+ + F + Ar$	7.0×10^{-10}	[7]
$Ar^+ + CF_3 \rightarrow CF_3^+ + Ar$	7.0×10^{-10}	[7]
$Ar^+ + C_2F_6 \rightarrow CF_3^+ + CF_3 + Ar$	9.58×10^{-10}	[7]
$Ar^+ + C_2F_5 \rightarrow C_2F_5^+ + Ar$	1.0×10^{-10}	[8][f]
$Ar^+ + C_2F_4 \rightarrow C_2F_4^+ + Ar$	1.0×10^{-10}	[8][f]
$Ar^* + Ar^* \rightarrow Ar^+ + Ar + e$	5.0×10^{-10}	[9]
$Ar^* + CF_4 \rightarrow CF_2 + F_2 + Ar$	4.0×10^{-11}	[10]
$Ar^* + CF_3 \rightarrow CF_2 + F + Ar$	4.0×10^{-11}	[10]
$Ar^* + CF_2 \rightarrow CF + F + Ar$	4.0×10^{-11}	[10]
$Ar^* + C_2F_5 \rightarrow CF_2 + CF_3 + Ar$	4.0×10^{-11}	[10]
$Ar^* + C_2F_3 \rightarrow CF_2 + CF + Ar$	4.0×10^{-11}	[10]
$Ar^* + C_2F_6 \rightarrow CF_3 + CF_3 + Ar$	4.0×10^{-11}	[10]
$Ar^* + C_2F_4 \rightarrow CF_2 + CF_2 + Ar$	4.0×10^{-11}	[10]
$CF_3^+ + CF_3 \rightarrow CF_3^+ + CF_3$	1.0×10^{-9}	[7]
$CF_3^+ + C_2F_6 \rightarrow C_2F_5^+ + CF_4$	3.50×10^{-11}	[7]
$C_2F_5^+ + C_2F_5 \rightarrow C_2F_5^+ + C_2F_5$	1.0×10^{-9}	[7]
$C_2F_4^+ + C_2F_4 \rightarrow C_2F_4^+ + C_2F_4$	1.0×10^{-9}	[7]
$F^- + Ar^+ \rightarrow F + Ar$	1.0×10^{-7}	[11]
$F^- + CF_3^+ \rightarrow F + CF_3$	1.0×10^{-7}	[11]
$F^- + C_2F_4^+ \rightarrow F + C_2F_4$	1.0×10^{-7}	[11]
$F^- + C_2F_5^+ \rightarrow F + C_2F_5$	1.0×10^{-7}	[11]
$F^- + CF_2^+ \rightarrow F + CF_2$	1.0×10^{-7}	[11]
$CF_3^- + Ar^+ \rightarrow CF_3 + Ar$	1.0×10^{-7}	[11]

$CF_3^- + CF_3^+ \rightarrow CF_3 + CF_3$	1.0×10^{-7}	[11]
$CF_3^- + C_2F_4^+ \rightarrow CF_3 + C_2F_4$	1.0×10^{-7}	[11]
$CF_3^- + C_2F_5^+ \rightarrow CF_3 + C_2F_5$	1.0×10^{-7}	[11]
$CF_3^- + CF_2^+ \rightarrow CF_3 + CF_2$	1.0×10^{-7}	[11]
$CF_3^- + F \rightarrow CF_3 + F^-$	5.0×10^{-8}	[11]
$F + F + M \rightarrow F_2 + M$	$2.4 \times 10^{-33}(T/298)^{0.033}$ cm^6 s^{-1}	[12]
$F + C_2F_4 \rightarrow CF_3 + CF_2$	4.0×10^{-11}	[13]
$F + C_2F_5 \rightarrow CF_3 + CF_3$	1.0×10^{-11}	[13]
$F + C_2F_3 \rightarrow C_2F_4$	1.0×10^{-12}	[14]
$F + CF_3 \rightarrow CF_4$	$1.99 \times 10^{-10}(T/300)^{-7.71}\exp(-1183.4/T)$	[14]
$F + CF_2 \rightarrow CF_3$	8.40×10^{-15}	[13]
$F + CF \rightarrow CF_2$	3.90×10^{-14}	[13]
$F_2 + CF_2 \rightarrow CF_3 + F$	4.56×10^{-13}	[14]
$F_2 + CF_3 \rightarrow CF_4 + F$	1.88×10^{-14}	[14]
$CF_3 + CF_3 \rightarrow C_2F_6$	7.67×10^{-12}	[14]
$CF_2 + CF_2 \rightarrow C_2F_4$	5.0×10^{-14}	[14]
$CF_2 + CF_3 \rightarrow C_2F_5$	8.26×10^{-13}	[14]

Notes:
[a]Only reactions directly affecting species densities are shown here. Additional electron impact collisions (e.g., momentum transfer, vibrational excitation) are included in the EETM.
[b]Rate coefficients have units cm^3 s^{-1} unless noted otherwise.
[c]Computed using the electron energy distribution and electron impact cross section from cited reference.
[d]Estimated by analogy to CF_4.
[e]Estimated by analogy to C_2F_6.
[f]Estimated. See cited reference for similar reaction.

A.1. References

[1] K. Tachibana, Phys. Rev. A **34**, 1007 (1986).

[2] D. Rapp and P. Englander-Golden, J. Chem. Phys. **43**, 1464 (1965).

[3] R. H. McFarland and J. D. Kinney, Phys. Rev. **137**, A1058 (1965).

[4] R. A. Bonham, Jpn. J. Appl. Phys., Part 1 **33**, 4157 (1994)

[5] M. Hayashi, in *Gaseous Dielectrics V*, edited by L. G. Christophorou and D. W. Bouldin (Pergamon, New York, 1987).

[6] M. Hayashi and T. Nimura, J. Appl. Phys. **54**, 4879 (1983).

[7] E. Fisher, M. E. Weber, and P. B. Armentrout, J. Chem. Phys. **76**, 4932 (1982).

[8] G. K. Jarvis, C. A. Mayhew, R. P. Tuckett, J. Phys. Chem. **100**, 17166 (1996).

[9] P. K. Leichner and R. J. Ericson, Phys. Rev. A **9**, 251 (1974).

[10] J. E. Velazco, J. H. Koltz, and D. W. Sester, J. Chem. Phys. **65**, 3468 (1976).

[11] R. E Olson, J. R. Peterson, and J. Moseley, J. Chem. Phys. **53**, 3391 (1971).

[12] E. L. Duman, N. P. Tishchenko, and I. P. Shmatov, Dokl. Phys. Chem. **295**, 5 (1987).

[13] C. Plumb, K. R. Ryan, Plasma Chem. Plasma Proc., **6**, 205 (1986).

[14] D. R. F. Burgess, Jr., M. R. Zachariah, W. Tsang, and P. R. Westmoreland, Prog. Energy Combust. Sci., **21**, 453,1996.

[15] V. Tarnovsky, P. Kurunczi, D. Rogozhnikov, and K. Becker, Int. J. Mass. Spectrom. Ion Processes **128**, 181 (1993).

[16] H. Deutsch, T. D. Bark, V. Tarnovsky, K. Becker, C. Cornelissen, L. Cespiva, and V. Bonacic-Koutecky, Int. J. Mass. Spectrom. Ion Processes **137**, 77 (1994).

VITA

Da Zhang was born in Guangde, Anhui, P. R. China, in 1972. He received his B.S. and M.S. degrees in materials science and engineering from Zhejiang University in 1993 and 1996, respectively. In 1996 he entered the graduate school of the University of Illinois at Urbana-Champaign. Under the direction of Professor Mark J. Kushner, he has studied low-temperature, low-pressure plasma processes and their equipment and feature scale simulation. He interned with Lam Research Corporation from June 1999 to August 1999. He is a member of the American Vacuum Society.